

An Optical Readout for the LISA Gravitational Reference Sensor

DISSERTATION

zur Erlangung des akademischen Grades

Dr. rer. nat
im Fach Physik

eingereicht an der
Mathematisch-Naturwissenschaftlichen Fakultät I
Humboldt-Universität zu Berlin

von

Dipl. Phys. Thilo Schuldt
geboren am 19.04.1975 in Singen

Präsident der Humboldt-Universität zu Berlin:
Prof. Dr. Dr. h.c. Christoph Marksches

Dekan der Mathematisch-Naturwissenschaftlichen Fakultät I:
Prof. Dr. Lutz-Helmut Schön

Gutachter:

1. Prof. Achim Peters, Ph.D.
2. Prof. Dr. Claus Braxmaier
3. PD Dr. Hans-Jürgen Wünsche

eingereicht am: 15.10.2009

Tag der mündlichen Prüfung: 14.07.2010

Abstract

The space-based gravitational wave detector LISA (Laser Interferometer Space Antenna) consists of three identical satellites. Each satellite accommodates two free-flying proof masses whose distance and tilt with respect to its corresponding optical bench must be measured with at least $1 \text{ pm}/\sqrt{\text{Hz}}$ sensitivity in translation and at least $10 \text{ nrad}/\sqrt{\text{Hz}}$ sensitivity in tilt measurement.

In this thesis, a compact optical readout system – consisting of an optomechatronic setup together with associated electronics, data acquisition and software – is presented, which serves as a prototype for the LISA proof mass attitude metrology. We developed a polarizing heterodyne interferometer with spatially separated frequencies. For optimum common mode rejection, it is based on a highly symmetric design, where measurement and reference beam have the same frequency and polarization, and similar optical pathlengths. The method of differential wavefront sensing (DWS) is utilized for the tilt measurement. An intrinsically highly stable Nd:YAG laser at a wavelength of 1064 nm is used as light source; the heterodyne frequencies are generated by use of two acousto-optic modulators (AOMs).

In a first prototype setup noise levels below $100 \text{ pm}/\sqrt{\text{Hz}}$ in translation and below $100 \text{ nrad}/\sqrt{\text{Hz}}$ in tilt measurement (both for frequencies above 10^{-1} Hz) are achieved. A second prototype was developed with additional intensity stabilization and phaselock of the two heterodyne frequencies. The analog phase measurement is replaced by a digital one, based on a Field Programmable Gate Array (FPGA). With this setup, noise levels below $5 \text{ pm}/\sqrt{\text{Hz}}$ in translation measurement and below $10 \text{ nrad}/\sqrt{\text{Hz}}$ in tilt measurement, both for frequencies above 10^{-2} Hz , are demonstrated. A noise analysis was carried out and the nonlinearities of the interferometer were measured.

The interferometer was developed for the LISA mission, but it also finds its application in characterizing the dimensional stability of ultra-stable materials such as carbon-fiber reinforced plastic (CFRP) and in optical profilometry. The adaptation of the interferometer and first results in both applications are presented in this work. DBR (Distributed Bragg-Reflector) laser diodes represent a promising alternative laser source. In a first test, laser diodes of this type with a wavelength near 1064 nm are characterized with respect to their spectral properties and are used as light source in the profilometer setup.

Zusammenfassung

Der weltraumgestützte Gravitationswellendetektor LISA (Laser Interferometer Space Antenna) besteht aus drei identischen Satelliten, an Bord derer sich jeweils zwei frei schwebende Testmassen befinden. Die Lage der einzelnen Testmassen in Bezug auf die zugehörige optische Bank muss mit einer Genauigkeit besser $1 \text{ pm}/\sqrt{\text{Hz}}$ in der Abstands- und besser $10 \text{ nrad}/\sqrt{\text{Hz}}$ in der Winkelmessung erfolgen.

In der vorliegenden Arbeit wird ein kompaktes optisches Auslesesystem – bestehend aus einem optomechanischen Aufbau mit zugehöriger Elektronik, Datenerfassung und Software – präsentiert, welches als Prototyp für diese Abstands- und Winkelmetrologie dient. Das dafür entwickelte polarisierende Heterodyn-Interferometer mit räumlich getrennten Frequenzen basiert auf einem hoch-symmetrischen Design, bei dem zur optimalen Gleichtakt-Unterdrückung Mess- und Referenzarm die gleiche Polarisation und Frequenz sowie annähernd gleiche optische Pfade haben. Für die Winkelmessung wird die Methode der differentiellen Wellenfrontmessung (differential wavefront sensing, DWS) eingesetzt. Als Lichtquelle wird ein Nd:YAG Festkörper-Laser bei einer Wellenlänge von 1064 nm verwendet; die Heterodyn-Frequenzen werden mittels zweier akusto-optischer Modulatoren (AOMs) generiert.

In einem ersten Prototyp-Aufbau wird ein Rauschniveau von weniger als $100 \text{ pm}/\sqrt{\text{Hz}}$ in der Translations- und von weniger als $100 \text{ nrad}/\sqrt{\text{Hz}}$ in der Winkelmessung (beides für Frequenzen oberhalb 10^{-1} Hz) demonstriert. In einem zweiten Prototyp-Aufbau werden zusätzlich eine Intensitätsstabilisierung und ein Phasenlock der beiden Frequenzen implementiert. Die analoge Phasenmessung ist durch eine digitale, auf einem Field Programmable Gate Array (FPGA) basierende, ersetzt. Mit diesem Aufbau wird ein Rauschen kleiner $5 \text{ pm}/\sqrt{\text{Hz}}$ in der Translationsmessung und kleiner $10 \text{ nrad}/\sqrt{\text{Hz}}$ in der Winkelmessung, beides für Frequenzen größer 10^{-2} Hz , erreicht. Eine Rausch-Analyse wurde durchgeführt und die Nichtlinearitäten des Interferometers bestimmt.

Das Interferometer wurde im Hinblick auf die LISA Mission entwickelt, findet seine Anwendung aber auch bei der Charakterisierung der dimensional Stabilität von ultra-stabilen Materialien wie Kohlefaser-Verbundwerkstoffen (carbon-fiber reinforced plastic, CFRP) sowie in der optischen Profilometrie. Die Adaptierung des Interferometers dazu sowie erste Resultate zu beiden Anwendungen werden in dieser Arbeit präsentiert. Eine alternative Laserquelle stellen DBR (Distributed Bragg-Reflector) Laserdioden dar. In einem ersten Test werden Laserdioden dieses Typs mit einer Wellenlänge nahe 1064 nm hinsichtlich ihrer spektralen Eigenschaften charakterisiert und im Profilometer als Lichtquelle eingesetzt.

Contents

Introduction	1
1. Gravitational Waves and Their Detection	5
1.1. General Relativity	5
1.2. Sources of Gravitational Waves	7
1.3. Gravitational Wave Detection	9
1.3.1. Indirect Proof	9
1.3.2. Bar Detectors	9
1.3.3. Interferometric Measurements	10
2. The LISA Mission Metrology Concept	13
2.1. Overall Mission Concept	13
2.2. The LISA Optical Bench design	18
2.3. The LISA Gravitational Reference Sensor	19
2.4. Drag-Free Attitude Control System (DFACS)	21
3. The LISA Gravitational Reference Sensor Readout	23
3.1. Capacitive Readout	23
3.2. SQUID-based Readout	25
3.3. Optical Readout (ORO)	26
3.3.1. Lever Sensor	27
3.3.2. Interferometric Measurement	27
3.3.3. ORO at the University of Napoli (Italy)	29
3.3.4. ORO at the University of Birmingham (England)	29
3.3.5. ORO at Stanford University (USA)	29
3.3.6. The LTP ORO aboard LISA Pathfinder	32
4. Interferometric Concepts	35
4.1. Interferometer Basics	35
4.1.1. In-Quadrature Measurement	37
4.1.2. Periodic Nonlinearities	38
4.2. Homodyne Michelson Interferometer	39
4.2.1. In-Quadrature Measurement	40

4.3.	Heterodyne Michelson Interferometer	40
4.3.1.	In-Quadrature Measurement	42
4.3.2.	Evaluation of Periodic Nonlinearities	43
4.3.3.	Generation of Heterodyne Frequencies	45
4.4.	Mach-Zehnder Interferometer	45
4.5.	Heterodyne Interferometer with Spatially Separated Frequencies	46
4.6.	A Heterodyne Interferometer Design as LISA Optical Readout	47
4.7.	Differential Wavefront Sensing	50
5.	Interferometer Setup	53
5.1.	Heterodyne Frequency Generation	53
5.2.	Interferometer Setup	54
5.3.	Phase Measurement and Data Processing	55
5.4.	LabView Data Processing	57
5.5.	Experimental Results	58
5.5.1.	First Check of the Phase Measurement	58
5.5.2.	PZT in the Measurement Arm of the Interferometer	59
5.5.3.	PZT in Reference and Measurement Arm	62
5.5.4.	Without PZT in the Setup	65
5.6.	Noise Analysis and Identified Limitations	66
6.	Advanced Setup	71
6.1.	Frequency Generation	71
6.2.	Interferometer Setup	72
6.3.	Intensity Stabilization	75
6.4.	Heterodyne Frequency Phaselock	75
6.5.	Frequency Stabilization of the Nd:YAG Laser	76
6.6.	Digital Phase Measurement	78
6.7.	Vacuum System	79
6.8.	Measurements	79
6.8.1.	Test of the Digital Phasemeter	79
6.8.2.	Translation Measurement	79
6.8.3.	Tilt Measurement	84
6.9.	Measurement of the Nonlinearities	84
6.9.1.	Experimental Setup	86
6.9.2.	Results	86
6.10.	Noise Analysis	90
7.	Applications	95
7.1.	Dilatometry	95
7.1.1.	Measurement Concept	96

7.1.2. Experimental Setup	96
7.1.3. Experimental Results	97
7.1.4. Limitations and Next Steps	100
7.2. Profilometry	101
7.2.1. Experimental Setup	102
7.2.2. First Measurements	102
8. Conclusion and Next Steps	107
A. Compact Frequency Stabilized Laser System	113
B. Electronics	115
B.1. Quadrant Photodiode Electronics	115
B.2. PID-Servo Loop	115
B.3. 6th Order Lowpass	118
C. LabVIEW Programs	121
C.1. First Interferometer Setup	121
C.2. Second Interferometer Setup	122
D. Calculation of the Power Spectrum Density	127
E. Frequency Stabilized Nd:YAG Laser	129
F. Alternative Laser Source	131
F.1. DBR Laser Diodes	131
F.2. Laser Module	133
F.3. First Characterization	133
Bibliography	135
Acknowledgments	147
List of Publications	149

Introduction

The history of astronomy is the history of receding horizons.

Edwin Hubble

Since the beginning of mankind people looked into the sky, and tried to understand the presence and the motions of the luminaries. Outer space implicated key human questions such as the existence of god, the creation of the universe and the Earth and the possibility of extraterrestrial life. Not only was all instrumentation available at that time used in order to get a deeper understanding of astronomy and astrophysics, but humankind's ambition to explore the sky and the universe was one of the main technology drivers throughout history.

First observations were made by naked eye, but the invention of the telescope at the beginning of the 17th century, and the knowledge of its potential by Galileo Galilei, enabled much more detailed observations and motivated modern astronomy. The optical setup, the optical component fabrication and the resulting telescope resolution were improved in the following enabling an in-depth analysis of celestial bodies in the visible wavelength region.

With the discovery of infrared radiation by the astronomer William Herschel in 1800, it became clear that the visible wavelength region is only a detail of a much more general spectrum which could be mathematically described by Maxwell's electromagnetic theory of light in 1864. The electromagnetic wave spectrum spans the whole wavelength region, including radio waves ($\lambda > 1$ m), microwaves ($\lambda = 1$ m ... 1 mm), infrared ($\lambda = 1$ mm ... 700 nm), visible ($\lambda = 750$... 380 nm), ultra-violet ($\lambda = 400$... 1 nm), X-rays ($\lambda = 10$... 0.01 nm) and gamma radiation ($\lambda < 10$ pm). Detecting light from outer space means building specific detectors for each wavelength region and to combine the information obtained in order to get a more extensive knowledge of astrophysical processes.

The Earth's atmosphere is a strong limitation for outer space observation. First because the telescope's angular resolution is limited by turbulence in the atmosphere, and second because the atmosphere has strong absorptions in the electromagnetic spectrum. The atmosphere blocks high energy radiation such as X-rays, gamma and ultra-violet radiation and shows strong absorption lines in the infrared. When it became possible to launch artificial satellites into an orbit outside the Earth's atmosphere, space-based telescopes were developed, launched and

operated. Examples are the radio astronomy satellite HALCA, the Hubble space telescope in the visible, near-ultra-violet and near-infrared spectral ranges, the Herschel telescope in the far infrared spectral range, the Extreme Ultra-violet Explorer (EUVE), the X-ray observatory XMM-Newton, the Compton Gamma Ray Observatory (CGRO) and COBE, a satellite investigating the cosmic microwave background radiation.

Up until now, telescopes detecting all parts of the electromagnetic spectrum – covering a range of 20 orders of magnitude in frequency – are operating. Each time the bandwidth was expanded to a different wavelength region in the electromagnetic spectrum, a different aspect of the universe was observed. But still, essentially all our knowledge about outer space is based on observations of electromagnetic waves emitted by individual electrons, atoms and molecules¹. When Einstein published his Theory of General Relativity in 1915, a new kind of waves was predicted: gravitational waves caused by asymmetrically accelerated masses. In contrast to electromagnetic waves, which are easily scattered, absorbed and dispersed, gravitational waves travel nearly undisturbed through space and time – opening a completely new access to space observation.

Gravitational waves distort spacetime, and therefore change the distances between free macroscopic bodies. As their amplitude is tiny, only processes involving huge masses can produce significant and measurable signals. Sources of gravitational waves cover a frequency range from 10^{-16} Hz to 10^4 Hz, and include galactic binary systems (such as neutron star binaries, black hole binaries, white dwarf binaries), mergers of massive black holes and supernovae collapses. While the high-frequency range 10 to 10^3 Hz can be covered by ground-based detectors, the low frequency range below 0.1 Hz is only accessible by space-based detectors.

Several ground-based gravitational wave detectors already exist and are on the way to achieve their designated sensitivities. Space-based detectors are proposed and studies on their design are being carried out. One specific space mission is LISA (Laser Interferometer Space Antenna) – an ESA/NASA collaborative space mission dedicated to the detection of gravitational waves in the low-frequency range $30 \mu\text{Hz}$ to 1 Hz. Three similar satellites form a giant Michelson interferometer in space with an armlength of 5 million kilometers as shown in Fig. 1. The LISA mission, planned to be launched around 2019, is currently in the so-called mission formulation phase, where the science requirements are fixed and the mission requirements are assigned. The corresponding study is carried out at Astrium GmbH – Satellites, Friedrichshafen, on behalf of ESA. This study also reveals critical subsystems and drives their technology demonstration first in on-ground laboratory experiments.

One of the subsystems is the readout of the LISA gravitational reference sensor

¹Also the analysis of meteorites and the detection of neutrinos are used for the study of astrophysical processes.

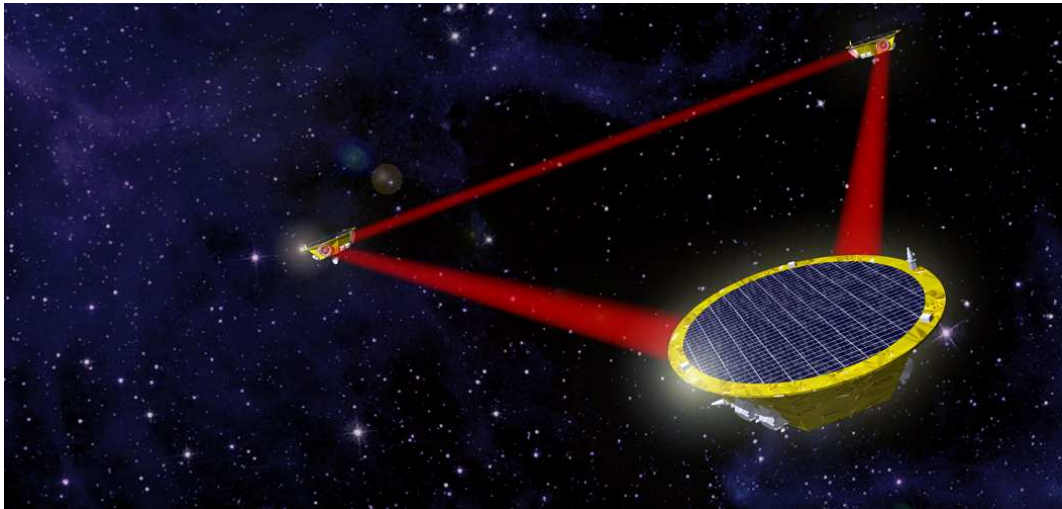


Figure 1.: Artist's view of the LISA space mission. Three satellites form a Michelson interferometer with an armlength of ~ 5 million kilometers (source: Astrium GmbH).

(GRS) where the position and tilt of a free flying proof mass with respect to the optical bench must be measured with pm-sensitivity in translation and nanoradian-sensitivity in tilt measurement. The needed sensitivity requires for an optical readout (ORO) where different implementations are conceivable. Several groups around the world are investigating different approaches, where interferometric measurements, which can be realized in a variety of designs, offer the highest potential. They can be subdivided in polarizing or non-polarizing setups, homodyne or heterodyne detection, Michelson or Mach-Zehnder type interferometers. All methods have their specific advantages and disadvantages. While an optical lever sensor is developed at the University of Napoli, interferometric methods are investigated at Stanford University (grating interferometer), University of Birmingham (homodyne polarizing interferometer; Michelson type) and Albert-Einstein-Institute Hannover (in collaboration with University of Glasgow and Astrium GmbH – Satellites, Friedrichshafen; heterodyne non-polarizing interferometer, Mach-Zehnder type).

The currently achieved noise levels of the different ORO implementations are shown in Fig. 2, together with the LISA science requirements. The readout systems developed by the Universities of Napoli, Birmingham and Standford can currently not demonstrate the noise levels required for LISA. The LTP interferometer – specifically built with respect to the LISA Pathfinder mission requirements – uses a glass ceramics baseplate where the optical components are fixed to using hydroxide-catalysis bonding technology. An alternative ORO implementation for LISA – based on single-path polarizing heterodyne interferometry – will be dis-

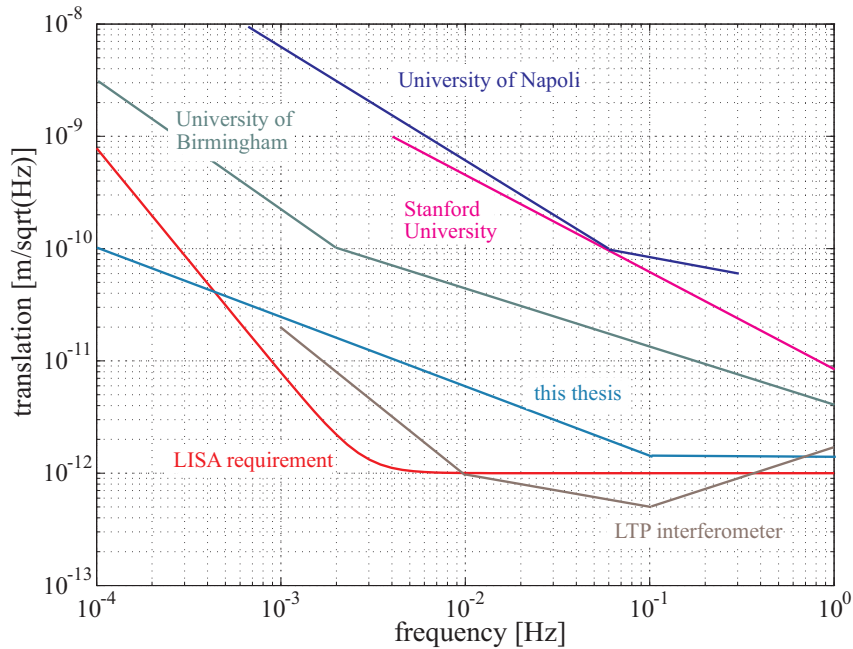


Figure 2.: Achieved noise levels of different optical readout implementations. Also included is the LISA science requirement.

cussed in the following and is the subject of this thesis. It is built as a laboratory setup, using a cast aluminum baseplate and optical mounts made of aluminum and stainless steel. The achieved noise levels are also included in Fig. 2.

Outline of the thesis: A short introduction to the physics of gravitational waves is given in Chapter 1 which also includes an overview of different methods for gravitational wave detection. A detailed outline of the LISA space mission is given in Chapter 2, focussing on the optical setup. Different possibilities for the optical readout of the LISA gravitational reference sensor are outlined in Chapter 3 where Chapter 4 will focus on interferometric concepts. Our interferometer design is presented in Chapter 5 and Chapter 6 where the experimental setups and measurements are shown. First applications of the interferometer in high-accuracy dilatometry and optical profilometry are presented in Chapter 7. Chapter 8 comprises a conclusion and the next steps with respect to an enhanced interferometer setup.

1. Gravitational Waves and Their Detection

Gravitational waves are deduced from the field equations in Einstein's theory of general relativity which was first published in 1915. Although most parts of the theory of general relativity are experimentally verified to a very high degree of precision, up until now, there has been no direct verification of the existence of gravitational waves.

This chapter shortly describes how gravitational waves result from general relativity, what kind of astrophysical events cause such waves and what different techniques of gravitational wave detection exist.

1.1. General Relativity

The theory of general relativity presents the relativistic generalization of Newton's gravitational theory where gravity can be expressed as a spacetime curvature (cf. e.g. [1, 2]). The Einstein field equations describe the relation between the Einstein tensor $G_{\mu\nu}$ representing the curvature of spacetime and the stress-energy tensor $T_{\mu\nu}$ which represents the mass and energy content of spacetime:

$$G_{\mu\nu} = \frac{8\pi G}{c^4} T_{\mu\nu}. \quad (1.1)$$

Here, G is the gravitational constant and c the speed of light. The tensors $G_{\mu\nu}$ and $T_{\mu\nu}$ are symmetric; equation (1.1) therefore corresponds to a system of 10 nonlinear partial differential equations. The field equations have the same form as an elasticity equation where spacetime represents the elastic medium. It is extremely stiff as its elasticity module is given by $G/c^4 \approx 10^{-43} \text{ N}^{-1}$.

The (infinitesimal) distance ds between two points in spacetime with coordinates x^μ and $x^\mu + dx^\mu$ is given by

$$ds^2 = g_{\mu\nu} dx^\mu dx^\nu, \quad (1.2)$$

where $g_{\mu\nu}$ is the symmetric metric tensor which contains the information on spacetime curvature. In case of the flat spacetime of special relativity, the metric tensor

is given by the Minkowskian metric $\eta_{\mu\nu} = \text{diag}(1, -1, -1, -1)$, where the distance is given by

$$ds^2 = \eta_{\mu\nu} dx^\mu dx^\nu = -c^2 dt^2 + dx^2 + dy^2 + dz^2. \quad (1.3)$$

The Minkowskian metric is a solution of the Einstein field equations with $T_{\mu\nu} = 0$. In a weak field approximation, the metric tensor can be written as

$$g_{\mu\nu} = \eta_{\mu\nu} + h_{\mu\nu}, \quad (1.4)$$

where $h_{\mu\nu} \ll 1$ is a small perturbation of the Minkowskian metric and a measure of spacetime curvature. The linearized field equation is then given by

$$\left(-\frac{1}{c^2} \frac{\delta^2}{\delta t^2} + \Delta \right) h_{\mu\nu} = -\frac{16\pi G}{c^4} T_{\mu\nu}. \quad (1.5)$$

For a source-free space with $T_{\mu\nu} = 0$, this results in a homogeneous wave equation

$$\left(-\frac{1}{c^2} \frac{\delta^2}{\delta t^2} + \Delta \right) h_{\mu\nu} = 0, \quad (1.6)$$

with plane waves as a solution. These gravitational waves propagate with the speed of light $v = c$ in the direction of \vec{k} ($k = \omega/c$):

$$h_{\mu\nu}(\vec{r}, t) = h_{\mu\nu}^0 \sin(\vec{k}\vec{r} - \omega t + \phi_{\mu\nu}). \quad (1.7)$$

Two polarizations of such gravitational waves exist; they are called ‘+’ and ‘×’ and are orthogonal to one another. The gravitational wave amplitude tensor $h_{\mu\nu}$ is given by

$$h_{\mu\nu} = \begin{pmatrix} 0 & 0 & 0 & 0 \\ 0 & h_+ & h_\times & 0 \\ 0 & h_\times & -h_+ & 0 \\ 0 & 0 & 0 & 0 \end{pmatrix}. \quad (1.8)$$

This means, $h_{\mu\nu}$ can be described as a superposition of two gravitational waves with different polarization. Their corresponding amplitudes are given by h_+ and h_\times , respectively.

Analogous to electromagnetic waves which interact with charged particles, gravitational waves interact with massive particles. For two masses separated by \vec{L} , the change in their separation $\delta\vec{L}$ is given by (see e.g. [2])

$$\frac{\delta L}{L} = \frac{1}{2} h. \quad (1.9)$$

Therefore, a gravitational wave with amplitude h (either h_+ or h_\times) stretches and

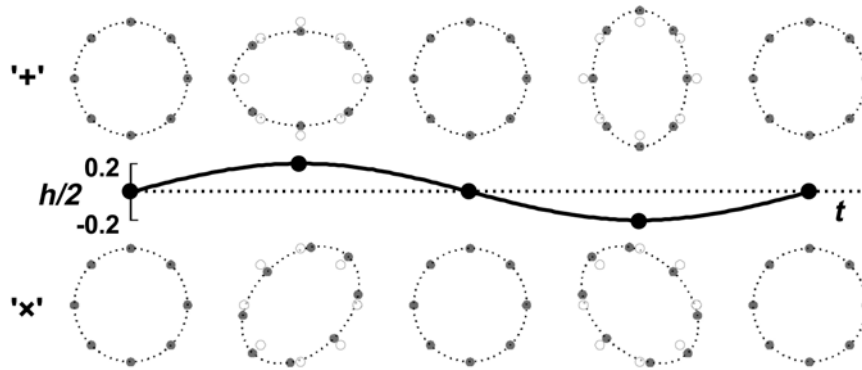


Figure 1.1.: Illustration of the two existing polarizations ‘+’ and ‘x’ of gravitational waves and their effect on a ring of free particles [3]. The polarizations are transverse to the direction of the wave.

shrinks the distance between two free bodies. This equation also states, that gravitational wave detectors should have a large baseline L since the change in distance δL caused by the gravitational wave with an amplitude h increases proportional to L .

Gravitational waves are transverse, i.e. they act in a plane perpendicular to their direction of propagation. In the transverse plane, gravitational waves are area preserving: when observing a ring of free particles, it will be stretched in one given direction and simultaneously squeezed in the direction perpendicular to that direction. In Fig. 1.1 the two polarizations of gravitational waves and their effect on a ring of free particles are shown schematically.

1.2. Sources of Gravitational Waves

Gravitational waves are caused by asymmetrically accelerated masses. As an example for a gravitational wave source, the amplitude h of a gravitational wave caused by a binary system where all mass is part of an asymmetric motion, is given by [3]:

$$h = 1.5 \times 10^{-21} \left(\frac{f}{10^{-3} \text{ Hz}} \right)^{2/3} \left(\frac{r}{1 \text{ kpc}} \right)^{-1} \left(\frac{\mathcal{M}}{M_{\odot}} \right)^{5/3} \quad (1.10)$$

where f is the gravitational wave frequency (and corresponds to twice the binary orbital frequency), r is the distance source to detector and \mathcal{M} the ‘chirp mass’ of

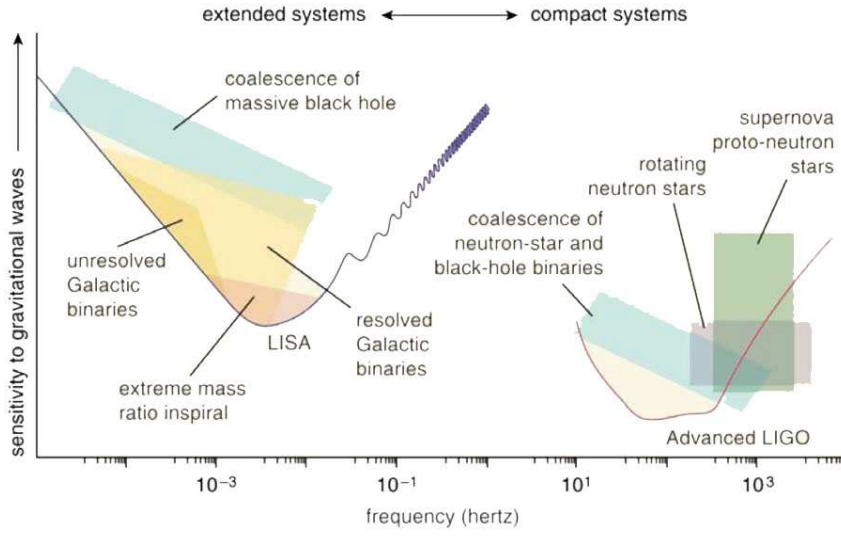


Figure 1.2.: Spectrum of gravitational waves. Shown are relevant sources for the spaceborne gravitational wave detector LISA and the Earth-bound gravitational wave detector (advanced) LIGO [8].

two stellar masses M_1 and M_2 :

$$\mathcal{M} = \frac{(M_1 M_2)^{3/5}}{(M_1 + M_2)^{1/5}}. \quad (1.11)$$

Equation (1.10) also shows the order of magnitude of the gravitational wave amplitude h . Only huge masses, which can only be found in astrophysics, can produce significant and measurable gravitational wave signals.

Sources of gravitational waves can be subdivided into three classes: bursts, periodic waves and stochastic waves – covering a frequency range from 10^{-16} Hz to 10^4 Hz. Burst sources include star collapses as supernova explosions, coalescent binary systems and the fall of stars or small black holes into a supermassive black hole ($M > 10^5 M_\odot$). Bursts only last for a very short time, i.e. a few cycles. Periodic sources with significant emission of gravitational wave radiation are double star binary systems and spinning stars as pulsars. A potential stochastic source of gravitational waves is the random primordial cosmological background¹ (cf. e.g. [4]).

An overview of different sources in the frequency range 10^{-4} Hz to 10^4 Hz is given in Fig. 1.2. An outline of gravitational wave sources and their astrophysical interest can be found e. g. in [5, 6, 7, 8].

¹The cosmic gravitational wave background (CGWB) is similar to the cosmic microwave background (CMB). While the CMB dates from about 380000 years after the big bang the predicted CGWB sets in nearly instantly after the big bang.

1.3. Gravitational Wave Detection

Detection of gravitational waves can be distinguished into indirect and direct methods where the direct methods can be further classified into resonant bar detection and interferometric measurements.

1.3.1. Indirect Proof

The indirect proof of the existence of gravitational waves was carried out by J. Taylor and R. Hulse by analyzing the rotation frequency of the PSR1913+16 double pulsar which they discovered in 1974 using the 305 m Arecibo radio telescope [9]. The fast rotation of a pulsar in combination with a very strong magnetic field leads to the emission of radio waves emitted in the direction of the magnetic poles of the pulsar. If this beam happens to be aligned in a way that it hits the Earth during the pulsar rotation, it hence yields to the characteristic pulses detected on Earth. The pulse repetition rate is extremely stable and pulsars can be taken as high-precision clocks. PSR1913+16 is a binary system consisting of two stars with similar mass. The accumulated shift of the times of periastron² is shown in Fig. 1.3. The straight line corresponds to a constant rotation period. Due to energy loss, the separation between the two stars decreases causing an increase in rotation frequency. The loss of energy can be explained by gravitational waves emitted by the binary system. The parabolic curve shows the prediction based on general relativity and presents the first indirect proof of gravitational waves [10, 11, 12]. For their work, Hulse and Taylor were awarded the Nobel Prize in physics in 1993.

1.3.2. Bar Detectors

The pioneering experimental work for the direct detection of gravitational waves was carried out by Joseph Weber in the early 1960s [13]. His idea was to use large aluminum bars with a weight of 1.5 t as resonant-mass antenna where a gravitational wave passing the detector will change the length of the aluminum bar. A gravitational wave with suitable frequency will excite a vibration of the bar – the bar then rings like a bell struck with a hammer. Weber built up a detector consisting of two aluminum cylinders located at the University of Maryland and the 1000 km distant Argonne National Laboratory near Chicago. The bars are located in a vacuum chamber, isolated against vibrations and operated at room temperature. A piezo ceramic was used for strain measurement and a coincidence measurement between both detectors with sensitivities of $h = 7 \cdot 10^{-17}$ was carried out. Resonant bar detectors are typically sensitive in a 1 Hz bandwidth around their resonant frequency which is between 700 Hz and 1000 Hz.

²Periastron is the point in the binary system where both stars have minimum distance.

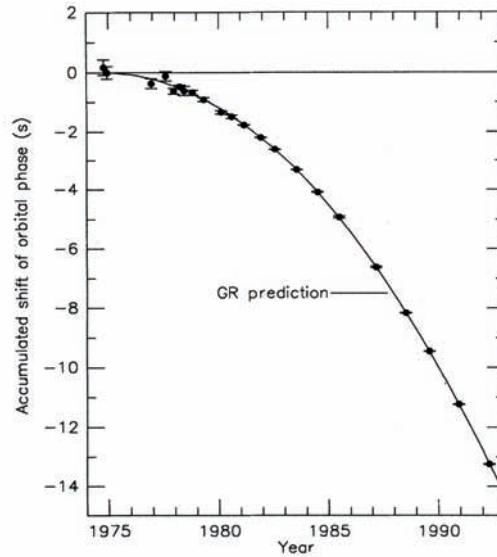


Figure 1.3.: Accumulated shift of the orbital phase of the binary system PSR1913+16. The straight line corresponds to a constant period, the parabolic curve is the prediction of general relativity. The losses are caused by gravitational radiation [12].

Later, different groups built up gravitational wave detectors based on Weber's design. They improved the sensitivity by operating the detectors at cryogenic temperatures (liquid helium at 4 K and later at ultra-low temperatures below 100 mK) and implementing an improved vibration isolation and a resonant transducer. Several detectors are currently operated throughout the world with sensitivities between $3 \cdot 10^{-19}$ to $7 \cdot 10^{-19}$. An overview is given in Table 1.1.

1.3.3. Interferometric Measurements

Another alternative gravitational wave detector design is using highly sensitive laser interferometry in order to measure changes in distance between widely separated proof masses. The principle of its operation is shown in Fig. 1.4 based on a Michelson interferometer. The laser light is split at a beamsplitter, both beams are reflected at mirrored proof masses and superimposed at the initial beamsplitter. The interference of the two returned beams is detected at a photodiode. Any differential change of the distance of the proof masses – e.g. caused by a gravitational wave – causes a change in the interferometer signal. Because of their quadrupole nature, gravitational waves propagating perpendicular to the plane of the interferometer will at the same time increase the length of one interferometer arm and decrease the length of the other interferometer arm. This exactly matches the geometry of the Michelson

name	location	bar material	operating temperature	reference
Allegro	Baton Rouge, LA, USA	Al	4 K	[14]
Altair	Frascati, Italy	Al	2 K	[15]
Auriga	Lengaro, Italy	Al	100 mK	[7]
Explorer	CERN, Switzerland	Al	2.6 K	[16]
Nautilus	Rome, Italy	Al	100 mK	[17]
Niobe	Perth, Australia	Nb	5 K	[18]

Table 1.1.: Currently operating resonant bar detectors for gravitational wave detection. The Explorer detector is operated by the same group as the Nautilus detector in Rome.

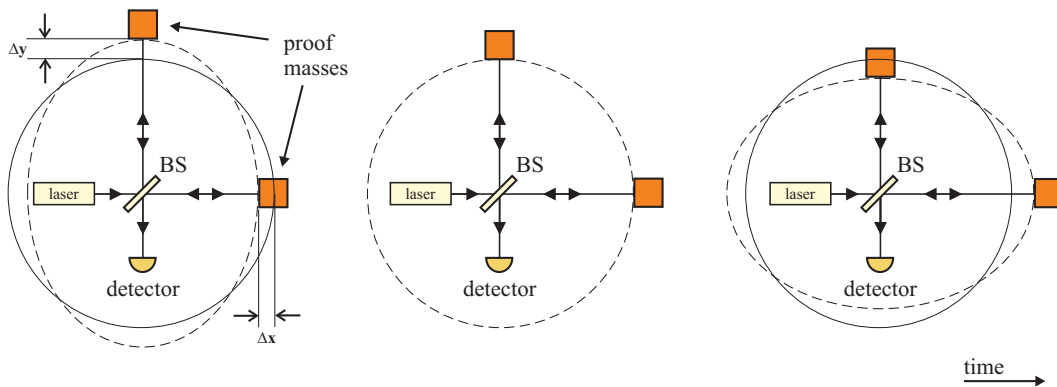


Figure 1.4.: Effect of a gravitational wave on a ring of free masses. The interferometer measures the changes in distance.

interferometer.

The ideal arm length of the interferometer equals half the wavelength of the gravitational wave. For a gravitational wave with a frequency of 100 Hz this corresponds to an interferometer armlength of 1500 km. Ground-based detectors can only realize limited armlengths of up to several kilometers and therefore must perform a very sensitive phase measurement. Several ground-based detectors based on interferometry are on the way to achieve the designed sensitivities, an overview over current projects is given in Table 1.2. Gravitational waves with frequencies below ~ 10 Hz are not accessible by ground-based detectors due to gravity gradient noise on Earth (caused e.g. by seismic activity, moving people and animals, passing clouds) [19, 20].

In order to surpass these limitations for the detection of low-frequency gravita-

name	location	armlength
GEO600	Hannover, Germany	600 m
LIGO (Hanford)	Hanford, WA, USA	2 km and 4 km
LIGO (Livingston)	Livingston, LA, USA	4 km
TAMA	Mitaka, Japan	300 m
VIRGO	near Pisa, Italy	3 km
AIGO	near Perth, Australia	80 m

Table 1.2.: Currently operated ground-based gravitational wave detectors using laser interferometry.

tional waves, space-based detectors are planned. The Laser Interferometer Space Antenna (LISA) [21, 22] has an armlength of 5 million kilometers and will detect gravitational waves in the frequency band of $30\mu\text{Hz}$ to 1 Hz. The LISA mission concept will be detailed in the following chapter. A more extensive review on interferometric gravitational wave detectors can be found in [23, 24].

2. The LISA Mission Metrology Concept

First plans for a spaceborne gravitational wave detector were already proposed in the 1980s. European and American scientists both proposed space missions dedicated to the detection of gravitational waves in the low frequency band below 1 Hz utilizing high-sensitivity interferometric laser distance metrology between distant spacecraft. In 1993 the mission LISA (Laser Interferometer Space Antenna) was proposed by a team of European and US scientists to the European Space Agency (ESA) as a medium-size M3 mission candidate within ESA's space science programme 'Horizon 2000'. Because of the cost, LISA was later included as the third Cornerstone mission in the ESA 'Horizon 2000 Plus' programme and proposed to be carried out in a collaboration with the National Aeronautics and Space Administration (NASA) [21, 22]. In 1998 a LISA mission concept study [25] and a pre-phase A study [3] were performed and in the period from June 1999 to February 2000 a LISA mission concept study was carried out by Dornier Satellitensysteme GmbH (now Astrium GmbH, Friedrichshafen, Germany) [26, 27]. Since 2004 the LISA mission formulation phase study is work in progress lead by Astrium GmbH (Friedrichshafen) on behalf of ESA. During the years the mission design concept was adopted. The LISA design detailed in the following is based on the current baseline design as developed in the mission formulation phase.

2.1. Overall Mission Concept

Planned to be launched around 2019 LISA aims at detecting gravitational waves in the low frequency range $30 \mu\text{Hz}$ to 1 Hz. Its strain sensitivity curve is shown in Fig. 2.1 enabling the detection of gravitational waves caused e.g. by neutron star binaries, white dwarf binaries, super-massive black hole binaries and super-massive black hole formations, cf. chapter 1.2. At frequencies below 3 mHz the LISA sensitivity is limited by proof mass acceleration noise and at mid-frequencies around 3 mHz by shot noise and optical-path measurement errors. The curve rises at higher frequencies as the wavelength of the gravitational wave becomes shorter than the armlength of the LISA interferometer.

The LISA mission consists of three identical spacecraft which form an equilateral

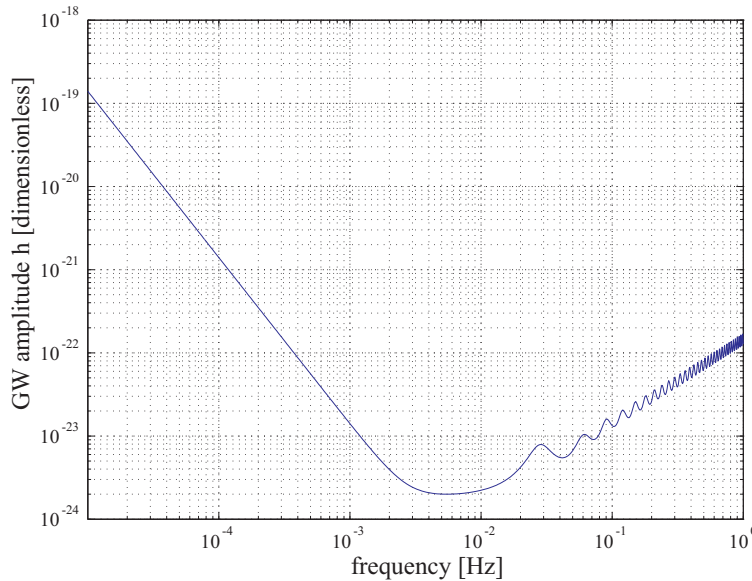


Figure 2.1.: LISA sensitivity curve given in the gravitational wave amplitude h . The curve is generated by use of the LISA Sensitivity Curve Generator [28].

triangle in a heliocentric Earth-trailing orbit with an edge length of approx. 5 million kilometers. The formation is flying $\sim 20^\circ$ behind the Earth, corresponding to a distance of ~ 50 million kilometers to Earth, cf. Fig. 2.2. This orbit is a compromise between the needed electric power for data transmission to Earth, the influence of gravitational effects caused by the Earth and the need in propulsion and time for the spacecraft to reach their final position. The plane of the three spacecraft is inclined at 60° with respect to the ecliptic. The triangular formation – with a nominally 60° angle – is mainly maintained with a slow variation of the order of $\pm 0.6^\circ$ over the annual orbit. The individual orbits of the three satellites cause the spacecraft constellation to rotate about its center one time per year.

Any combination of two arms of the LISA triangle forms a Michelson interferometer with an armlength of about 5 million kilometer. Gravitational waves passing the LISA formation will be measured as changes in the length of the interferometer arms by use of laser interferometry with $\sim 10 \text{ pm}/\sqrt{\text{Hz}}$ sensitivity. Each satellite contains two optical benches and two telescopes, which are orientated 60° to each other and form the Y-structure of the spacecraft (cf. Fig. 2.3). The telescopes have a diameter of 40 cm and are used for sending the outgoing laser beam to the distant spacecraft as well as for collecting the incoming laser light from the distant spacecraft. A laser power of 1 W is sent to the distant spacecraft where only 150 pW are collected due to diffraction losses and the limited telescope diameter. While

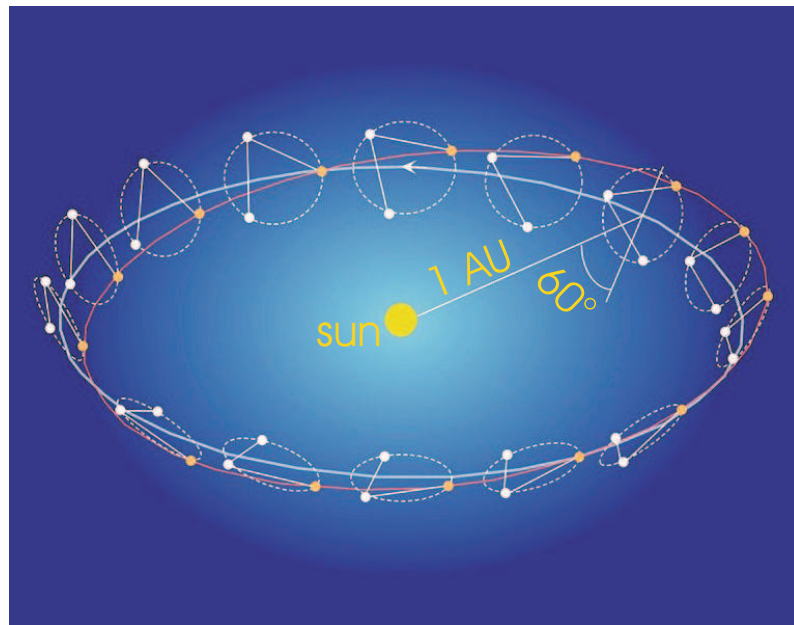


Figure 2.2.: The three LISA spacecraft are flying in a heliocentric orbit, 20° behind the Earth. (In this schematic, the LISA triangle is enlarged by a factor of 10).

in a classical Michelson interferometer, the incoming beam is reflected at the measurement mirror (and reference mirror, respectively), LISA utilizes a transponder scheme where the laser on the distant spacecraft is phase-locked to the incoming laser light and 1 W laser power is transmitted back [29]. This laser light is superimposed on the initial spacecraft with part of the original laser beam (local oscillator, LO). Due to relative velocities of the three spacecraft, the laser frequencies are Doppler shifted, resulting in a heterodyne signal on the photodiode which frequency is varying between 5 and 20 MHz over the spacecraft's orbit. The phase measurement of this heterodyne signal gives the information about changes in length of one interferometer arm. A similar measurement is performed for each arm, where the difference between the phase measurements of two single arms yields the information about the relative change in two arms. This measurement then corresponds to the gravitational wave signal. Here, laser frequency variations would cancel in the phase measurement in case of interferometer arms exactly equal in length. Due to annual variations in the orbits of the three LISA spacecraft, laser frequency variations do not totally cancel. For frequency variation and noise suppression, additional techniques are utilized: (i) laser frequency stabilization to an optical cavity; (ii) laser frequency stabilization to the (well defined) 5 million kilometer arm length (the so-called 'arm locking' [30, 31]); (iii) on-ground post-processing using 'time

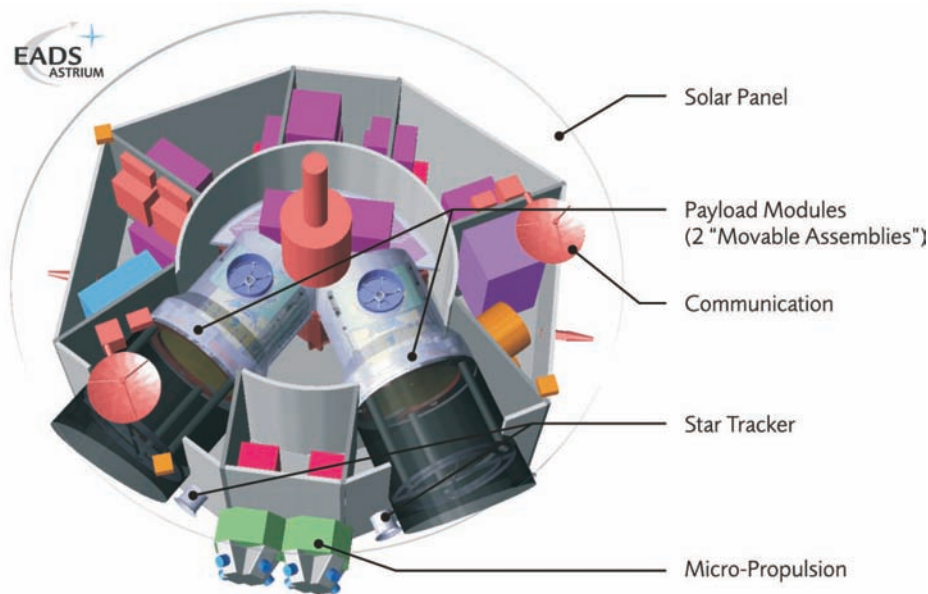


Figure 2.3.: Schematic of the LISA spacecraft. The two telescopes (movable assemblies; together with the – vertically mounted – optical bench) are oriented 60° to each other and point to the distant spacecraft.

delay interferometry’ [32, 33].

Two free flying proof masses on each satellite represent the end mirrors of the interferometer. Placed inside the satellite, they are shielded against external disturbances which ensures the unperturbed environment for the gravitational wave detection. Additionally, one of the proof masses acts as inertial reference for the satellite orbit (‘drag-free attitude control system’, cf. chapter 2.4). In the current baseline design, the laser light coming from the distant spacecraft is not directly reflected by the proof mass, but the (heterodyne) beat signal with the local oscillator is measured on the optical bench. In addition, the distance between optical bench and its associated proof mass has to be measured with the same accuracy as in the distant spacecraft interferometry. In this so-called strap-down architecture (cf. Fig. 2.4 and [34, 35]), the interferometric measurement of one interferometer arm is split into three technically and functionally decoupled measurements, easing the AIV (assembly, integration, verification) process:

- measurement between proof mass and optical bench on one spacecraft: d_1
- measurement between two optical benches on two distant spacecraft over the distance of 5 million kilometers: d_{12}
- measurement between optical bench and proof mass on the distant spacecraft: d_2

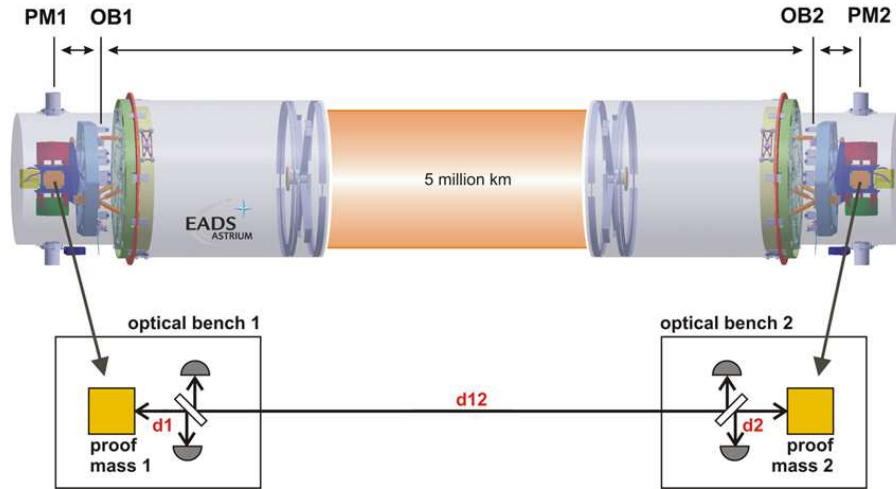


Figure 2.4.: Schematic of the strap-down architecture. The interferometer measuring the gravitational waves is split into three functionally decoupled interferometric measurements.

The science measurement (i.e. the interferometric measurement for detecting gravitational waves) is then given by:

$$d_{science} = d_1 + d_{12} + d_2. \quad (2.1)$$

The measurement of d_1 and d_2 is referred to as ‘Optical Readout (ORO)’, the measurement of d_{12} represents the spacecraft-to-spacecraft link.

The performance requirements of the three interferometric measurements are the same and given in Table 2.1.

In order to test critical subsystems for LISA, a technology demonstration precursor mission – called LISA Pathfinder – will be launched around 2010 carrying two payloads: the European ‘LISA Technology Package (LTP)’ and the American ‘Disturbance Reduction System (DRS)’. Its main objectives are to demonstrate drag-free control of a satellite with two proof masses within an acceleration noise of $3 \cdot 10^{-14} [1 - (f/3\text{mHz})^2] \text{ms}^{-2}/\sqrt{\text{Hz}}$ (i.e. a factor 7 less stringent than the LISA requirements), to test the feasibility of laser interferometry between two free flying proof masses with a sensitivity needed for LISA and to demonstrate the functionality of micro-Newton thrusters in orbit [36, 37]. LISA pathfinder consists of one spacecraft with two free flying proof masses, separated by a distance of approximately 30 cm.

relative displacement between spacecraft and proof mass (sensitive axis)	$1 \cdot 10^{-12} \sqrt{1 + \left(\frac{2.8\text{mHz}}{f}\right)^4} \text{ m}/\sqrt{\text{Hz}}$
dynamic range (sensitive axis)	$\pm 50 \mu\text{m}$
tilt noise (sensitive angles)	$10^{-8} \sqrt{1 + \left(\frac{2.8\text{mHz}}{f}\right)^4} \text{ rad}/\sqrt{\text{Hz}}$
dynamic range (sensitive angles)	$\pm 100 \mu\text{rad}$

Table 2.1.: LISA requirements for the interferometric measurements as part of the strap-down architecture [26]. The sensitive axis corresponds to the line of sight of two facing telescopes on two distant spacecraft.

2.2. The LISA Optical Bench design

Each LISA satellite payload exists of two identical so-called ‘movable optical assemblies’, consisting of a Cassegrain telescope, an optical bench (OB) and an inertial sensor, cf. Fig. 2.5. The nominal 60° angle between the two assemblies can be varied by use of ultra-low-noise actuators. This is necessary due to ‘breathing’ of the LISA triangle in orbit (changing distances and angles between the spacecraft).

The cubic proof mass is made of a Au-Pt alloy with very low magnetic susceptibility and high mass. It is surrounded by the electrode housing used for electrostatic readout and actuation of the proof mass position. The housing itself is encaged by a vacuum enclosure. The Cassegrain telescope has an aperture of 400 mm and a magnification of 80. The two mirrors M1 and M2 have a distance of 450 mm where the spacer is a tube made of CFRP (carbon-fiber reinforced plastics).

The schematic of the optical bench is shown in Fig. 2.6. It is vertically mounted behind the telescope, as seen in Fig. 2.5. Its baseplate is a 40 mm thick Zerodur hexagon, the optical components are made out of fused silica and connected to the baseplate via the method of hydroxide-catalysis bonding [38]. The optical bench will be operated at room temperature with a stability of $\approx 10^{-5} \text{ K}/\sqrt{\text{Hz}}$. The folding mirror in the middle of the optical bench is the interface to the telescope and to the proof mass – both optical axes coincide. Three interferometers are implemented: the optical readout of the proof mass (PM optical readout), the science interferometer (measuring changes in distance between two separated spacecraft) and the reference interferometer (measuring the phase between local oscillator LO1 and LO2 on the optical bench). All detectors are quadrant photodiodes used for differential wavefront sensing (see chapter 4.7) and also for alignment purposes. Additionally, power monitor photodiodes and CCD cameras for acquisition of the incoming beam are placed on the optical bench.

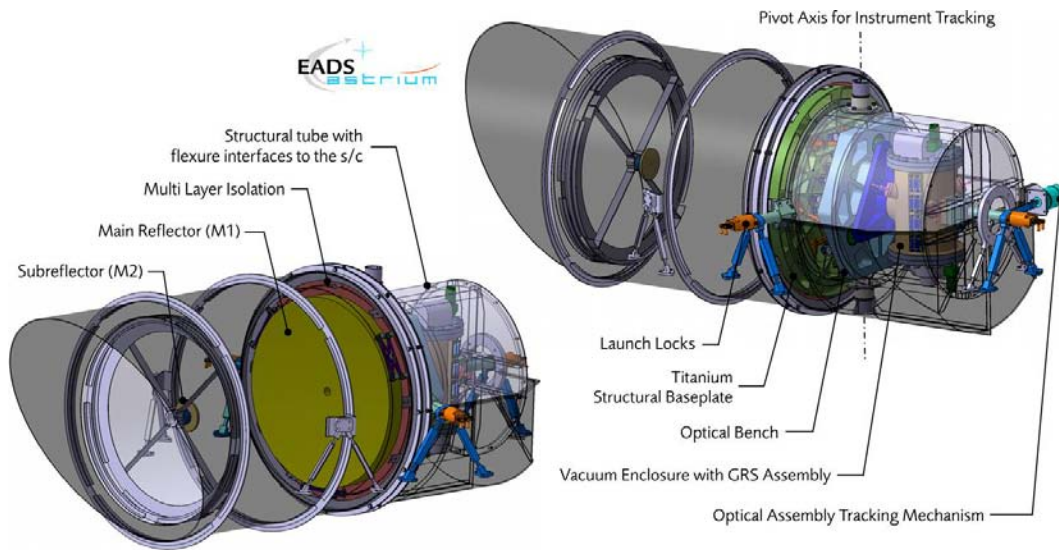


Figure 2.5.: Schematic of the LISA payload module ('movable optical assembly'). Shown are the telescope, the optical bench and the inertial sensor assembly.

The optical bench also includes an ultra-low-noise gimbal actuator (Point-Ahead Angle Mechanism, PAA) which corrects the angle of the incoming beam in order to achieve maximum contrast on the photodiode. The angle is varying with the annual orbit of the satellites.

The current baseline laser source is a non-planar ring-oscillator (NPRO, [39]) Nd:YAG laser at a wavelength of 1064 nm which intrinsically offers high intensity and frequency stability. The required output power is 2 W using a bulk or fiber amplifier. Each LISA satellite carries 2 phase-locked laser systems (plus 2 for redundancy) which are placed separately and sent to the optical bench using optical fibers.

2.3. The LISA Gravitational Reference Sensor

Each spacecraft contains two gravitational reference sensors (inertial sensors), consisting of a free flying proof mass with its housing and vacuum enclosure. Each proof mass is representing the end mirror of an interferometer arm. Also, one proof mass of each satellite is used as inertial reference for the drag-free attitude control system (DFACS, cf. chapter 2.4) of the spacecraft.

The proof mass is placed inside an electrode housing with six capacitive readouts to measure position and attitude of the proof mass. The sensor can be used in two different modes:

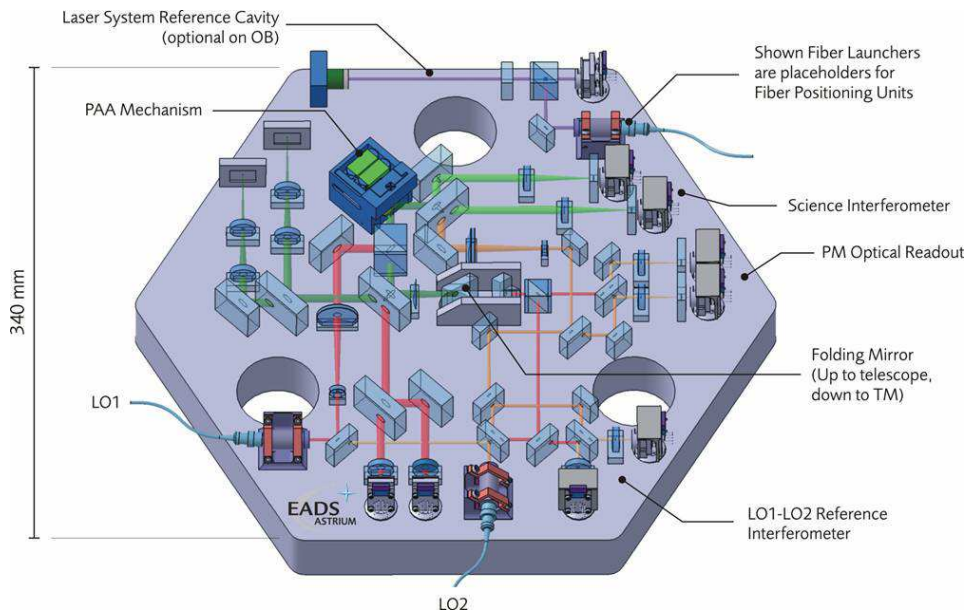


Figure 2.6.: Schematic of the LISA Optical Bench. (LO: local oscillator; PAA: point ahead angle-actuator; OB: optical bench)

- The inertial reference is free flying and the the capacitive position sensors provide information of its position and attitude with respect to the sensor cage.
- The sensor can be operated as accelerometer where the proof mass is servo-controlled in such a way that it is centered inside the housing at all times. The electrostatic forces applied to the proof mass represent the satellite acceleration.

Both modes will be used during the LISA mission in order to compensate for external perturbations.

The proof mass has a dimension of $46 \text{ mm} \times 46 \text{ mm} \times 46 \text{ mm}$ and is made out of a 75% Au and 25% Pt alloy because of its high density of 20 g/cm^3 and its weak magnetic susceptibility. The low susceptibility minimizes effects of a variation of the magnetic environment, induced by interplanetary magnetic fields or by the magnetic field gradient caused by the satellite itself. The surface of the proof mass is coated with a thin gold layer in order to provide sufficient reflectivity for the laser interferometer. A photograph of the gravity reference sensor for LTP is shown in Fig. 2.7. The same design is intended to be used aboard the LISA satellites.

The sensor includes a capacitive readout of the proof mass position and tilt (6 DOF). The sensitive axis for the science measurement, i.e. the axis aligned with the line of sight of the telescope and therefore with the proof mass on the distant

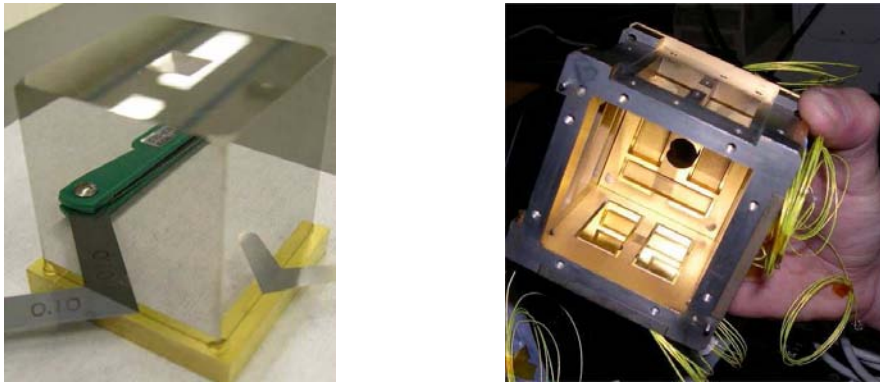


Figure 2.7.: Photograph of the LTP gravitational reference sensor prototype consisting of a proof mass (left) and the corresponding electrode housing (right) [36].

spacecraft, has an additional optical link for the LISA science measurement. The sensor also includes injection electrodes for charge control of the proof mass. The emitted ultra-violet light will release photoelectrons from the proof mass surfaces. During launch, the proof mass must be clamped. The caging mechanism must have access to the proof mass and will most probably use piezo electric actuators.

2.4. Drag-Free Attitude Control System (DFACS)

External disturbances like solar radiation pressure or solar wind will change the position of the spacecraft and thereby affect the interferometer signals caused by gravitational waves. Therefore, a free-flying proof mass inside the satellite is taken as reference for a purely gravitational orbit of the satellite. As the external disturbances only act on the surface of the satellite, the distance between the proof mass and its housing (which is rigidly connected to the satellite) is changing. In case of a drag-free controlled satellite, any change of the proof mass position is measured and the satellite is controlled in such a way that it is centered around the proof mass at any time, canceling all non-gravitational forces acting on the spacecraft (drag-free attitude control system, DFACS). The actuation of the satellite can be done e.g. by miniaturized ion engines as part of a so-called μ -propulsion system. While external disturbances are repelled, interacting forces between the satellite and the proof mass are still present and must be controlled – in case of LISA – to a 10^{-15} m/s^2 level. Such forces are e.g. the gravitational force caused by the satellite acting on the proof mass, and forces due to electrostatic charge of the proof mass and gradients in magnetic fields.

Drag free control of a satellite was first demonstrated in space 1972 aboard the

relative displacement between S/C and proof mass (sensitive axis)	$2.5 \cdot 10^{-9} \text{ m}/\sqrt{\text{Hz}}$
relative displacement between S/C and proof mass (transverse axes)	$10 \cdot 10^{-9} \text{ m}/\sqrt{\text{Hz}}$
absolute displacement measurement between S/C and proof mass	$5 \mu\text{m}$
proof mass acceleration noise (along the sensitive axis)	$3 \cdot 10^{-15} \sqrt{1 + \left(\frac{f}{8\text{mHz}}\right)^4} \text{ m/s}^2/\sqrt{\text{Hz}}$

Table 2.2.: DFACS requirements for LISA. The displacement requirements are flat in the LISA measurement band [26].

US Navy TRIAD 1 spacecraft where the residual disturbances to the proof mass were $5 \cdot 10^{-12}g$ (for 3 day tracking time) [40]. Since then, the drag-free control became a standard space technology enabling several space missions with ever increasing sensitivity. Examples are the Earth gravity missions GRACE and GOCE and the equivalence principle test mission Gravity Probe B. DFACS will also be implemented aboard LISA Pathfinder.

In case of LISA, the proof mass is a 46 mm cube¹. It is surrounded by a housing which includes all electrodes needed for a capacitive position readout, which is current baseline for LISA. The gap between housing and proof mass measures 3 to 4 mm. The capacitive readout provides the translation and tilt information of the proof mass with respect to the housing, i.e. the input signals for the drag-free control feedback loop. The requirements for the LISA DFACS position sensor are given in Table 2.2.

¹The cubic proof mass is the current baseline but a spherical proof mass is a possible alternative still under investigation [41, 42].

3. The LISA Gravitational Reference Sensor Readout

The design of the LISA gravitational reference sensor assembly was given in the previous chapter. The requirements for drag free control of the satellite and for the science measurement are summarized in Table 3.1. In the following, different methods for position and tilt metrology of the free flying proof masses are detailed and compared. Here, both applications – as sensor for the drag-free control and as part of the science interferometer – are taken into consideration. A system fulfilling the requirements for the science interferometer can always be taken as a redundant and independent back-up solution for the drag-free sensor. The equations in the following are mainly given in order to show the relevant parameters and their dependencies.

For a drag-free control loop, the residual proof mass acceleration can be written as (cf. e.g. [43])

$$a_n = \frac{f_{str}}{m} + \omega_p^2 \left(x_n + \frac{F_{ext}}{M\omega_{DF}^2} \right), \quad (3.1)$$

where m is the mass of the proof mass and M the mass of the spacecraft. f_{str} are stray forces which are independent of the proof mass position (e.g. imperfect shielding of environmental disturbances and disturbances caused by the satellite itself). x_n is the position sensing noise (sensor noise), F_{ext} are external forces acting on the spacecraft. Both result in an acceleration contribution coupled by $\omega_p^2 = k_p/m$, where k_p is a (parasitic) spring constant. The term $F_{ext}/M\omega_{DF}^2$ is caused by the finite time response of the drag free control loop.

3.1. Capacitive Readout

Current baseline for the DFACS position sensor is a capacitive readout where the proof mass is surrounded by several electrodes that sense the motion of proof mass along its six degrees of freedom. The electrodes are connected to the so-called housing which is rigidly fixed to the satellite structure. In general, the capacity of a

	DFACS	science interferometer
relative displacement between S/C and proof mass (sensitive axis)	$2.5 \cdot 10^{-9} \text{ m}/\sqrt{\text{Hz}}$	$1 \cdot 10^{-12} \text{ m}/\sqrt{\text{Hz}}$
relative tilt between S/C and proof mass (sensitive axis)	$2 \cdot 10^{-7} \text{ rad}/\sqrt{\text{Hz}}$	$10^{-8} \text{ rad}/\sqrt{\text{Hz}}$
proof mass acceleration noise (along the sensitive axis)	$3 \cdot 10^{-15} \text{ m/s}^2/\sqrt{\text{Hz}}$	

Table 3.1.: Requirements for the LISA inertial sensor readout. The frequency dependencies can be found in Table 2.1 and Table 2.2.

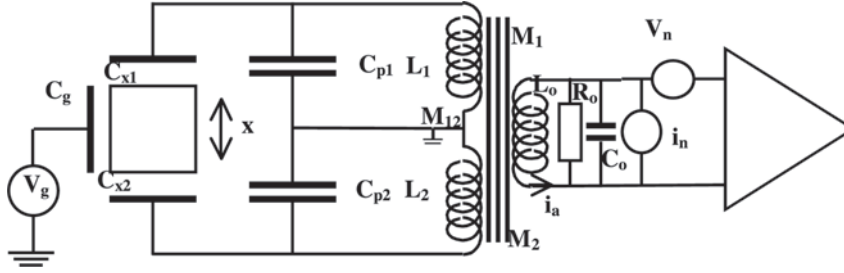


Figure 3.1.: Schematic of a capacitive proof mass position readout using a resonant capacitive-inductive bridge [45].

plate capacitor is given by

$$C = \epsilon \cdot \frac{A}{d}, \quad (3.2)$$

where A is the surface area of the electrode, d the gap between the two electrodes (i.e. the distance between housing and proof mass) and ϵ the permittivity of the material between the two electrodes (ϵ_0 in case of free space in vacuum). A schematic of the capacitive readout for LISA is shown in Fig. 3.1, representing a differential capacitive-inductive bridge. The capacities C_{p1} and C_{p2} are equal, the inductances L_1 and L_2 are equal and an injection electrode applies a sine wave voltage V_g to the proof mass at the resonance frequency $\omega_0 \approx 1/\sqrt{2LC_{p1}} \approx 2\pi \cdot 100 \text{ kHz}$. In ground tests, a sensitivity of $2 \text{ nm}/\sqrt{\text{Hz}}$ in displacement and $200 \text{ nrad}/\sqrt{\text{Hz}}$ in rotation measurement was achieved, fulfilling the LISA DFACS requirements [44]. The same electrodes can also be used to apply an electrostatic force to the proof mass.

The injection electrodes also control electrostatic charging of the proof mass due

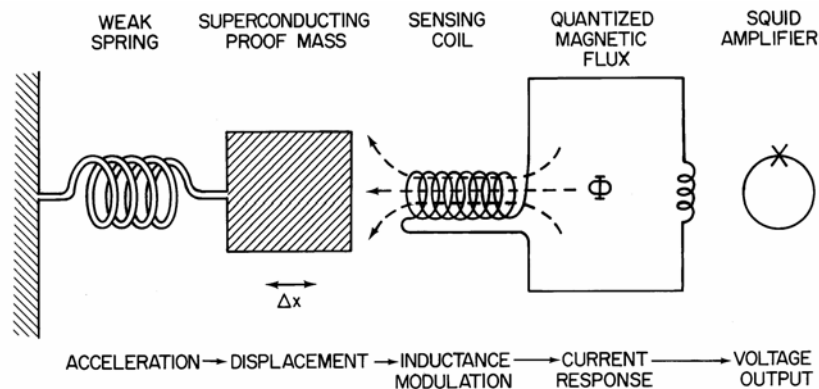


Figure 3.2.: Schematic of a superconducting accelerometer using SQUIDs [49].

to cosmic rays. In the Star and SuperStar accelerometers developed by ONERA (France), a gold wire attached to the proof mass is used for this purpose. The induced stiffness and damping limits the resolution to several $10^{-14} \text{ m/s}^2/\sqrt{\text{Hz}}$ [46].

For a capacitive readout, a smaller gap results in a higher sensitivity of the capacity measurement but also causes a higher influence of external forces and therefore an increase in acceleration noise. The need of a small gap for a high capacity is a main limitation of a capacitive readout. Such a readout can not provide the sensitivity needed for the LISA science measurement.

3.2. SQUID-based Readout

Superconducting Quantum Interference Devices (SQUIDs) can be used for displacement sensing of a proof mass, where up to now all SQUID based accelerometers are designed as gradiometers with a certain baselength b between two proof masses. The realization is shown in Fig. 3.2 representing a differentiating SQUID transducer [47, 48]. The proof masses have superconducting sides which interact with currents in superconducting inductors. The inductors are part of an inductive bridge where the SQUID senses its imbalance.

Current sensors are utilizing low temperature superconducting (LTS) materials operated at cryogenic temperatures (4 K). High temperature superconducting (HTS) materials operated at temperatures up to 90 K are investigated and will result in no gain in performance but in a less complex technical realization. In general, problems of the SQUID based readout are its signal at low frequencies where the $1/f$ -noise of the SQUIDs is very high (due to DC coupling between sensing inductors and SQUID). Also, reliable cryogenic cooler in space are not yet available and SQUIDs show a strong thermal sensitivity of $5 \cdot 10^{-4} / \text{s}^2 / \text{K}$.

The minimum power spectral density of such a sensor (m : mass of the proof mass, b : baseline, $\omega_{res} = 2\pi f_{res}$: resonance frequency, Q : quality factor) operated at temperature T is given by [50]

$$S_{\Gamma}(f) = \frac{8}{mb^2} \left[k_B T \frac{\omega_{res}}{Q} + \frac{\omega_{res}^2}{2\beta\eta} E_A(f) \right], \quad (3.3)$$

where the first term states thermal noise and the second term SQUID noise. Here, k_B is the Boltzmann constant, η is the energy coupling efficiency from the superconducting circuit to the SQUID, β is the electromechanical energy coupling constant of the transducer, $E_A(f)$ the input energy resolution of the SQUID (current values are $E_A(f) = 5 \cdot 10^{-31} \text{ J/s}^2/\text{K}$). The best demonstrated performance is $2 \cdot 10^{-11} \text{ J/s}^2/\sqrt{\text{Hz}}$ [50].

3.3. Optical Readout

In general, various methods for an optical readout are conceivable:

- lever sensor, i.e. sensing of the proof mass position via position sensitive device (e.g. CCD camera),
- single-path interferometer: Michelson (or Mach-Zehnder) type interferometer with the proof mass representing the measurement mirror,
- multiple-path interferometer: use of optical resonators with one of the mirrors rigidly connected to the proof mass (or coated proof mass).

For an optical readout, the gap between proof mass and housing has no restriction and can be made large enough to minimize coupling forces between spacecraft and proof mass. Also, an optical readout is not directly sensitive to proof mass charging. On the other hand, a laser beam with power P_0 will perform a force $F = ma = 2P_0/c$ to the proof mass caused by radiation pressure. Therefore, two laser beams on opposing proof mass surfaces must hit the proof mass in order to cancel the forces. When allocating a residual proof mass acceleration of $\tilde{a} < 1 \cdot 10^{-16} \text{ m/s}^2/\sqrt{\text{Hz}}$ and a proof mass weight of $m = 2 \text{ kg}$, the relative power stability must obey

$$\frac{\tilde{P}}{P_0} < 3 \cdot 10^{-5} \left(\frac{1 \text{ mW}}{P_0} \right) \text{ Hz}^{-1/2}, \quad (3.4)$$

which is achievable using an active intensity stabilization.

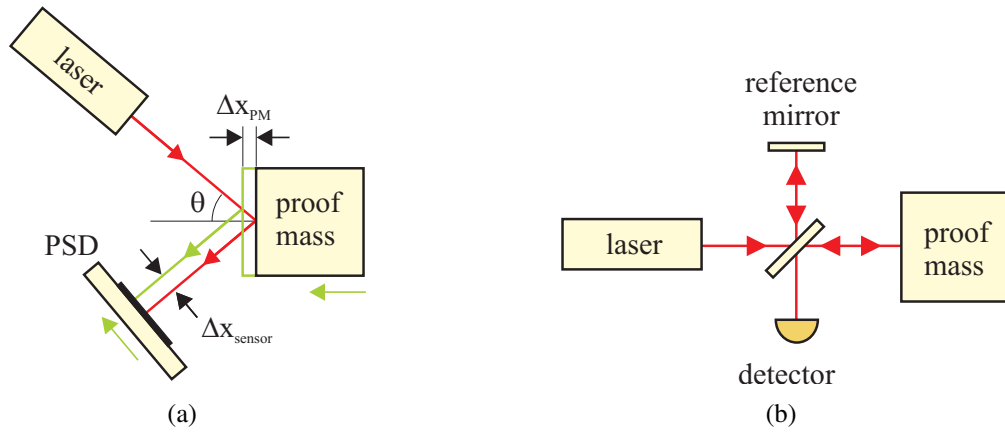


Figure 3.3.: Possible optical readout methods: (a) optical lever sensor (PSD: position sensitive device); (b) single-path interferometry.

3.3.1. Lever Sensor

This method is shown as schematic in Fig. 3.3 (a). A laser is reflected at a proof mass surface under an incidence angle θ and detected on a position sensitive device such as a CCD camera or a quadrant photodiode. A translation movement of the proof mass results in a beam displacement Δx_{sensor} on the position sensitive device:

$$\Delta x_{sensor} = 2 \sin \theta \cdot \Delta x_{PM} . \quad (3.5)$$

A tilt ϕ around an axis perpendicular to the normal of the proof mass surface results in a beam displacement measured at the position sensitive device which is dependent on the distance l between proof mass surface and position sensor:

$$\Delta x_{sensor} = 2l\phi . \quad (3.6)$$

By an appropriate sensor combination, tilt and translation can be decoupled and all 6 degrees of freedom of the proof mass can be detected.

3.3.2. Interferometric Measurement

Single-path interferometers as Michelson and Mach-Zehnder interferometers are state of the art technologies which are highly developed in a variety of different implementations. Such interferometers offer pm-accuracy – demonstrated in lab experiments. A tilt measurement can be implemented by performing a spatially resolved phase measurement, e.g. with quadrant photodiodes (Differential Wavefront Sensing, DWS [51, 52]). A schematic of a Michelson interferometer with a proof mass acting as measurement mirror is shown in Fig. 3.3 (b). A more detailed

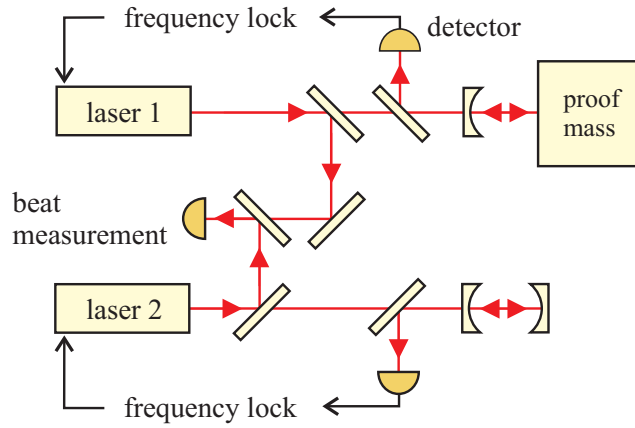


Figure 3.4.: Multiple-path interferometry.

analysis concerning single-path interferometry will be given in chapter 4.

Multiple-path interferometry, i. e. the use of optical resonators (cavities) is most promising, providing the highest sensitivity in position sensing. A possible implementation is shown in Fig. 3.4. The resonance frequency f_{res} of a cavity with length L is given by

$$f_{res} = \frac{nc}{2L}, \quad (3.7)$$

where c is the vacuum speed of light and n an integer number. A laser frequency locked to the resonance frequency of a cavity will change its frequency when the length of the resonator is changing. In case of LISA one cavity mirror will be fixed to the satellite structure (i.e. the optical bench or housing), the other mirror is rigidly fixed to the proof mass (e.g. by directly coating the proof mass surface). Locking the laser to this cavity and performing a beat measurement with a second laser which is frequency locked to a stable reference cavity will provide the information on a change in frequency of the first laser and therefore change in length L of the corresponding cavity.

Depending on the finesse of the cavity, a sensitivity up to $\sim 1 \text{ fm}/\sqrt{\text{Hz}}$ could be achieved. A tilt of the proof mass might be measured by analyzing higher order modes in the cavity. This technology is not yet demonstrated in a lab experiment and is also highly complex (use of several lasers, which are frequency stabilized to several cavities).

3.3.3. An Optical Readout Developed at the University of Napoli (Italy)

The method of a lever sensor as optical readout for the LISA inertial sensor is under investigation at the University of Napoli (Italy). Their design is based on the implementation in the current LISA pathfinder gravitational reference sensor design with its vacuum enclosure where it uses available optical accesses. The laser light is reflected twice on the electrodes (acting as mirrors) and once on the proof mass enabling a measurement of the proof mass translation and tilt. The position of the laser beam is monitored by a position sensitive device (PSD), cf. the schematic shown in Fig. 3.5. The measured power spectral density in translation measurement is also shown in Fig. 3.5. They demonstrated a displacement noise below 10^{-9} m/ $\sqrt{\text{Hz}}$ for frequencies $> 5 \cdot 10^{-3}$ Hz [53, 54]. This method can presently not provide the sensitivity needed in the LISA science interferometer but can serve as position sensor for DFACS, supporting the capacitive readout.

3.3.4. An Optical Readout Developed at the University of Birmingham (England)

For the LIGO ground-based gravitational wave detector, the University of Birmingham set up a homodyne in-quadrature interferometer utilizing polarizing optical components [55]. They developed a compact prototype using a VCSEL (Vertical Cavity Surface Emitting Laser) laser diode. Noise levels below 10^{-12} m/ $\sqrt{\text{Hz}}$ for frequencies > 10 Hz were achieved and work is currently under way to optimize their design with respect to the LISA low frequency measurement band, cf. Fig. 3.6. Due to its design, the interferometer is insensitive to a tilt of the measurement mirror.

3.3.5. An Optical Readout Developed at Stanford University (USA)

An optical readout using a Littrow resonator is developed at the University of Stanford. It is based on a LISA gravitational reference sensor design with spherical proof mass as already proposed in [26]. A double-sided grating is implemented in the housing wall enabling an internal interferometric measurement between the GRS and the proof mass (ORO) and an external interferometric measurement between the GRS and the distant spacecraft (cf. Fig. 3.7 and [57, 58, 59]). The optical setup is similar to the tunable external cavity laser diode design in Littrow configuration. A relative movement of the grating results in a change, both, in amplitude and frequency; this can be converted to a translation measurement. In a laboratory setup, a

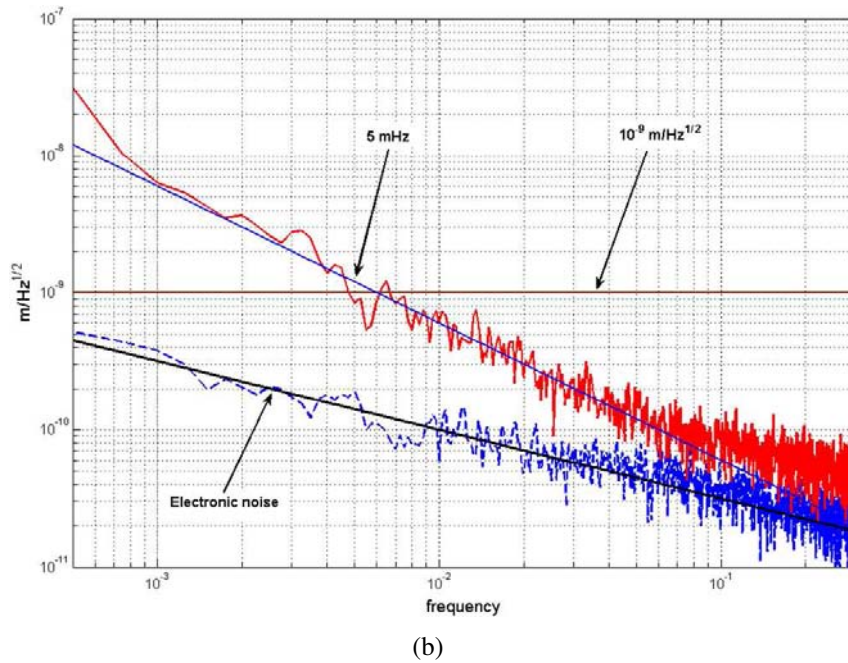
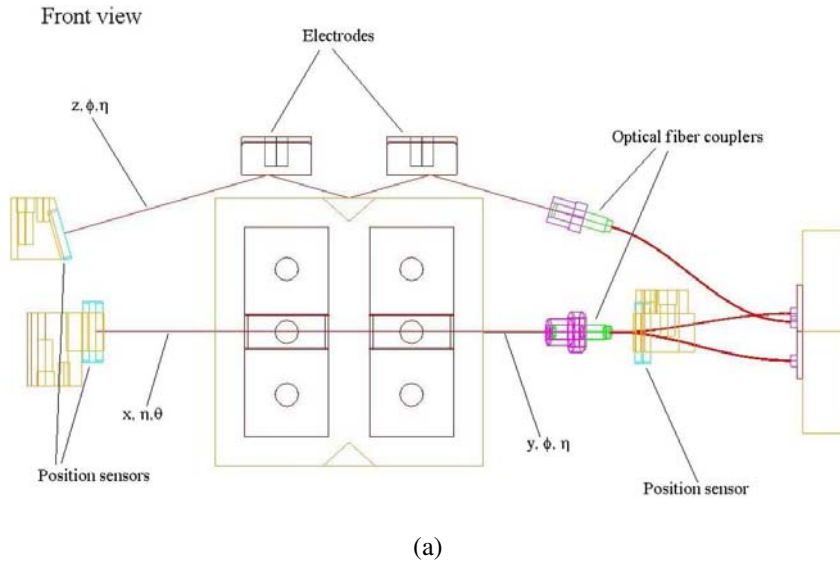
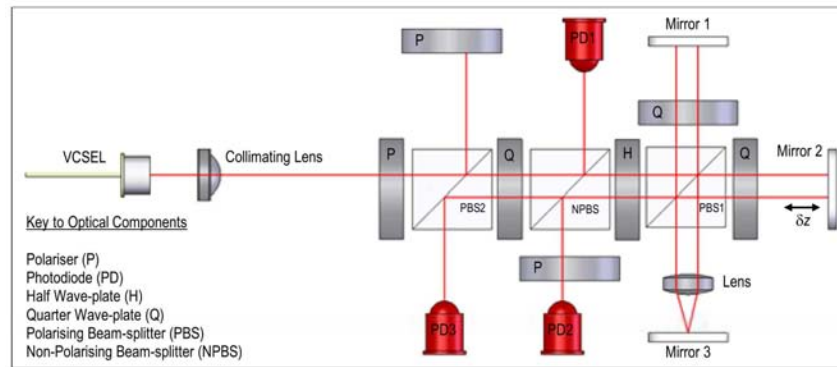
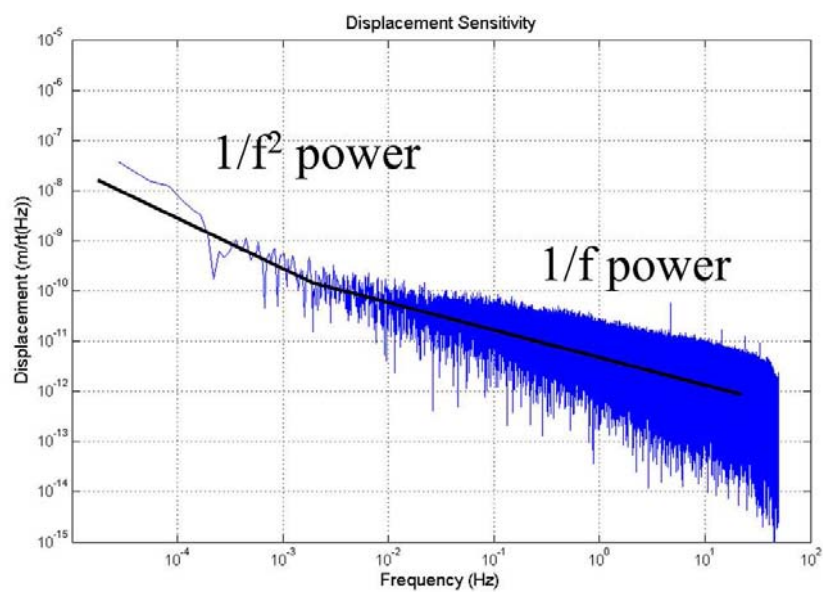


Figure 3.5.: Optical readout developed at the University of Napoli. (a) schematic of the setup, front view; (b) PSD of the measured translation [53].



(a)



(b)

Figure 3.6.: Optical readout developed at the University of Birmingham. (a) schematic of the interferometer; (b) PSD of the measured translation in the LISA frequency band [56].

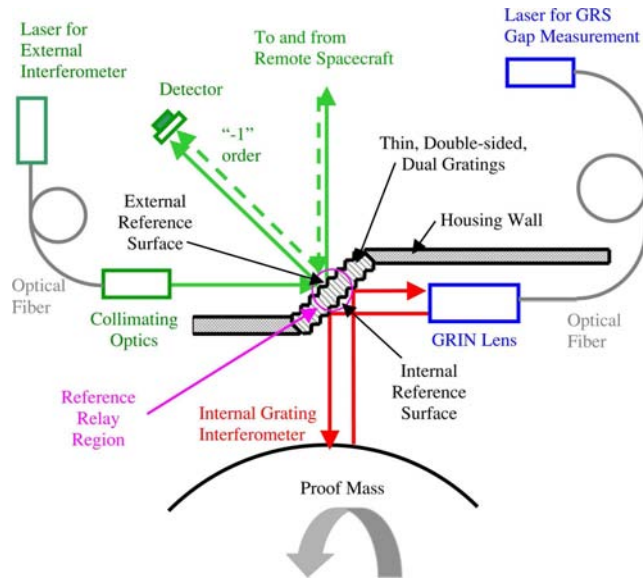


Figure 3.7.: Schematic of the optical readout developed at Stanford University [57].

preliminary sensitivity of $\sim 5 \text{ pm}/\sqrt{\text{Hz}}$ at a frequency of 1 Hz and $\sim 40 \text{ pm}/\sqrt{\text{Hz}}$ at a frequency of 0.1 Hz was measured [59].

3.3.6. The LTP Optical Readout aboard LISA Pathfinder

As part of the LISA technology package (LTP) aboard LISA Pathfinder, a heterodyne Mach-Zehnder interferometer utilizing non-polarizing optics was developed in a collaboration of the Albert-Einstein-Institute Hannover and Astrium GmbH – Satellites, Friedrichshafen [60, 61, 62]. The optical setup is realized using a Zerodur baseplate where the optical components are fixed using the method of hydroxide-catalysis bonding. Differential wavefront sensing is utilized for tilt measurement. Several interferometers are implemented on the optical bench, measuring changes in distance between the two free flying proof masses with a nominal distance of 30 cm, and changes in distance between each proof mass and the optical bench. Noise levels below $1 \text{ pm}/\sqrt{\text{Hz}}$ in translation measurement (in the frequency range 10 mHz to 0.5 Hz), and below $1 \text{ nrad}/\sqrt{\text{Hz}}$ in tilt measurement (in the frequency range 50 mHz to 10 Hz), were demonstrated [63]. A photograph of the interferometer setup, its corresponding schematic and the measured translation noise are shown in Fig. 3.8. In the measurement, the proof masses are replaced by gold mirrors.

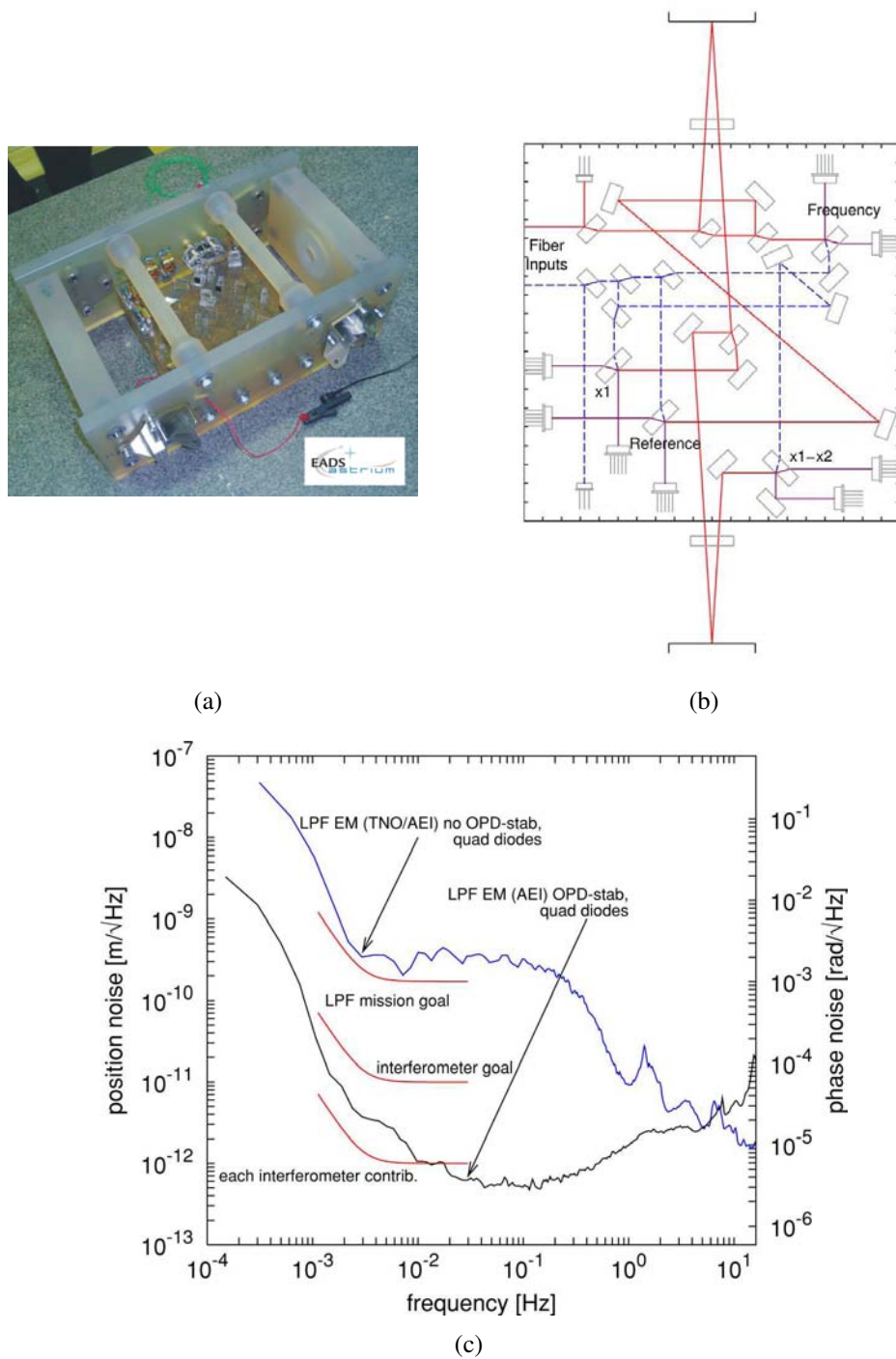


Figure 3.8.: LTP optical readout aboard LISA pathfinder (engineering model). Photograph (a) and schematic (b) of the interferometer; (c) PSD of the measured translation [60, 63].

4. Interferometric Concepts

Single-path interferometers can be sub-divided with respect to different properties:

- *homodyne vs. heterodyne detection:* That means the use of one laser frequency (homodyne interferometer) or two laser frequencies (heterodyne interferometer). The heterodyne frequency, i.e. the difference between the two laser frequencies, can be between 1 kHz and several MHz; this method offers better noise immunity than the homodyne measurement.
- *utilizing polarizing optics vs. utilizing non-polarizing optics:* Polarizing optics includes e.g. polarizing beamsplitters and retarder waveplates and always suffer from leakage of the ‘wrong’ polarization in each optical path. This polarization mixing can limit the performance of the interferometer.
- *optical path, i.e. Michelson interferometer vs. Mach-Zehnder interferometer:* In a Michelson interferometer the measurement mirror is hit under normal incidence, in a Mach-Zehnder interferometer under an angle. In a Mach-Zehnder interferometer, incoming and outgoing beam are spatially separated.

The choice of interferometer design is also based on additional design drivers as compactness (this also includes the number of optical components) and – above all – the needed performance. In this chapter, first, an overview over different interferometer techniques is given – resulting in a design trade-off for our specific application.

4.1. Interferometer Basics

The most basic interferometer is the Michelson interferometer shown in Fig. 4.1. A laser beam is split at a (non-) polarizing beamsplitter where one part is reflected at the reference mirror and the other part at the measurement mirror. Both beams are superimposed at the same beamsplitter and hit a detector.

The electric fields of the reference and measurement beams are given by

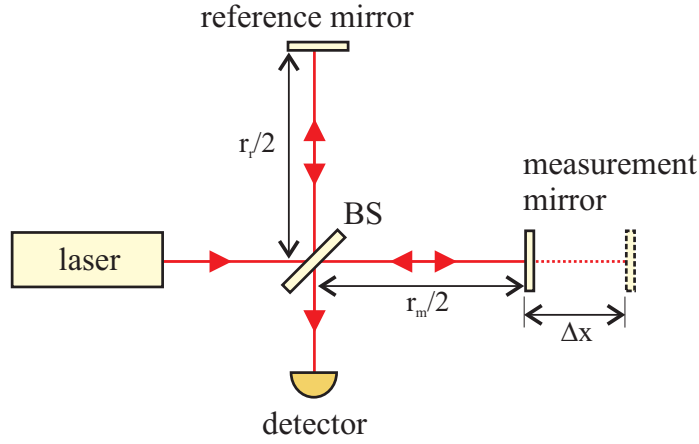


Figure 4.1.: Schematic of a Michelson interferometer (BS: beamsplitter).

$$E_{ref} = E_r \cdot e^{i(\omega t + \vec{k}\vec{r}_r - \phi_r)} \quad (4.1)$$

$$E_{meas} = E_m \cdot e^{i(\omega t + \vec{k}\vec{r}_m - \phi_m)}, \quad (4.2)$$

where E_r and E_m are the amplitudes of the electric fields, ω is the angular frequency, t the time, $|\vec{k}| = 2\pi/\lambda$ the propagation vector, \vec{r} the position vector (i.e. the optical path traveled in the reference and measurement beam, cf. Fig. 4.1) and ϕ_r and ϕ_m the initial phases of the reference and measurement beam. The light intensity measured at the photo detector is the superposition of the two electric fields (ϵ_0 : vacuum permittivity, c : vacuum speed of light):

$$\begin{aligned} I &= \epsilon_0 c \langle E^2 \rangle \\ &= \epsilon_0 c \langle E_{ref}^2 + E_{meas}^2 + 2E_{ref}E_{meas} \rangle \\ &= \frac{1}{2} \epsilon_0 c [E_r^2 + E_m^2 + 2E_r E_m \cos(k(r_m - r_r) - (\phi_m - \phi_r))] . \end{aligned} \quad (4.3)$$

Measurement and reference beam are generated by the same (coherent) source, therefore $\phi_r = \phi_m$. With $E_r = E_m$ and $I_0 = \frac{1}{2} \epsilon_0 c E_r E_m$ the interference term becomes

$$I = 2I_0 \left[1 + \cos \left(\frac{2\pi}{\lambda} (r_m - r_r) \right) \right] . \quad (4.4)$$

When the measurement mirror is moved by a distance Δx (as shown in Fig. 4.1), the optical path in the measurement arm is changing by $2n\Delta x$, where n is the refractive index of the medium, the light is traveling in. Now, the detected intensity

changes by

$$I(\Delta x) = 2I_0 \left[1 + \cos \left(\frac{2\pi}{\lambda} (2n\Delta x) \right) \right] = 4I_0 \cos^2 \left(\frac{\pi}{\lambda} (2n\Delta x) \right). \quad (4.5)$$

In case of a constant laser wavelength and a constant refractive index, this signal can be taken for measuring the change in position of the measurement mirror. Only a (relative) displacement can be measured, but no (absolute) distance. The measured intensity varies between $I_{min} = 0$ and $I_{max} = 4I_0$. When the measurement mirror is continuously moved in the same direction, the resulting intensity is varying from 'dark' to 'bright' and back to 'dark', corresponding to one so-called 'fringe'.

4.1.1. In-Quadrature Measurement

When the measurement mirror is moved continuously in one direction, the resulting signal at the detector is $\propto \cos x$. A displacement can only be measured unambiguously in a range of $\lambda/4$ in mirror displacement. When the cosine reaches maximum or minimum, it can not be specified in which direction the measurement mirror is moving.

In order to overcome this limitation in dynamic range, a so called in-quadrature measurement can be implemented. Therefore, a second signal I_{S2} , 90° out of phase with the initial signal I_{S1} is generated:

$$I_{S1} = 2I_0 \cos \left(\frac{4\pi n \Delta x}{\lambda} \right) \quad (4.6)$$

$$I_{S2} = 2I_0 \sin \left(\frac{4\pi n \Delta x}{\lambda} \right). \quad (4.7)$$

In case the first signal is at maximum or minimum, the second signal is at maximum sensitivity and yields the information of the direction of movement of the measurement mirror. With these two equation, the displacement can be calculated via

$$\Delta x = \frac{\lambda}{4\pi n} \arctan \left(\frac{I_{S2}}{I_{S1}} \right). \quad (4.8)$$

As the amplitudes I_0 drop out in equation (4.8), this phase measurement is insensitive to fluctuations in light amplitude.

4.1.2. Periodic Nonlinearities

In an ideal case, when plotting the measured interferometer signal against the mirror displacement, a straight line should result. In reality, the interferometer signal oscillates around this straight line with periodicities of one cycle per wavelength (first order nonlinearities) and two cycles per wavelength (second order nonlinearities). These nonlinearities are subject to many investigations with respect to error sources and compensation methods.

Nonlinearities occur in both, homodyne and heterodyne interferometers, where in a homodyne system only second-order nonlinearities are present. Quenelle predicted nonlinearities in a heterodyne interferometer caused by alignment errors between laser and optics [64], which were experimentally verified by Sutton in 1987 [65]. Both, first order and second order nonlinearities were observed. Many theoretical analyses [66, 67, 68, 69, 70, 71, 72, 73, 74, 75, 76] and experimental investigations [77, 66, 78, 70, 79, 80, 81, 75, 82, 83] were carried out revealing following error sources:

- polarization mixing (in a homodyne interferometer), caused by
 - leakage of the ‘wrong’ polarization through the polarizing beamsplitter
 - rotation of the polarization axis by the mirrors/retroreflectors
 - errors caused by the retarding waveplates
- frequency mixing (in a heterodyne interferometer), caused by
 - elliptic polarization of the laser
 - leakage of the ‘wrong’ polarization through the beamsplitter
 - rotation of the polarization axis by the mirrors/retroreflectors
 - misalignment of the laser polarization axis to the polarizing beamsplitter
 - errors caused by the retarding waveplates
- interference of two wavefronts with different propagation axes (caused by misalignment or optical components of poor quality)
- ghost reflection, i.e. parasitic reflections due to imperfect anti-reflection coatings of the optical components

Also, methods for compensating nonlinearities were investigated:

- measurement of the polarization state at the photodetector (i.e. measurement of the leakage component) and compensating the error by use of an optical phase compensator [84, 85]

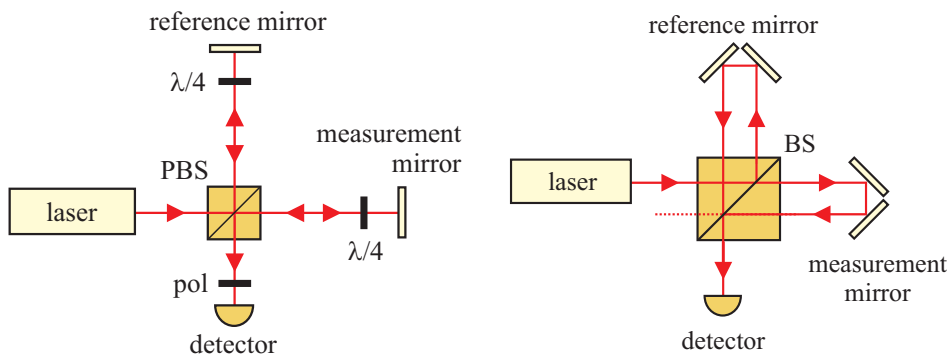


Figure 4.2.: Homodyne Michelson interferometer. Left: use of polarizing beam-splitter (PBS; pol: polarizer; $\lambda/4$: quarter waveplate); Right: use of retroreflectors.

- angular adjustments of polarizers and quarter-waveplates [86]
- phase modulation of the laser light [87, 88]
- elliptical fitting¹ [89, 90, 91, 92]

4.2. Homodyne Michelson Interferometer

The most simple Michelson interferometer is shown in Fig. 4.1 using a non-polarizing beamsplitter. The disadvantage is, that only 50 % of the light hits the detector while the other 50 % are sent directly back to the laser. Without precaution (e.g. use of a Faraday isolator) this might cause instabilities of the laser.

In order to prevent back-reflection to the laser source, two possible interferometer designs are shown in Fig. 4.2. The design on the left side shows the same setup as before where the non-polarizing beamsplitter is replaced by a polarizing one (PBS). The incoming laser beam has a linear polarization 45° to the optical baseplate. The polarization parallel to the baseplate is transmitted by the PBS while the orthogonal polarization is reflected. Both beams are passing a quarter-wave plate (resulting in circular polarized light) and are reflected at the measurement and reference mirror, respectively. After passing the quarter-wave plate for the second time they are both linearly polarized and are both outcoupled in direction of the detector at the PBS. This means, all light is sent in direction of the detector and no light is back-reflected to the laser. As both beams have orthogonal polarization, a polarizer in front of the detector is needed in order to project the two beams onto the same axis (50 % of the light intensity is lost). The design in Fig. 4.2, right, shows the use of a

¹When the two signals 4.6 and 4.7 are plotted against each other in an x-y-plot, in an ideal case a circle results. Due to nonlinearities this circle is distorted to an ellipse.

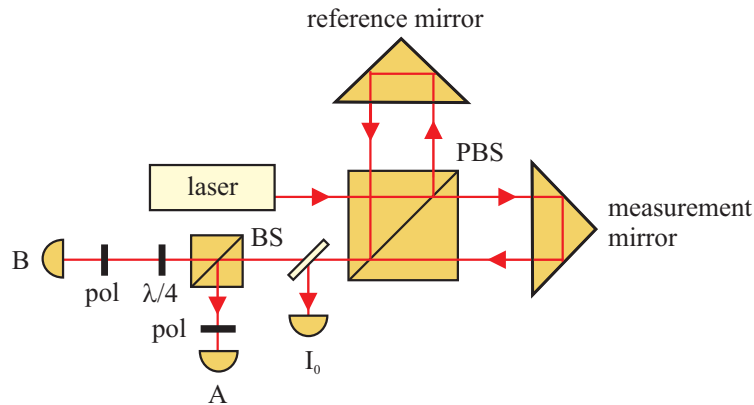


Figure 4.3.: Homodyne Michelson interferometer with in-quadrature readout. Signal I_0 is taken for power normalization.

non-polarizing beamsplitter combined with retroreflectors as measurement and reference mirrors. Therefore the incoming and the outgoing laser beams at the BS are spatially separated. Still 50% of the laser light is not used for generating the detected signal but the light can be well-defined absorbed and is not back-reflected towards the laser.

4.2.1. In-Quadrature Measurement

The generation of a second, 90° phase shifted signal is shown in Fig. 4.3. The interferometer output signal is split by a non-polarizing beamsplitter, where one signal passes an additional quarter-waveplate ($\lambda/4$) which changes the relative phase of the two linearly polarized beams by 90° . Therefore, the measured signals A and B resemble the signals proportional to \sin and \cos , as given in equations (4.6) and (4.7).

As this detection scheme is sensitive to intensity variations of the laser, an additional detector can be implemented for power normalization (cf. I_0 in Fig. 4.3).

4.3. Heterodyne Michelson Interferometer

The basic schematic of a heterodyne interferometer is shown in Fig. 4.4. The laser emits two frequencies f_1 and f_2 which are superimposed but have orthogonal polarization.

The electric field of the two beams reflected by the measurement and reference mirror are given by:

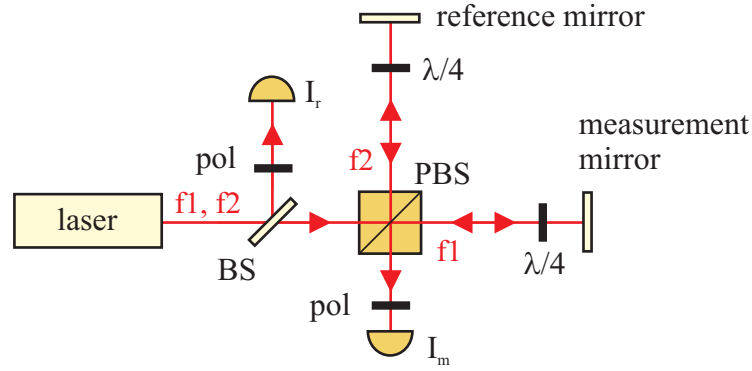


Figure 4.4.: Schematic of a heterodyne interferometer.

$$E_{meas} = E_m \cdot e^{i(2\pi f_1 t - \phi_{01} - \phi_m)} \quad (4.9)$$

$$E_{ref} = E_r \cdot e^{i(2\pi f_2 t - \phi_{02} - \phi_r)}. \quad (4.10)$$

E_r and E_m are the amplitudes of the electric fields, f_1 and f_2 are the frequencies of the measurement and reference beam, t is the time. ϕ_{01} and ϕ_{02} are the initial phases of the two light frequencies f_1 and f_2 , and ϕ_r and ϕ_m the phases in the reference and measurement arm.

Directly behind the laser, part of its light is split off and sent to a photo detector (reference signal, measuring the intensity I_r in Fig. 4.4). A polarizer in front of the detector, under 45° to both beam polarization axes, permits interference. The signal on the detector is given by:

$$\begin{aligned} I_r &= \epsilon_0 c \langle E^2 \rangle \\ &= \frac{1}{2} \epsilon_0 c [E_r^2 + E_m^2 + 2E_r E_m \cos(2\pi |f_1 - f_2| t - (\phi_{01} - \phi_{02}))]. \end{aligned} \quad (4.11)$$

A band pass filter at the heterodyne frequency $|f_1 - f_2|$ cuts off the DC part:

$$I_r = \epsilon_0 c E_r E_m \cos(2\pi |f_1 - f_2| t - (\phi_{01} - \phi_{02})). \quad (4.12)$$

The measurement signal I_m measured at the second photo detector is given by:

$$\begin{aligned}
I_m &= \varepsilon_0 c \langle E^2 \rangle \\
&= \frac{1}{2} \varepsilon_0 c [E_r^2 + E_m^2 + 2E_r E_m \cos(2\pi|f_1 - f_2|t - (\phi_{01} - \phi_{02}) - (\phi_m - \phi_r))]
\end{aligned} \tag{4.13}$$

and after band pass filtering:

$$I_m = \varepsilon_0 c E_r E_m \cos(2\pi|f_1 - f_2|t - (\phi_{01} - \phi_{02}) - (\phi_m - \phi_r)). \tag{4.14}$$

The term $\phi_m - \phi_r = \Delta\phi$ is the difference in the phase of the light waves coming from measurement mirror and reference mirror. It consists of a static term ϕ_{m0} in the measurement arm, a static term ϕ_{r0} in the reference arm and a dynamic term $\phi(t)$ caused by a movement of the measurement mirror. For a velocity $v(t)$ of the measurement mirror, it is given by

$$\begin{aligned}
\phi(t) &= 2 \frac{2\pi}{\lambda} \int dt v(t) \\
&= 2 \frac{2\pi}{\lambda} s(t).
\end{aligned} \tag{4.15}$$

The displacement $s(t)$ of the measurement mirror is directly proportional to the measured phase ϕ .

When the measurement mirror is moving with a velocity v , the frequency f_2 is Doppler-shifted by $\Delta f_{Doppler} = 2vf_2/c$. This shift in frequency states a limitation on the maximum traveling speed of the mirror.

4.3.1. In-Quadrature Measurement

For in-quadrature phase measurement, the (electronic) signal I_m is multiplied by the reference signal I_r and also by a signal exactly 90° out of phase with the reference signal. The second signal is electronically generated, e.g. by an analog phaseshifter or in a digital phasemeter by generating a synthetic second signal.

In general, for two signals $x_{RF}(t) = \cos(\omega_{RF}t)$ and $x_{LO}(t) = \cos(\omega_{LO}t)$, the multiplied signal results in

$$\begin{aligned}
x_{IF} &= x_{RF} \cdot x_{LO} \\
&= \frac{1}{2} \cos(\omega_{RF} + \omega_{LO})t + \frac{1}{2} \cos(\omega_{RF} - \omega_{LO})t,
\end{aligned} \tag{4.16}$$

where one term is at the sum frequency $\omega_{RF} + \omega_{LO}$ and one at the difference frequency $\omega_{RF} - \omega_{LO}$. The first one is not of interest and eliminated by low-pass filtering. For two input signals with the same frequency $\omega_{RF} = \omega_{LO}$, the resulting signal is proportional to the phase between the two input signals.

Multiplication and subsequent low-pass filtering of equations (4.12) and (4.14) result in

$$I_{IF} = \frac{1}{2} \epsilon_0^2 c^2 E_r^2 E_m^2 \cdot \cos(\phi_m - \phi_r). \quad (4.17)$$

In-quadrature measurement of the phase between I_r and I_m results in the two signals

$$S_1 = \frac{1}{2} \epsilon_0^2 c^2 E_r^2 E_m^2 \cos\left(\frac{4\pi n}{\lambda_1} \Delta x\right) \quad (4.18)$$

$$S_2 = \frac{1}{2} \epsilon_0^2 c^2 E_r^2 E_m^2 \sin\left(\frac{4\pi n}{\lambda_1} \Delta x\right), \quad (4.19)$$

where the phase is obtained via

$$\phi(t) = \frac{4\pi n}{\lambda_1} \Delta x = \arctan\left(\frac{S_2}{S_1}\right). \quad (4.20)$$

4.3.2. Evaluation of Periodic Nonlinearities

As given in equation (4.15), the displacement of the measurement mirror should be exactly proportional to the phase. Nonlinearities can therefore be determined by a controlled linear movement of the measurement mirror or by changing the refractive index in the measurement arm of the interferometer, e.g. by performing a pressure scan using a vacuum cell. Also a non-linear scan can be evaluated, as detailed in the following, cf [93].

For an in-quadrature measurement with signals S_1 and S_2 , the amplitude is given by

$$R(t) = [S_1^2 + S_2^2]^{1/2} \quad (4.21)$$

and the demodulated phase Φ by

$$\Phi = \arctan \frac{S_2}{S_1}. \quad (4.22)$$

In the presence of nonlinearities, the measurement signal I_m can be written as

$$I_m = \cos(2\pi|f_1 - f_2|t - \phi) + \varepsilon \cos(2\pi|f_1 - f_2|t - \delta), \quad (4.23)$$

where $\varepsilon \ll 1$ and δ are functions of ϕ . The coefficients were omitted for convenience. In this case, the in-quadrature signals become

$$S_1 = \frac{1}{2} (\cos \phi + \varepsilon \cos \delta) \quad (4.24)$$

$$S_2 = \frac{1}{2} (\sin \phi + \varepsilon \sin \delta). \quad (4.25)$$

The measured phase is then given by

$$\Phi(t) = \arctan \frac{\sin \phi + \varepsilon \sin \delta}{\cos \phi + \varepsilon \cos \delta}, \quad (4.26)$$

and expansion of this expression in ε results in

$$d\Phi = \Phi - \phi = \varepsilon \sin(\delta - \phi). \quad (4.27)$$

The amplitude as given in equation (4.21) is then

$$R = \frac{1}{2} [(\cos \phi + \varepsilon \cos \delta)^2 + (\sin \phi + \varepsilon \sin \delta)^2]^{1/2}, \quad (4.28)$$

whose expansion in ε yields to

$$\frac{dR}{R} = \varepsilon \cos(\delta - \phi). \quad (4.29)$$

When comparing equation (4.27) and equation (4.29), it can be seen that the magnitude of the phase error is the same as the magnitude of the amplitude error. Therefore, it is possible to evaluate the nonlinearities by measuring the amplitude errors, and the periodic phase error can be expressed by

$$|d\phi| = \left| \frac{dR}{R} \right| \quad (4.30)$$

and therefore

$$|dx| = \frac{\lambda}{4\pi} \left| \frac{dR}{R} \right|. \quad (4.31)$$

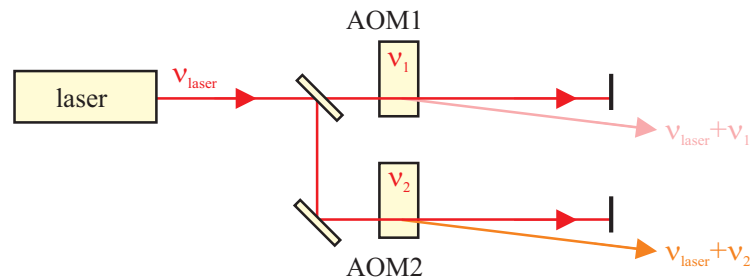


Figure 4.5.: Generation of the heterodyne frequencies by use of 2 acousto-optic modulators (AOMs).

4.3.3. Generation of Heterodyne Frequencies

The two frequencies needed for heterodyne detection can be generated by different methods:

- Use of one laser which intrinsically generates two frequencies e.g. a Zeeman laser [94, 95] or a two-longitudinal-mode laser [96]. The two frequencies are spatially overlapping and have orthogonal polarization. Heterodyne frequencies from several MHz to 100 MHz are possible.
- Use of one laser and 2 acousto-optic modulators where the first order Bragg deflections are used in the interferometer (cf. Fig. 4.5). Here, both frequencies are spatially separated and can easily adjusted by the RF-frequencies of the AOMs. Heterodyne frequencies between several kHz and several hundred MHz can be realized.
- Use of one laser and an electro-optic modulator [97].
- Use of 2 phase-locked lasers. Here, both frequencies are spatially separated as well, heterodyne frequencies between several kHz and several GHz are possible, depending on the laser source.

Beside that, the heterodyne frequency can also be realized by a (continuously) moving measurement mirror.

4.4. Mach-Zehnder Interferometer

The basic schematic of a Mach-Zehnder interferometer is shown in Fig. 4.6. The laser beam is split at a beamsplitter and both beams are recombined at a second beamsplitter before hitting a detector. The Mach-Zehnder interferometer can be realized homodyne or heterodyne, the splitting of the two frequencies can be realized using polarizing optics, cf. chapter 4.3.3.

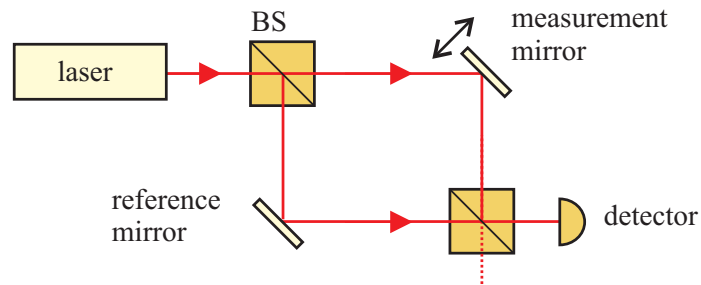


Figure 4.6.: Schematic of a Mach-Zehnder interferometer (BS: beamsplitter).

A Mach-Zehnder type interferometer can be realized using non-polarizing optics where no light is reflected back to the laser source. In contrast to the Michelson interferometer no retroreflector is needed – but the measurement mirror is hit under no-normal incident angle. This also means, that a Mach-Zehnder interferometer can only be used for small mirror displacements as the overlap of the measurement and reference beams is degraded. Also, the optical access to the measurement mirror needs to be larger.

4.5. Heterodyne Interferometer with Spatially Separated Frequencies

Frequency and polarization mixing can be avoided by spatially separating the two beams with different frequencies. The corresponding schematic is shown in Fig. 4.7, based on a design presented in [98] using non-polarizing optics. The input beams with frequencies f_1 and f_2 are first split at the beamsplitters BS1 and BS2, respectively. The beam with frequency f_1 is reflected by the measurement mirror; the beam with frequency f_2 by the reference mirror. Both beams are superimposed in front of a first detector at beamsplitter BS4 – providing the measurement signal. Correspondingly, the split-off beam with frequency f_2 is superimposed with the split-off beam with frequency f_1 in front of a second detector at beamsplitter BS3 – providing the reference signal. Both photodiode signals are heterodyne signals at the heterodyne frequency $|f_1 - f_2|$. The measurement signal gives the information of a relative movement between measurement and reference mirror. A relative change in phase between the two initial beams before their splitting at BS1 and BS2 is measured by the reference signal. With a fixed reference mirror, the phase comparison between the two detector signals yields the information of a measurement mirror movement. All phase effects taking place before the initial beamsplitters (BS1 and BS2) are common-mode to both detector signals and therefore canceled.

The advantages of this design are:

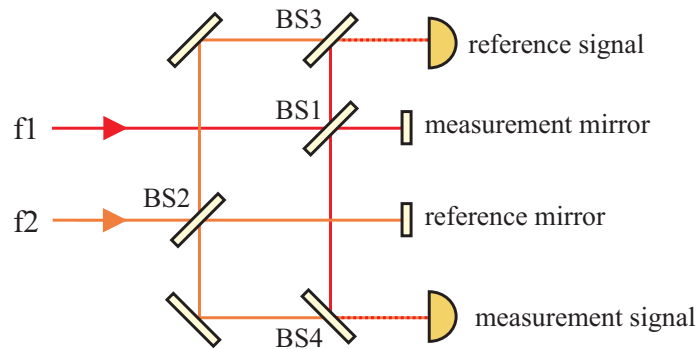


Figure 4.7.: Schematic of a heterodyne interferometer with spatially separated frequencies. All optics are non-polarizing.

- Both frequencies are spatially separated and therefore no polarization and frequency mixing occurs.
- Measurement and reference arm can be designed highly symmetrically (with respect to optical path length). Therefore common-mode errors are suppressed.

4.6. A Heterodyne Interferometer Design as LISA Optical Readout

As most suitable for our LISA application with required pm-sensitivity² we have chosen an interferometer layout based on a design by Wu et al. [93, 99, 100]. It represents a heterodyne interferometer with two spatially separated beams with frequencies f_1 and f_2 , cf. the schematic shown in Fig. 4.8. The design of this interferometer is based on maximum symmetry between reference and measurement arm of the interferometer. Both have the same polarization and frequency. In front of the photodiodes, they are superimposed with the second frequency in order to generate the heterodyne beat signal. This design also takes care that the optical paths of the reference and measurement arm are the same (especially the same distances traveled in optical elements). Therefore, common-mode distortions and frequency noise are maximally rejected and polarization mixing is in principle avoided.

The electric fields of the 4 beams as shown in Fig. 4.8 are given by

²The LISA requirements for the optical readout are given in Table 2.1 and Table 2.2. A 1 pm sensitivity corresponds to a phase sensitivity of $1.3 \cdot 10^{-5}$ rad (at a laser wavelength of $1064 \mu\text{m}$).

$$E_m = E_{0,m} e^{i(2\pi f_1 t + \vec{k}_1 \vec{r}_m + \phi_m)} \quad (4.32)$$

$$E_r = E_{0,r} e^{i(2\pi f_1 t + \vec{k}_1 \vec{r}_r + \phi_r)} \quad (4.33)$$

$$E_{het1} = E_{0,het1} e^{i(2\pi f_2 t + \vec{k}_2 \vec{r}_{het1} + \phi_{het1})} \quad (4.34)$$

$$E_{het2} = E_{0,het2} e^{i(2\pi f_2 t + \vec{k}_2 \vec{r}_{het2} + \phi_{het2})} . \quad (4.35)$$

where ϕ_m , ϕ_r , ϕ_{het1} , and ϕ_{het2} are the initial phases of the four electric fields with $\phi_m = \phi_r$ and $\phi_{het1} = \phi_{het2}$.

The intensity at the reference photodiode is given by

$$\begin{aligned} I_r &= \epsilon_0 c \langle E^2 \rangle \\ &= \frac{1}{2} \epsilon_0 c [E_{0,r}^2 + E_{0,het2}^2 + 2E_{0,r}E_{0,het2} \\ &\quad \cdot \cos(2\pi|f_1 - f_2|t + 2\pi(\frac{r_{het2}}{\lambda_2} - \frac{r_r}{\lambda_1}) - (\phi_{het2} - \phi_r))] , \end{aligned} \quad (4.36)$$

the intensity at the measurement photodiode by

$$\begin{aligned} I_m &= \epsilon_0 c \langle E^2 \rangle \\ &= \frac{1}{2} \epsilon_0 c [E_{0,m}^2 + E_{0,het1}^2 + 2E_{0,m}E_{0,het1} \\ &\quad \cdot \cos(2\pi|f_1 - f_2|t + 2\pi(\frac{r_{het1}}{\lambda_2} - \frac{r_m}{\lambda_1}) - (\phi_{het1} - \phi_m))] . \end{aligned} \quad (4.37)$$

Bandpass filtering at the heterodyne frequency results in

$$\begin{aligned} I_r &= \epsilon_0 c E_{0,r} E_{0,het2} \\ &\quad \cdot \cos(2\pi|f_1 - f_2|t + 2\pi(\frac{r_{het2}}{\lambda_2} - \frac{r_r}{\lambda_1}) - (\phi_{het2} - \phi_r)) \end{aligned} \quad (4.38)$$

$$\begin{aligned} I_m &= \epsilon_0 c E_{0,m} E_{0,het1} \\ &\quad \cdot \cos(2\pi|f_1 - f_2|t + 2\pi(\frac{r_{het1}}{\lambda_2} - \frac{r_m}{\lambda_1}) - (\phi_{het1} - \phi_m)) . \end{aligned} \quad (4.39)$$

Both signals are multiplied, and subsequently low-pass filtered:

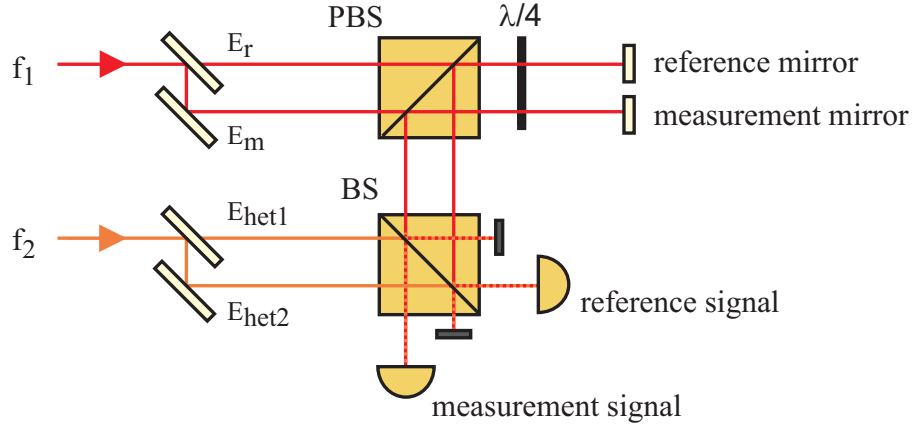


Figure 4.8.: Schematic of the heterodyne interferometer design, which is the basis for our optical readout (BS: beamsplitter; PBS: polarizing beamsplitter).

$$I_{IF} = \frac{1}{2} \varepsilon_0^2 c^2 E_{0,r} E_{0,m} E_{0,het1} E_{0,het2} \cdot \left[\cos \left(\frac{2\pi}{\lambda_1} (r_m - r_r) + \frac{2\pi}{\lambda_2} (r_{het2} - r_{het1}) + (\phi_r - \phi_m) + (\phi_{het1} - \phi_{het2}) \right) \right] \quad (4.40)$$

$$= \frac{1}{2} \varepsilon_0^2 c^2 E_{0,r} E_{0,m} E_{0,het1} E_{0,het2} \cos \left(\frac{2\pi}{\lambda_1} (r_m - r_r) \right) \quad (4.41)$$

$$\propto \cos \left(\frac{2\pi}{\lambda_1} \Delta OPD \right) \quad (4.42)$$

All other summands in equation (4.40) get zero. The optical path length difference is $\Delta OPD = 2n\Delta x$, where Δx is the displacement of the measurement mirror.

In-quadrature measurement of the phase between I_r and I_m results in the two signals

$$S_1 = \frac{1}{2} \varepsilon_0^2 c^2 E_{0,r} E_{0,m} E_{0,het1} E_{0,het2} \cos \left(\frac{4\pi n}{\lambda_1} \Delta x \right) \quad (4.43)$$

$$S_2 = \frac{1}{2} \varepsilon_0^2 c^2 E_{0,r} E_{0,m} E_{0,het1} E_{0,het2} \sin \left(\frac{4\pi n}{\lambda_1} \Delta x \right), \quad (4.44)$$

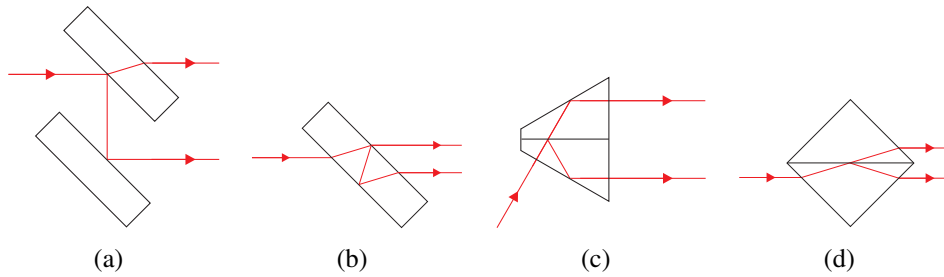


Figure 4.9.: Possible realizations of a beamsplitter generating two parallel output beams.

where the phase is obtained via

$$\phi(t) = \frac{4\pi n}{\lambda_1} \Delta x = \arctan\left(\frac{S_2}{S_1}\right). \quad (4.45)$$

From equation (4.45) it can be seen, that all amplitude factors in equations (4.43) and (4.44) drop out in the phase measurement.

Several possible realizations for the splitting of the two beams with f_1 and f_2 into two parallel output beams are shown in Fig. 4.9. Alternatives (a) and (b) are asymmetric for the two beams: in (a) the upper beam is transmitted by an optical component, the lower one not; in (b) the upper beam is transmitted once by an optical component, the lower beam thrice. Alternatives (c) and (d) are symmetric: (c) represents a Kösters prism where the input and the output beams are orthogonal to the optical surfaces. Therefore, parasitic back reflections (due to imperfect anti-reflection coatings) are reflected into the beam axis and can cause etalon effects. Alternative (d) is also symmetric and prevents back reflections into the beam axis and is therefore esteemed to be the best choice for our interferometer setup.

4.7. Differential Wavefront Sensing

Having an interferometer, alignment information – i.e. information on a tilt of the measurement mirror – can be obtained by using a position sensitive device such as a quadrant photodiode for the measurement signal. The wavefront reflected by the reference mirror is at all times parallel to the detector plane. The wavefront reflected by the measurement mirror is tilted with respect to the detector plane in case of a tilted measurement mirror (cf. Fig. 4.10). This tilt causes a non-uniform interferometer pattern over the cross section of the laser beam. By comparing the phase at two positions over the beam cross section, a change in tilt of the two beams can be measured. In case of a quadrant photodiode (QPD), either the signals of two opposing quadrants or of two opposing halves are compared in phase. This method

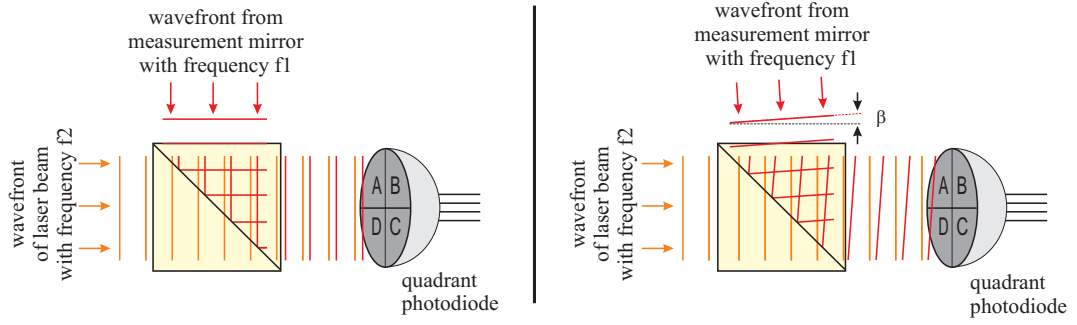


Figure 4.10.: Schematic of Differential Wavefront Sensing. Left: untilted measurement mirror; right: tilted measurement mirror.

is called Differential Wavefront Sensing (DWS) and was initially developed for an automatic alignment system for interferometers by analyzing higher-order Gaussian modes by use of a quadrant photodiode [51, 52, 61].

A laser beam with radius w_0 hitting a quadrant photodiode with radius R is shown in Fig. 4.11. In the ideal case, both beams have the same diameter and are both centered on the QPD. The phase difference at a distance r from the beam center is given by $\phi \approx 2\pi r\beta/\lambda$, where λ is the laser wavelength and $\beta \ll 1$ the tilt of the incoming wavefront from the measurement mirror. The phase measurement is integrated over the area of the photodiode, in case of DWS one single quadrant or half of the photodiode. In an approximation, DWS measures the phases at two locations with a distance of $2r_{ca}$ from the diode's center, where r_{ca} corresponds to the center of area of a single quadrant (or half of the photodiode, respectively³). The measured phase difference in case the phase is compared between two halves is given by:

$$\phi \approx \frac{16w_0}{3\lambda}\beta, \quad (4.46)$$

where w_0 is the radius of the beam with $w_0 < R$ where R is the radius of the QPD. The angle β equals twice the tilt angle of the measurement mirror α : $\beta = 2\alpha$.

A calculation based on two Gaussian beams results in the measured beat note [101]

$$I = 2|E_1 E_2| \int_0^R \int_{-\pi/4}^{\pi/4} r e^{-2r^2/w_0^2} \cos(\beta k r \cos \theta - 2\pi|f_1 - f_2|t) d\theta dr. \quad (4.47)$$

Here the integration is carried out over the surface of one quadrant where R is the

³The distance r_{ca} from the center is given by $4\sqrt{2}w_0/3\pi$ in case of a single quadrant and by $4w_0/3\pi$ in case of summed halves, cf. Fig. 4.11. w_0 corresponds to the beam radius.

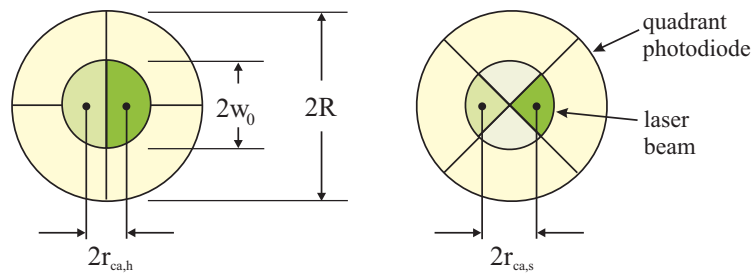


Figure 4.11.: Schematic of a quadrant photodiode (QPD) used for DWS measuring the tilt in the 'left-right' direction. Marked are the centers of area for halves (left) and quarters (right) of the QPD.

radius of the diode, w_0 the beam radius, $k = 2\pi/\lambda$. The integration in θ depends on the orientation of the quadrant diode and the measured signal.

5. Interferometer Setup

As our laboratory setup serves as a demonstrator for a future space qualifiable setup, special attention is put on compactness, robustness and reliability. Also flexibility and a modular, fiber-coupled assembly to ensure simple interfaces are basic design drivers as they ease integration into an optical system setup (as e.g. the optical bench aboard the LISA satellites). For our laboratory experiment we therefore used mechanically highly stable optical mounts with a beam height of only 2 cm. These mounts were originally designed in our group for an experiment realizing a Bose-Einstein Condensate (BEC) under zero-gravity at the drop tower facility in Bremen. In the optics design for the BEC laser system, compactness and robustness are crucial as the whole experiment must fit in a 2 m long drop capsule with an 80 cm diameter and must sustain peak decelerations of up to 50 g at the impact after fall. A compact frequency stabilized laser module developed in the framework of the drop-BEC project is detailed in appendix A.

The optical setup can be divided into two parts: (i) the interferometer board, and (ii) the optics for heterodyne frequency generation. The interferometer board is placed inside a vacuum chamber in order to minimize fluctuations in refraction index due to air turbulence and to provide a better temperature stability, the heterodyne frequency generation is placed outside the vacuum chamber on a standard optical table using standard optical components.

5.1. Heterodyne Frequency Generation

We utilize an NPRO-type (non-planar ring-oscillator, cf. [39]) Nd:YAG laser (by Laser Zentrum Hannover) at a wavelength of 1064 nm providing approximately 200 mW of output power. Part of it is split by a non-polarizing beamsplitter and each beam is shifted in frequency by an acousto-optic modulator (AOM; Crystal Technology, model 3080-125). The beams which are deflected into the first order Bragg diffraction are taken as input beams for the interferometer. In our case, the AOMs are working at RF-frequencies of 80.00 MHz and 80.10 MHz, respectively, resulting in a heterodyne frequency of 100 kHz. The RF-signals are generated by use of two phase-locked function generators (SRS DS345), the signal outputs of which are quadrupled in frequency (Mini Circuits, FD-2) and appropriately filtered and amplified.

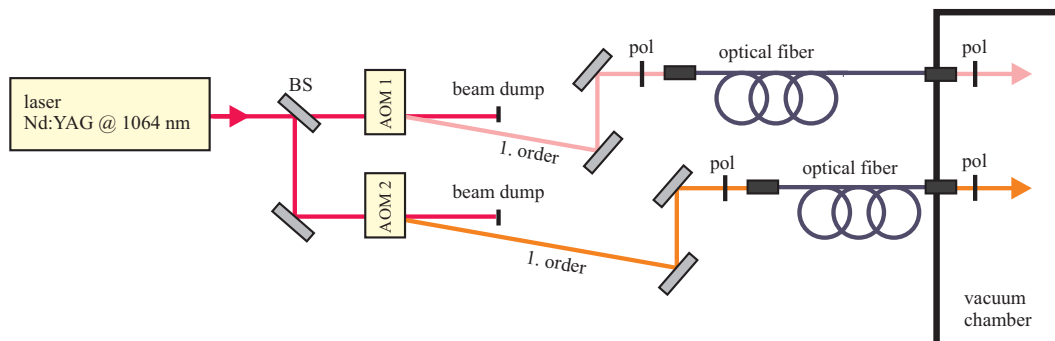


Figure 5.1.: Schematic of the setup for generation of the heterodyne frequencies (AOM: acousto-optic modulator, BS: beamsplitter, pol: polarizer).

A schematic of the optical setup is shown in Fig. 5.1; the electronics setup for driving the AOMs is shown in Fig. 5.2 which is similar for both AOMs. The coupler outputs are both input signals to a double-balanced mixer (ZFM3 by Mini Circuits) in order to generate a 100 kHz signal phase locked to the function generators. This signal is taken for further diagnostic measurements, cf. chapter 5.5.2.

5.2. Interferometer Setup

The schematic of our interferometer setup is shown in Fig. 5.3, a photograph of it in Fig. 5.4. A detailed description of the interferometer setup can be found in [102]. The interferometer is placed on a 4 cm thick aluminum breadboard with a diameter of 23 cm. Cast aluminum (AlMg4.5Mn) was chosen as material because of high thermal stability and absence of internal stresses which could otherwise cause a long-term drift of the material. The laser light coming from the AOMs is fiber coupled and sent to the interferometer board inside the vacuum chamber by use of commercial vacuum feedthroughs (Schäfter und Kirchhoff, polarization maintaining single mode fibers with FC-APC connectors). The collimated beams at the fiber outputs have intensities of ≈ 0.5 mW and a diameter of ≈ 1.4 mm. Polarizers are placed in front and behind the fibers to ensure the proper (and clean) linear polarization. After fiber outcoupling $\approx 5\%$ of each beam intensity is split off by a glass plate to a monitor photodiode (OPT101). On the interferometer board, each beam is again split into two by a beam separator cube ('energy separator cube' by CVI), which provides parallel output beams with a parallelism better than $2'$. The two beams coming from collimator 1 are reflected towards the measurement and reference mirrors by a polarizing beamsplitter (PBS). Passing twice a quarter waveplate ($\lambda/4$), the beams are then transmitted by the PBS. The two beams are superimposed with the beams coming from collimator 2 at a 50:50 non-polarizing beamsplitter

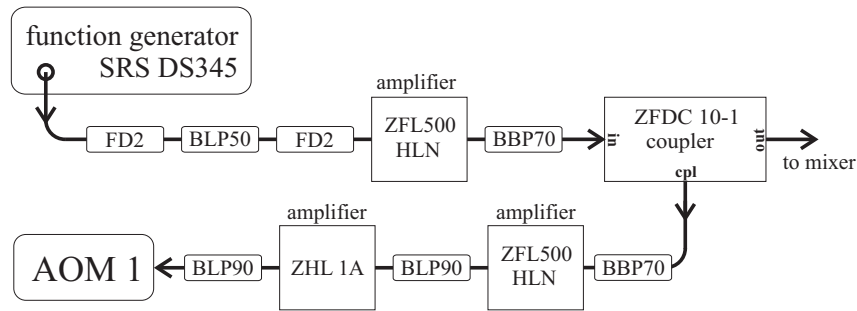


Figure 5.2.: Schematic of the electronics driving the AOMs (BLP: low-pass, BBP: band-pass, FD2: frequency doubler).

(BS). Two silicon quadrant photodiodes¹ provide the measurement signal (QPD1) and the reference signal (QPD2). The signals at QPD1 are also taken for the DWS measurement, providing the tilt measurement. The optical power is $\sim 100 \mu\text{W}$ at the measurement mirror and at the quadrant diodes.

In our first experiments, we used a gold mirror as measurement mirror. It was attached to a piezoelectric tip-tilt actuator (PI S-340 with LVDT sensors and closed-loop servo which removes the hysteresis and drift of the piezoelectric actuator). An additional high voltage piezoelectric actuator (PZT, by Piezomechanik) is placed between the tip-tilt actuator and the gold mirror for translational movement of the measurement mirror. The tip-tilt actuator has a total tilt angle of 2 mrad with a resolution of 500 nrad and a reproducibility of $\pm 1 \mu\text{rad}$ over the whole tilt angle. The PZT by Piezomechanik has no closed-loop option and provides a total displacement of 13 μm by applying -200 V to 1000 V.

5.3. Phase Measurement and Data Processing

We designed and realized an analog in-quadrature phase readout where double-balanced mixers are used as phase detectors, cf. the schematic shown in Fig. 5.5. The signals of the four quadrants are pre-amplified in the vacuum chamber and the single signals as well as their sum are lead through to the outside of the chamber (the electronic circuit diagrams are shown in appendix B). For the translation measurement, the sum signals of both quadrant photodiodes are taken as input for the phasemeter. For DWS the signals of opposing quadrants are taken as input for the phasemeter. The signals are bandpass filtered at the heterodyne frequency of 100 kHz, amplified and split. For the in-quadrature signal generation, one of the output signals of the split reference diode signal is shifted in phase by 90° using

¹Photodiodes provided by Silicon Sensor, type PC20-7, with a diameter of 5.05 mm, a spectral sensitivity of 0.2 A/W at 1064 nm, a capacity of 20 pF and a NEP of $4 \cdot 10^{-14} \text{ W}/\sqrt{\text{Hz}}$.

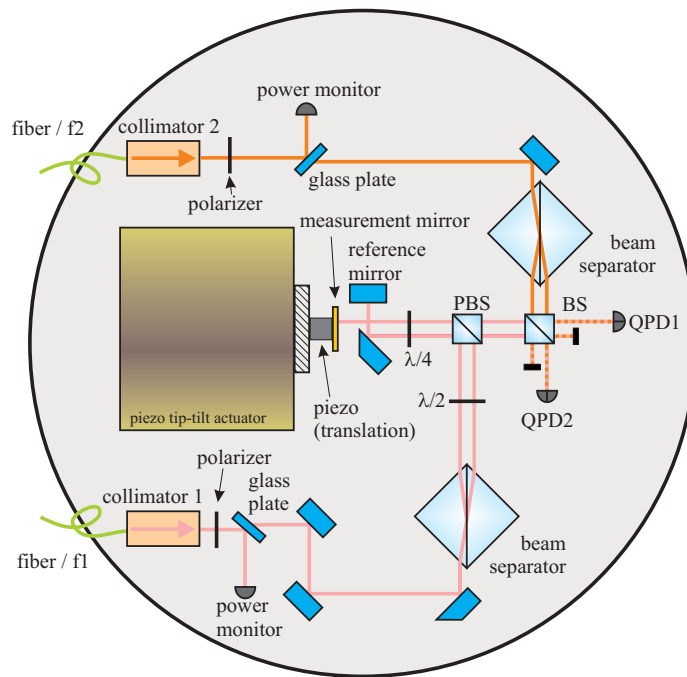


Figure 5.3.: Schematic of our interferometer setup (BS: non-polarizing beamsplitter, PBS: polarizing beamsplitter, PD: photodiode, QPD: quadrant photodiode).

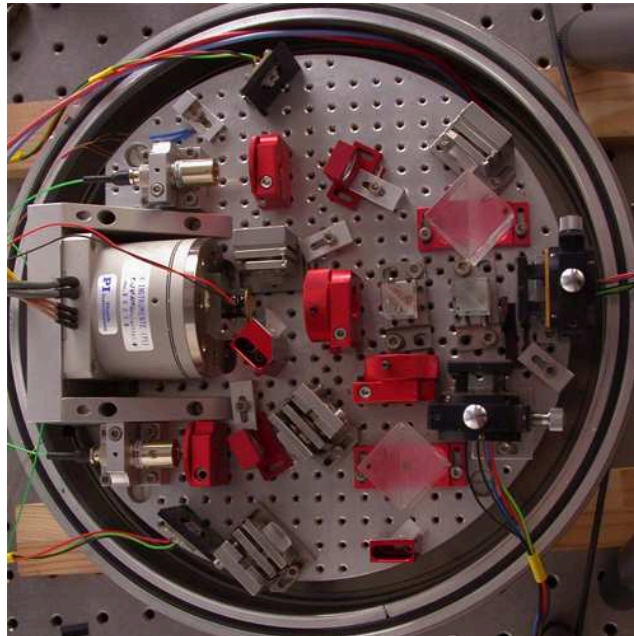


Figure 5.4.: Photograph of our setup. The interferometer is placed on an aluminum board with a diameter of 23 cm.

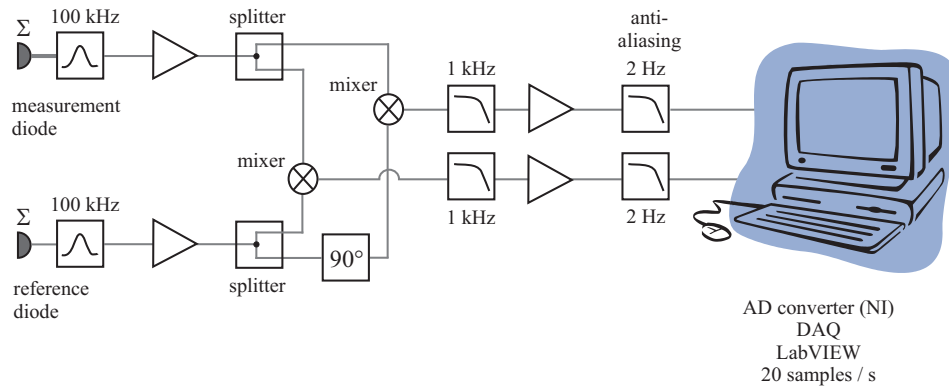


Figure 5.5.: Schematic of the analog in-quadrature phase measurement.

an analog allpass filter. All four signals are input signals to the double-balanced mixers (Mini-Circuits, ZAD-8). The IF output signals of the mixers are low-pass filtered, amplified and anti-alias filtered with a 6th order Bessel filter with a cut-off frequency of 2 Hz (circuit diagram shown in Appendix B.3). They are digitized by a National Instruments 6229 M Series data acquisition board with a 16 bit ADC resolution at a sampling rate of 20 Hz.

5.4. LabView Data Processing

A LabVIEW program provides post-processing of the data and calculates the arctangent as given in equation (4.45). The program also offers a dynamic range not limited to $\lambda/2$ by monitoring π phase jumps in the arctangent. Additional parameters as room temperature, temperature on the interferometer board and voltages at the monitor photodiodes are also recorded. The LabView program in more detail can be found in appendix C.1.

The phase readout for the tilt measurement is similar to the readout for the translation measurement described above. Here, the input signals are the signals from two opposing quadrants of the same QPD. Again, the arctangent is calculated by a LabVIEW program and the measured phase is converted to the tilt angle α of the measurement mirror by use of differential wavefront sensing, cf. chapter 4.7. The conversion factor is obtained via equation (4.47) and results in $\phi_{ij} = 7500\alpha$ (for a quadrant photodiode with a diameter of 5 mm and a beam radius of 0.8 mm)². In our setup, the line of sight of two opposing quadrants of the photodiode is under an angle of 45° to the interferometer baseplate. As we measure the tilt parallel to the baseplate (and perpendicular to it, respectively), the conversion factor is reduced by a factor of $\sqrt{2}$ resulting in $\phi_{eff} = 5300\alpha$.

²Using the approximation given in equation (4.46), a conversion factor $\phi_{ij} = 8200$ is obtained.

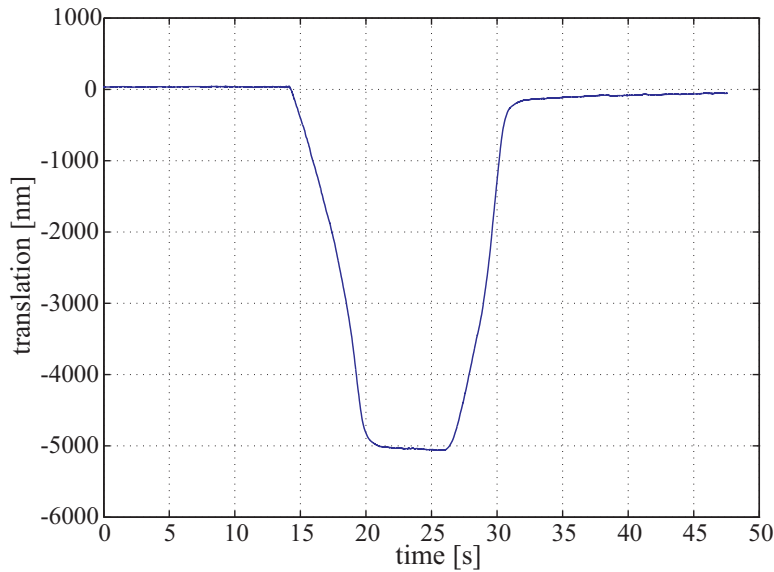


Figure 5.6.: First interferometer check by applying 0 – 625 V to the translation PZT.

5.5. Experimental Results

In our first measurements, we used the setup as described in section 5.2 with a gold mirror glued to a PZT actuator. We first performed a check of the phase measurement verifying its performance. When we saw that the noise and drift of the piezo-electric actuators is limiting the performance, we replaced the measurement and reference mirrors and substituted them by *one* fixed mirror without actuator.

5.5.1. First Check of the Phase Measurement

We applied a voltage 0 V to 625 V to the high-voltage PZT for translational movement which should result in a $5\ \mu\text{m}$ translation of the measurement mirror corresponding to the PZT data sheet. Fig. 5.6 shows the measured translation of the PZT which confirms the estimated value.

By applying a known voltage to the control input of the tip-tilt actuator (sine wave with a frequency of 10 Hz and an amplitude of 200 mV), we also performed a check of the tilt measurement. A conversion factor of $235\ \mu\text{rad}/\text{V}$ was experimentally obtained for the x-axis of the actuator. This results in an applied tilt of the measurement mirror of $47\ \mu\text{rad}$. Using DWS, we measured a tilt of approximately $37\ \mu\text{rad}$. This measurement confirms our phase readout, the difference might be caused by uncertainties in the calculation of the conversion factor, mainly due to a possible slight misalignment of the two overlapping beams.

5.5.2. Measurements with PZT in the Measurement Arm of the Interferometer

A 45 h translation measurement with the setup described above and the corresponding power spectral density³ (PSD) is shown in Fig. 5.7. A zoom into the time series together with the associated interferometer board temperature is shown in Fig. 5.8. The measurement depicts a rather high temperature coefficient of ~ 1000 nm/K and a linear drift of ~ 85.5 nm/day which is not temperature correlated.

We also analyzed the two interferometer signals on the two quadrant photodiodes separately. The phases of the sum signals on the two photodiodes were individually compared to an external 100 kHz reference which was generated by mixing the two (frequency quadrupled) signals of the function generators driving our AOMs. Therefore the outputs of two couplers (ZFDC 10-1 by Mini Circuits) are input to a double-balanced mixer (ZFM 3 by Mini Circuits), cf. Fig. 5.2. The measured signals correspond to an interferometer signal, where the splitting into measurement and reference arm is performed at the beamsplitter before the AOMs. Consequently, both interferometer signals include differential changes in optical pathlength caused by the AOMs and the fibers. A translation measurement is shown in Fig. 5.9. This measurement shows large drifts (~ 14 μm over 8 h) and a short term noise of ~ 600 nm which are both common-mode to both interferometer and mainly caused by the optical fibers where a change in ambient temperature induces changes in optical pathlength. The difference of the two individual interferometer signals should result in the differential interferometer signal. Fig. 5.10 shows the differential interferometer signal in comparison with the difference of the two individual interferometers. The latter one has fluctuations 6 times larger than the differential interferometer signal which also are not correlated.

By tilting the gold mirror, i.e. actuating the tip-tilt PZT actuator, the influence of a tilt of the measurement mirror to the translation signal was measured. A factor of 1.6 nm/ μrad for the x-direction (where the beam stays parallel to the baseplate) and 1 nm/ μrad for the y-direction was obtained. This correlation is most likely caused by a laser beam not hitting the mirror in its center of rotation. Our measurement corresponds to a 1.6 mm displacement in x-direction and a 1 mm displacement in y-direction.

³For the calculation of the power spectral density, cf. Appendix D. In the LISA context it is common, to refer to the spectral density given in $1/\sqrt{\text{Hz}}$ as PSD. Formally, this is a linear spectral density (also amplitude spectral density, ASD, i. e. $\text{PSD}^{1/2}$).

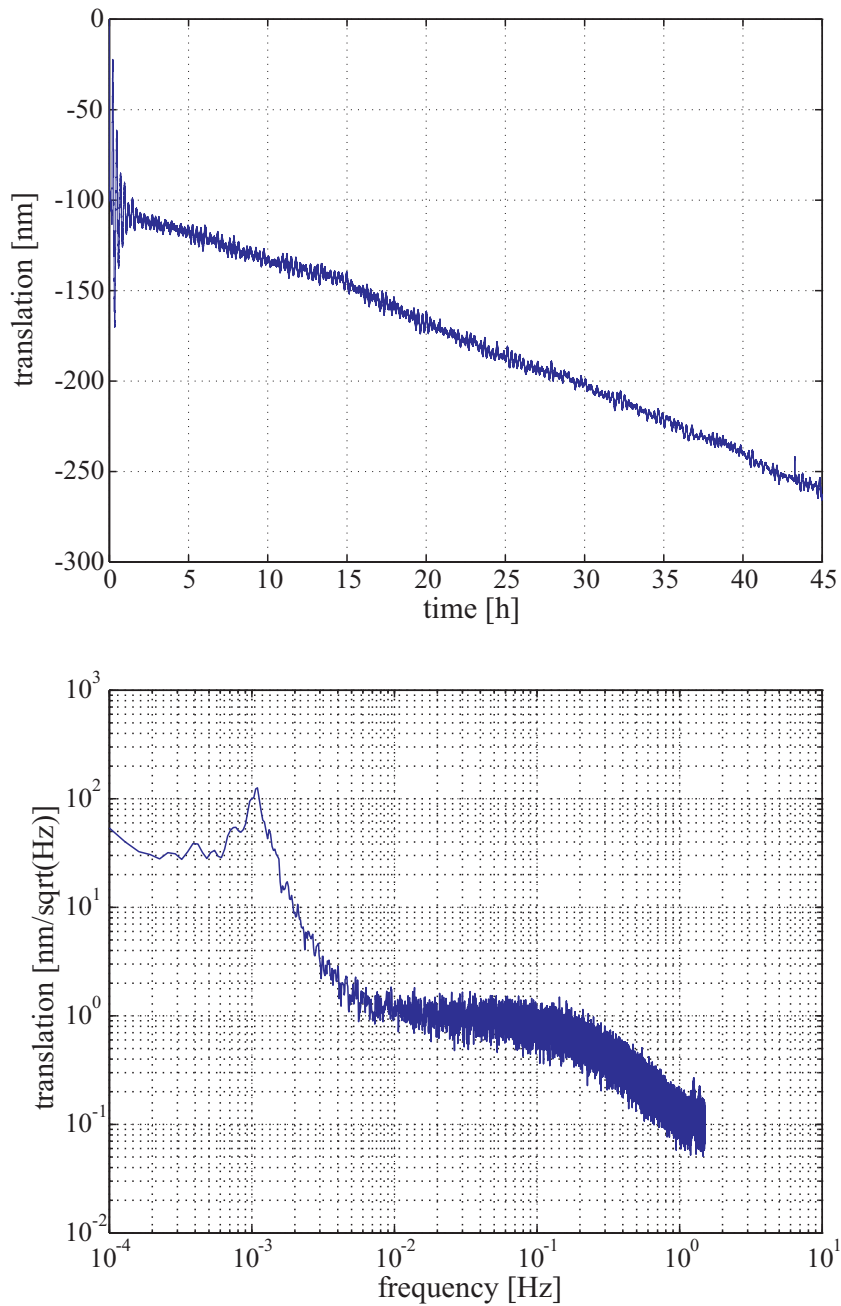


Figure 5.7.: Translation measurement with PZT in the measurement arm of the interferometer. The upper curve shows the measured translation signal, the lower curve shows the calculated PSD (the first 700 s of the measurement showing the transient response of the temperature stabilization servo loop were omitted for PSD calculation).

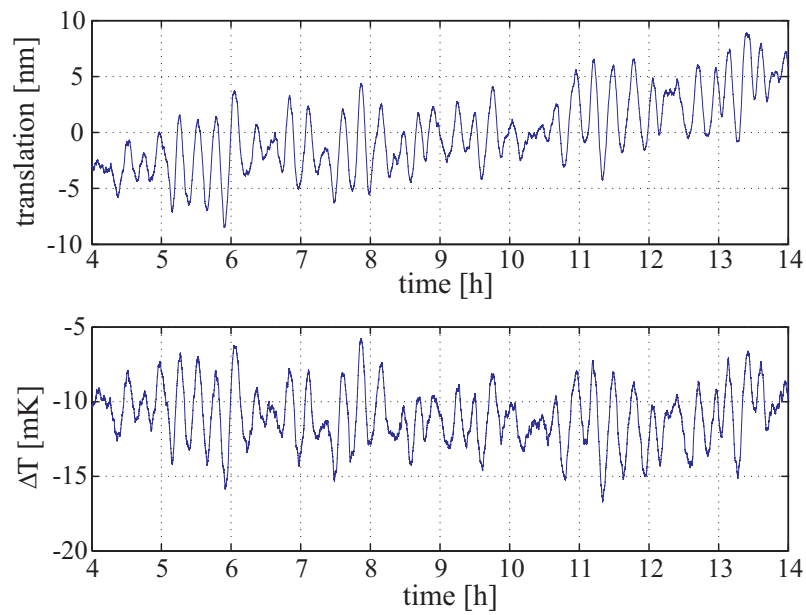


Figure 5.8.: The upper curve shows the measured translation signal, the lower curve shows the temperature of the interferometer board.

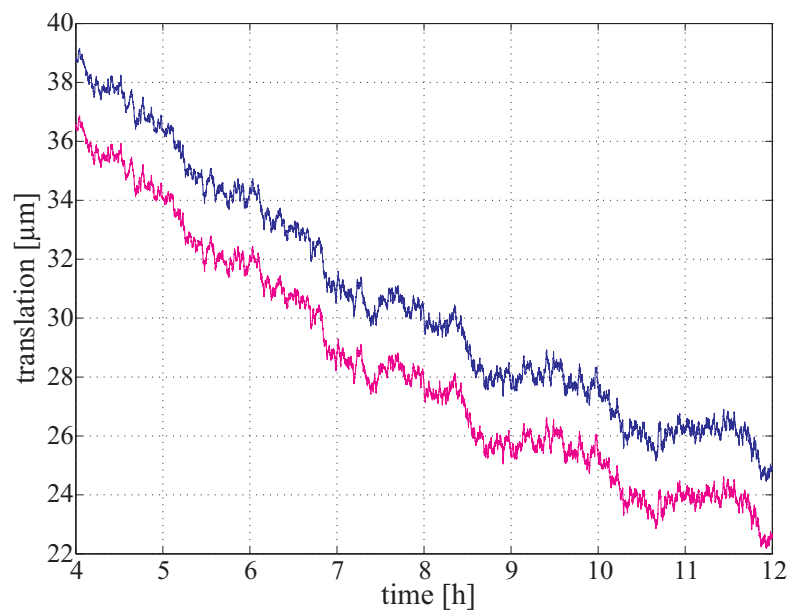


Figure 5.9.: The two interferometer signals of the measurement and reference photodiode.

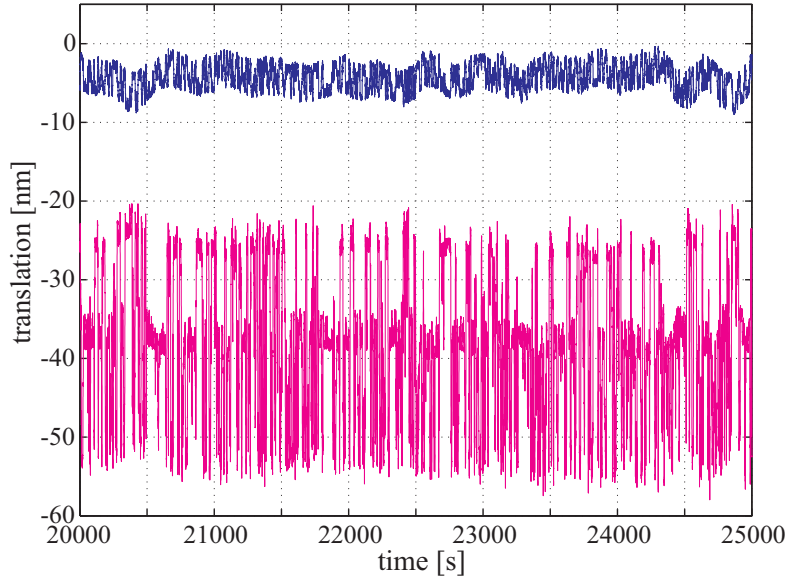


Figure 5.10.: Upper curve: translation signal of the differential interferometer; lower curve: difference of the two individual interferometers, cf. text.

5.5.3. Measurements with PZT in Reference and Measurement Arm

The temperature coefficient was mainly caused by the PZT and was reduced in a setup where both — reference and measurement beam — were reflected by the gold mirror attached to the PZT. Drifts in the PZT then are common mode to both interferometer arms. The drift was allocated to creep in the PZT material and in the glue between PZT and mirror. A translation measurement where reference and measurement beam are reflected by the gold mirror mounted to the PZT is shown in Fig. 5.11. The temperature coefficient is ~ 25 nm/K and the (not temperature correlated) drift ~ 23.3 nm/day.

The measurements of the translation signal when modulating the intensity of the light with frequency f_1 (and f_2 , respectively) are shown in Fig. 5.12 and Fig. 5.13. The measured translation and the corresponding voltage at the monitor photodiodes directly behind the fiber outcoupling on the interferometer board (cf. ‘power monitor’ in Fig. 5.3) are given. Consequently, in order to achieve 10 pm stability in translation measurement, the intensity must be stable to approximately 0.01%.

We also performed a measurement under vacuum condition ($p \leq 7 \cdot 10^{-4}$ mbar) by use of an AEG membrane forepump in combination with an oil-free turbopump

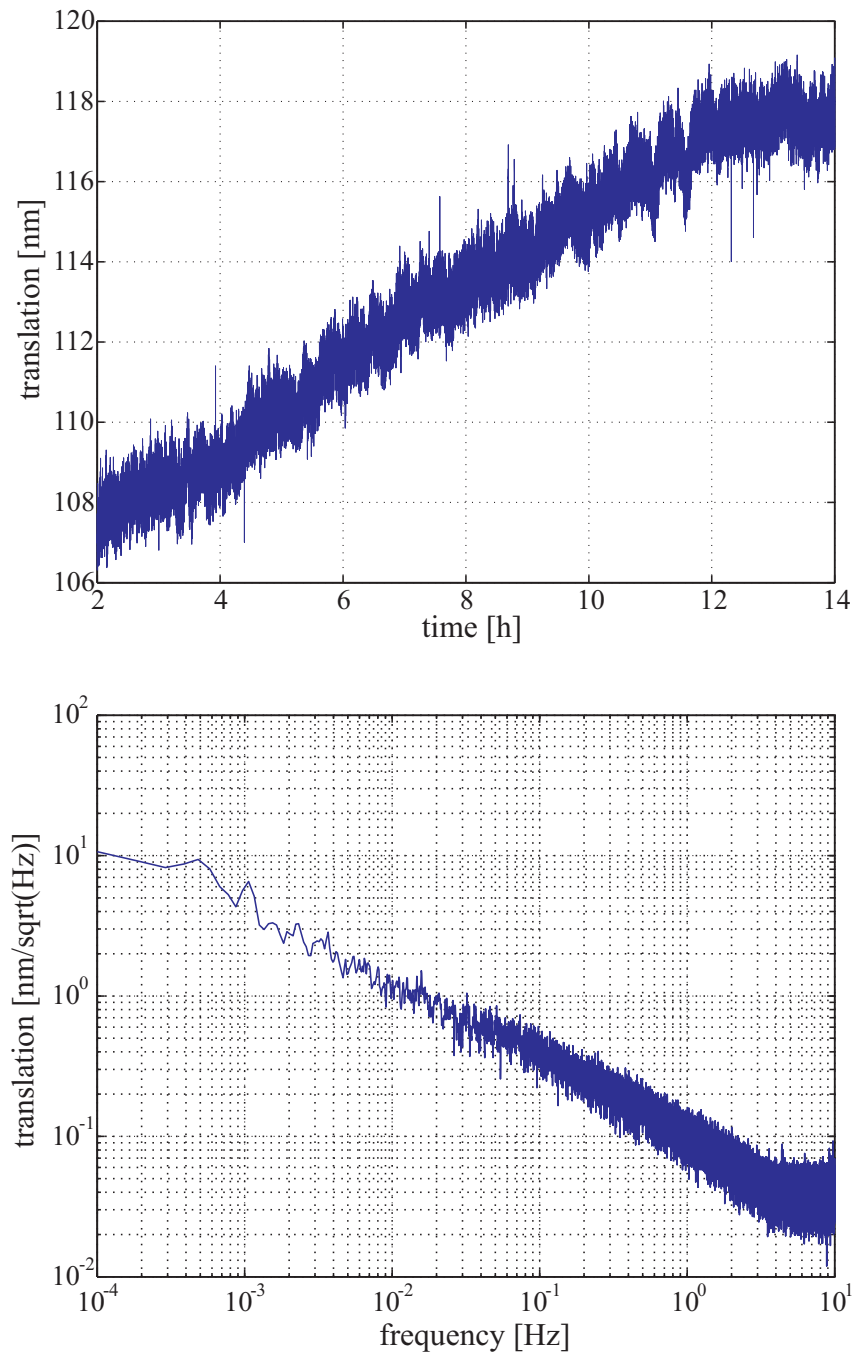


Figure 5.11.: Translation measurement where measurement and reference beam are both reflected by the gold mirror mounted to the PZT. The upper curve shows the measured translation signal, the lower curve shows the calculated PSD.

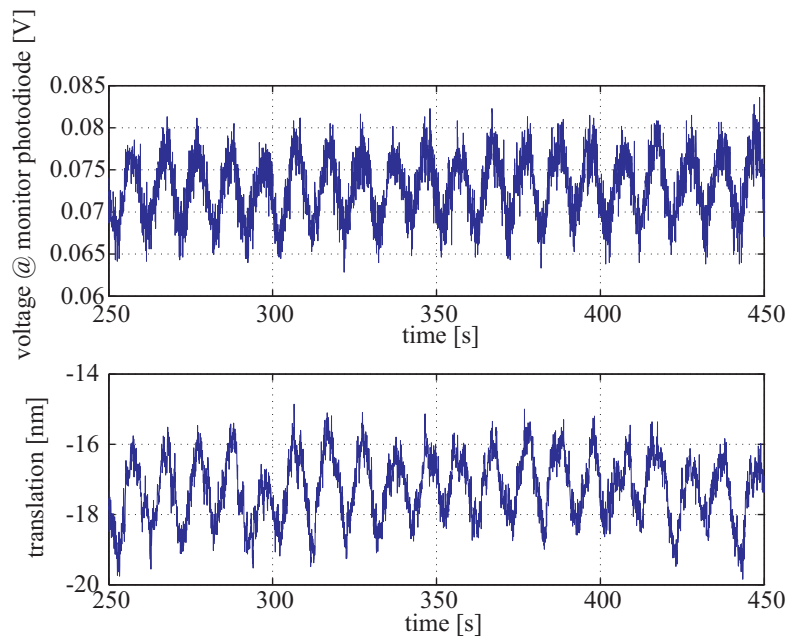


Figure 5.12.: Influence of intensity variations to the translation signal. (The RF-amplitude of AOM 1 was modulated.)

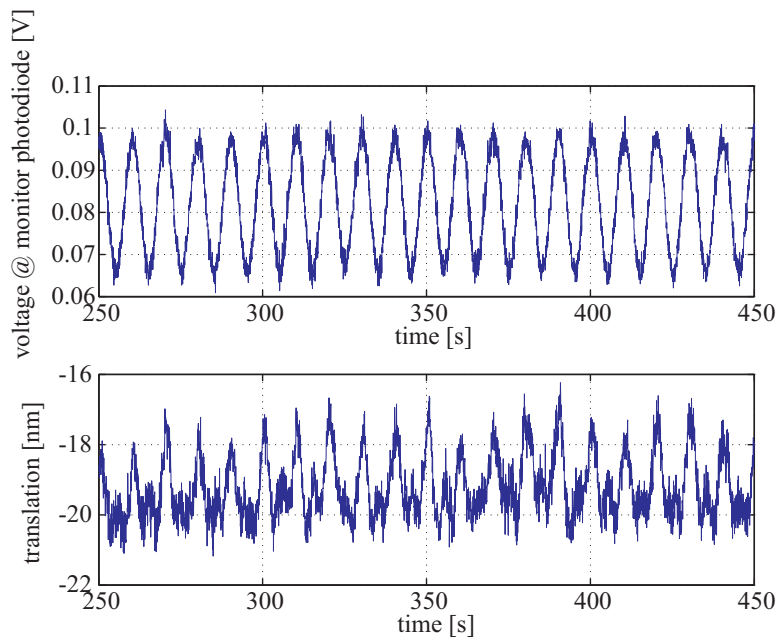


Figure 5.13.: Influence of intensity variations to the translation signal. (The RF-amplitude of AOM 2 was modulated.)

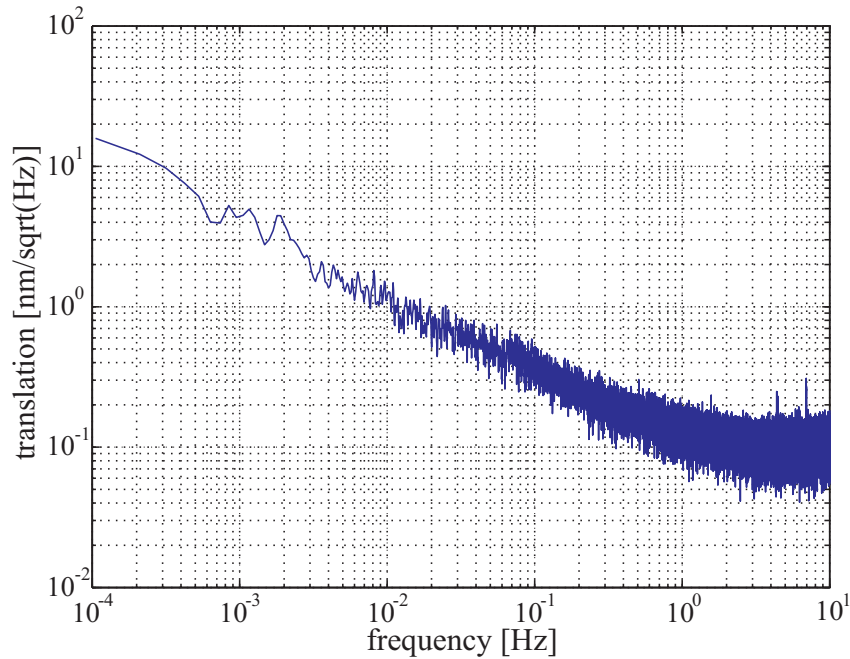


Figure 5.14.: PSD of a measurement under vacuum condition. Measurement and reference beam are both reflected by the gold mirror attached to the PZT.

(TurboVac 151 by Leybold Vacuum). The power spectral density of a 14 h translation measurement is shown in Fig. 5.14. The measurement result is approximately identical to the measurement without vacuum for frequencies below 1 Hz, i.e. in the relevant LISA measurement band. At higher frequencies the noise floor is higher in case of vacuum, probably mainly caused by vibrations induced to the interferometer board by the pumping system.

To test the analog detection part of the phasemeter, we also performed measurements where the signals from both photodiodes were directly digitized. The phase measurement (i.e. mixing and filtering) was carried out post-processed by a Matlab program. There was no observable difference of the resulting PSD compared to the one obtained by use of the analog phasemeter.

5.5.4. Measurements without PZT in the Setup

To determine the translation and tilt noise floor of our metrology system, we replaced the PZT actuator by a fixed mirror which reflected reference and measure-

ment beam⁴. We measured a corresponding temperature coefficient of 40 nm/K. The measured translation signal and its corresponding power spectral density are shown in Fig. 5.15. The measurement was done with closed chamber but at atmospheric pressure. We measured a translation noise $< 80 \text{ pm}/\sqrt{\text{Hz}}$ for frequencies above 10^{-1} Hz and $< 1 \text{ nm}/\sqrt{\text{Hz}}$ for frequencies above 10^{-3} Hz . The PSD of the measured temperature in the chamber was converted to translation noise by the temperature coefficient of $\sim 40 \text{ nm/K}$ and is shown as lower curve in the PSD in Fig. 5.15. Hence, we believe our measurement is limited by temperature variations in the chamber for frequencies below $\sim 3 \cdot 10^{-3} \text{ Hz}$.

The PSD of the measured tilt noise is shown in Fig. 5.16. The noise is $< 70 \text{ nrad}/\sqrt{\text{Hz}}$ for frequencies above 10^{-1} Hz and $< 2 \text{ } \mu\text{rad}/\sqrt{\text{Hz}}$ for frequencies above 10^{-3} Hz .

5.6. Noise Analysis and Identified Limitations

The measured noise spectra show several characteristics, cf. Fig. 5.15 and Fig. 5.16:

- A white noise floor at $\approx 6 \text{ pm}$ ($\approx 5 \text{ nrad}$, respectively) for frequencies above 1 Hz, and
- a noise increase towards lower frequencies. The frequency dependency is not really clear, at intermediate frequencies (between 10^{-2} to 1 Hz in translation measurement and between $\sim 4 \cdot 10^{-1}$ to 1 Hz in tilt measurement) the increase is $\propto 1/f^2$ in power (random walk) and subsequently at lower frequencies nearly $\propto 1/f$ in power (Flicker noise).

The noise levels can have a multitude of origins, some of them are analyzed in the following.

Thermal and acoustic effects: As stated before, for frequencies below 10^{-3} Hz we might be limited by the temperature stability of the optical setup in the vacuum chamber, i.e. differential thermal expansion of the interferometer arms. In the frequency range $3 \cdot 10^{-3} \text{ Hz}$ to 1 Hz, we might be limited by thermal and acoustic noise in the optical fibers and AOMs which cause changes in the intensity of the laser beams after fiber outcoupling. The dependency of the translation measurement on laser intensity was shown in the experiment. Changes in intensity can e.g. be caused by a rotation of the light polarization in the optical fibers (in combination with the

⁴The PZT introduces additional noise sources due to a temperature dependency of the actuator's position; creep of the PZT material, glue and mechanics material; variations in the supply voltage δU . The PZT tilt noise (rms) according to the datasheet is $0.5 \text{ } \mu\text{rad}$ resulting in a translation noise of 2.5 nm.

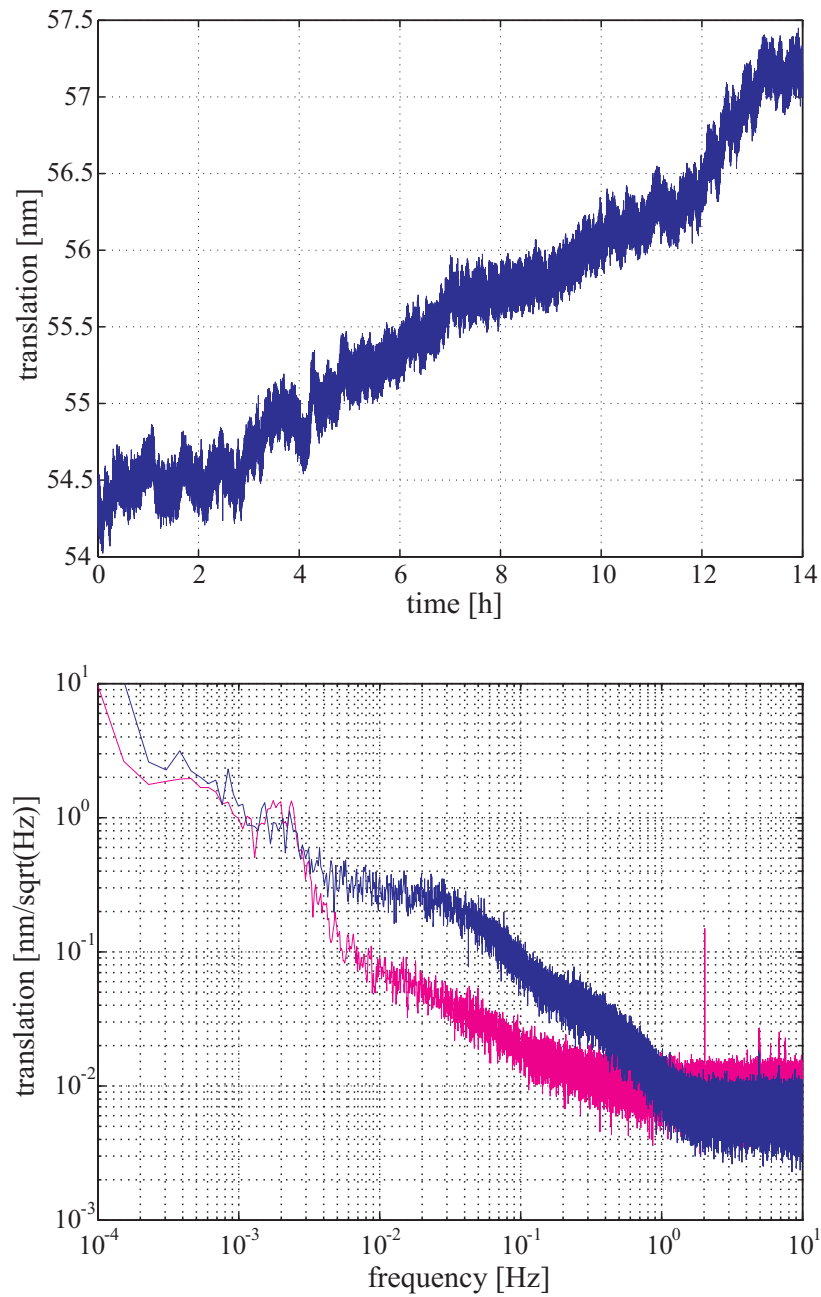


Figure 5.15.: Translation measurement where measurement and reference beam are both reflected by the same fixed mirror. Upper curve: measured translation signal; lower curve: calculated PSD. The upper curve shows the PSD of the translation measurement, the lower curve the PSD of the temperature measured in the vacuum chamber and converted to a resulting translation.

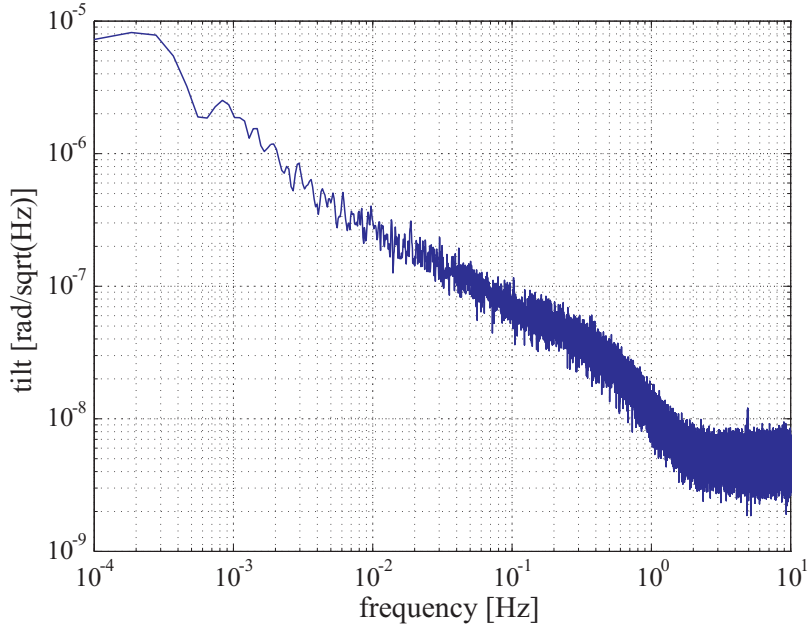


Figure 5.16.: PSD of the tilt measurement. Measurement and reference beam are reflected by the same fixed mirror.

polarizer after fiber outcoupling) and by a slight change in optical alignment of the fiber coupling optics.

Digitizing noise: The noise level of about $10^{-2} \text{ nm}/\sqrt{\text{Hz}}$ for frequencies $> 1 \text{ Hz}$ is caused by amplitude quantization noise of the 16 bit A/D-converter. Input signals with $\pm 5 \text{ V}$ amplitudes transformed to phase noise in the arctangent calculation results in a $\sim 4 \text{ pm}$ noise level. The signal amplitudes were varying for the different measurements, resulting in slightly different noise levels.

Shot noise: The shot noise limited translation measurement sensitivity is given by [57]

$$\Delta l \approx \frac{1}{\pi} \left(\frac{hc\lambda}{2\eta P} \right)^{1/2}, \quad (5.1)$$

with P the laser power, c the speed of light, h the Planck constant, λ the laser wavelength, and η the quantum efficiency of the detector. In our case ($P = 100 \mu\text{W}$, $\lambda = 1064 \text{ nm}$ and $\eta = 0.5$) this results in a noise level of $\approx 1.4 \cdot 10^{-14} \text{ m}$.

Laser frequency noise: Laser frequency noise only cancels in an interferometer with exactly equal path lengths. The phase difference for an interferometer with a

difference in armlengths x is given by equation (4.15) and hence

$$\delta\phi = \frac{4\pi}{c} (x\delta v + v\delta x) = \frac{4\pi vx}{c} \left(\frac{\delta v}{v} + \frac{\delta x}{x} \right). \quad (5.2)$$

$\delta\phi$ is a phase fluctuation caused either by a change in armlength δx or by a change in the laser frequency δv . For a given frequency stability $\tilde{\delta v}/v$ of the laser, the smallest change in displacement which can be measured is given by

$$\tilde{\delta x} = \Delta x \frac{\tilde{\delta v}}{v}. \quad (5.3)$$

In our experimental setup, 1 mm is a realistic difference in armlength. For 1 pm sensitivity this results in a required frequency stability $\delta v/v \approx 10^{-9}$ of the laser source. The frequency stability of an NPRO Nd:YAG laser is in this order of magnitude at 1 Hz but with decreasing stability towards lower frequencies. A frequency stabilization of the laser source might be necessary.

Intensity noise: It was seen in the measurement, that variations in intensity have a rather high influence on the measured translation. The measured coefficient is 1 nm change in translation per 1% variation in intensity.

Electronic noise: A possible limitation in the medium frequency range (10^{-3} to 1 Hz) is electronic noise, including drifts of the anti-aliasing filters. This noise source is not yet analyzed in detail.

Stabilization servo loops: In our experiments, we also realized, that an intensity stabilization is necessary as well as an OPD-stabilization of the two single interferometers. This phaselock of the heterodyne frequency after fiber-outcoupling in the vacuum chamber was also analyzed by the Albert-Einstein-Institute (Hannover) in the context of the LTP engineering model [103, 63, 104] and considered as crucial for obtaining pm interferometer sensitivity.

Resume

For improved performance and better noise analysis, we decided to set up a newly designed interferometer with the following changes and enhancements:

- implementation of an intensity stabilization after fiber-outcoupling
- implementation of a heterodyne frequency phaselock after fiber-outcoupling
- realization of a digital phasemeter, directly digitizing the heterodyne signals from the quadrant photodiodes
- use of a lower heterodyne frequency compliant with the bandwidth of the detectors (~ 10 kHz)

- implementation of a frequency stabilization of the Nd:YAG laser source
- include additional mirrors for easier adjustment
- improve vacuum system and reduce induced vibrations
- improve quadrant diode detector electronics

As our vacuum chamber does not offer the opportunity to include diagnostic tools in the optical setup, especially no space for the detector for the heterodyne frequency phaselock, we decided to build up a new interferometer board and a new vacuum chamber. The advanced interferometer is subject of the following chapter.

6. Advanced Setup

Our first setup showed limitations with respect to the space available on the interferometer board e.g. for diagnostics and additional detectors. Also, the vacuum system caused problems, mainly due to induced vibrations. We therefore decided to realize a new setup on a larger aluminum board in a newly designed vacuum chamber. This new setup also includes a new digital phasemeter based on an FPGA computer board which is capable in simultaneously digitizing the heterodyne signals for translation and tilt measurement.

6.1. Frequency Generation

The measurements with our new setup were carried out utilizing different NPRO-type Nd:YAG lasers at a wavelength of 1064 nm. At the beginning, we used a Nd:YAG laser by Laser Zentrum Hannover which was replaced by a new one (laser ‘Prometheus’ by InnoLight GmbH) during the project. The latter one provides 1 W output power at 1064 nm and ~ 50 mW output power single-pass frequency doubled at 532 nm. Also, it is equipped with an intensity stabilization (‘noise eater’). This laser eases the realization of an active laser frequency stabilization to a molecular absorption line in Iodine. Later this laser was replaced by an InnoLight ‘Mephisto’ with 500 mW output power at 1064 nm.

The optics for frequency generation is similar to our first setup. Additionally, intensity stabilization and heterodyne frequency phaselock after fiber outcoupling are implemented, cf. the schematic shown in Fig. 6.1 and the photograph in Fig. 6.2. A schematic of the electronics used for driving the AOMs, intensity stabilization and frequency phaselock is shown in Fig. 6.3. Two phase locked direct digital synthesizers (DDS, by Novatech, Model 408A) generate in-quadrature signals (sine and cosine) at frequencies 79.99 MHz and 80.00 MHz. The DDS cosine output signals are appropriately filtered and amplified and provide the AOM drive signals. A double-balanced mixer is included before the power amplifier as actuator for the intensity stabilization, cf. chapter 6.3. Compared to our first setup, we have chosen a lower heterodyne frequency of 10 kHz as this corresponds to the bandwidth of our detectors. As we implement a digital phasemeter, we are not restricted to available analog electronics (as e.g. amplifiers provided by Mini Circuits which are only available for frequencies > 100 kHz). The DDS sine output signals are input to

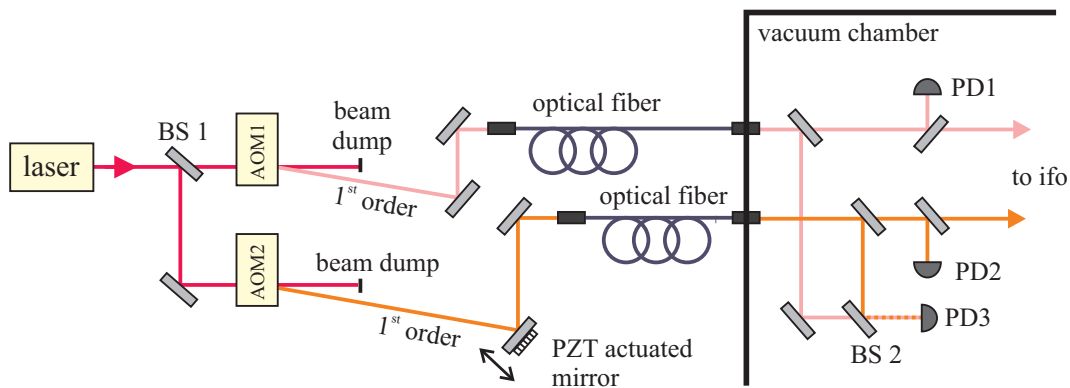


Figure 6.1.: Schematic of the heterodyne frequency generation including the photodiodes used for intensity stabilization (PD1 and PD2) and heterodyne frequency phaselock (PD3). (AOM: acousto-optic modulator; BS: beamsplitter; PD: photodiode).

a double balanced mixer which provides the 10 kHz reference signal for frequency phaselock (cf. chapter 6.4).

6.2. Interferometer Setup

A schematic of our interferometer is shown in Fig. 6.4, a photograph of it in Fig. 6.5; it is also detailed in [105, 106]. The interferometer is placed on a 300 mm x 440 mm x 40 mm cast aluminum board guaranteeing low internal stresses, which otherwise might lead to a long term creep of the material.

The two frequencies are provided to the interferometer board by use of commercial fiber vacuum feedthroughs (polarization maintaining single-mode fibers by Schäfter and Kirchhoff). The light intensities at the fiber outputs are ~ 2.5 mW. Both beams are first split at a 6 mm thick wedged glass plate. The reflections at the front surfaces are the input beams for the interferometer with intensities of ~ 200 μ W. The reflections at the back surfaces are sent to photodiodes PD1 and PD2 whose signals are used for intensity stabilization, cf. chapter 6.3. The beams transmitted at the glass plates are superimposed on a third photodiode (PD3) — this signal is used for the heterodyne frequency phaselock, cf. chapter 6.4.

The beams for use in the interferometer are split in two parallel output beams with a parallelism better than $2'$ by use of two beam separator cubes. These cubes guarantee a symmetric optical path of the two beams inside the material. The two beams with frequency f_1 represent measurement and reference beam of the interferometer. At a polarizing beamsplitter (PBS) both beams are reflected towards the measurement and reference mirrors, which in our experiment are realized by one fixed mir-

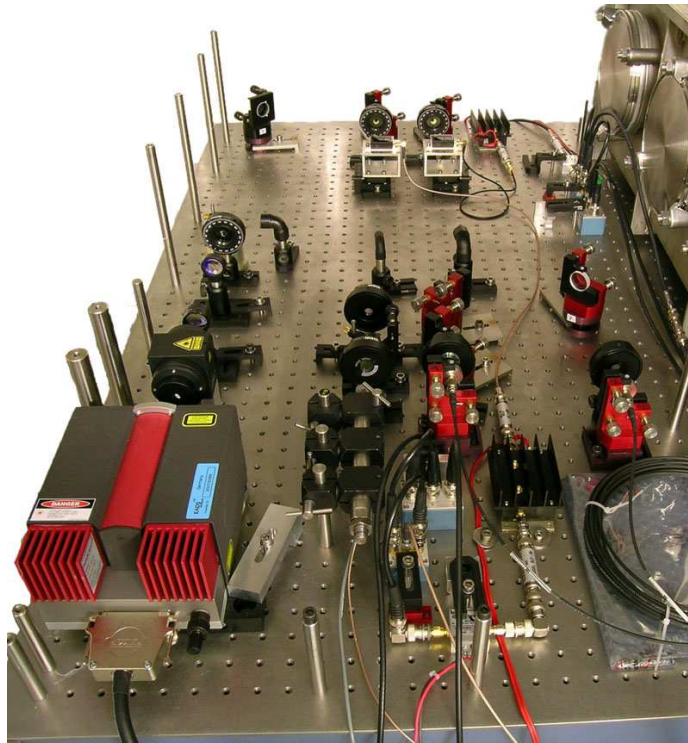


Figure 6.2.: Photograph of the frequency generation setup.

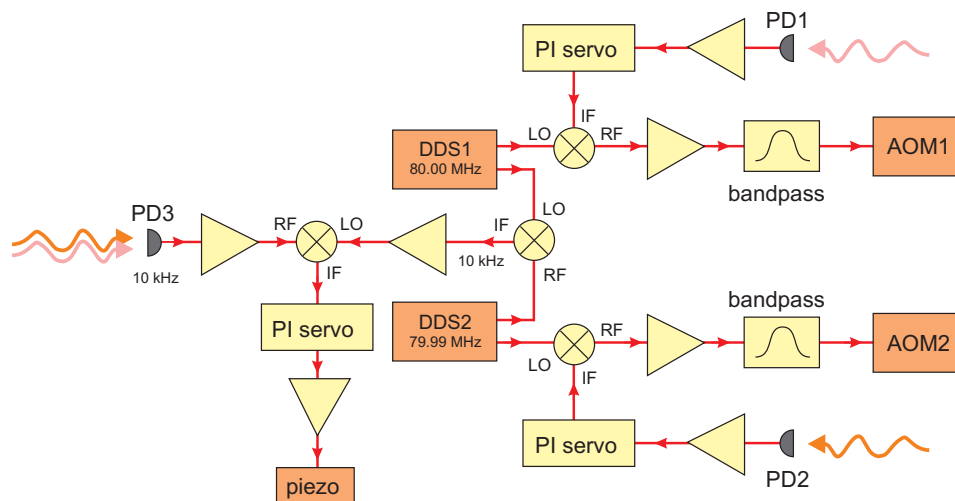


Figure 6.3.: Schematic of the electronics for heterodyne frequency generation and phaselock (DDS: direct digital synthesizer, PD: photodiode, LO: local oscillator; AOM: acousto-optic modulator).

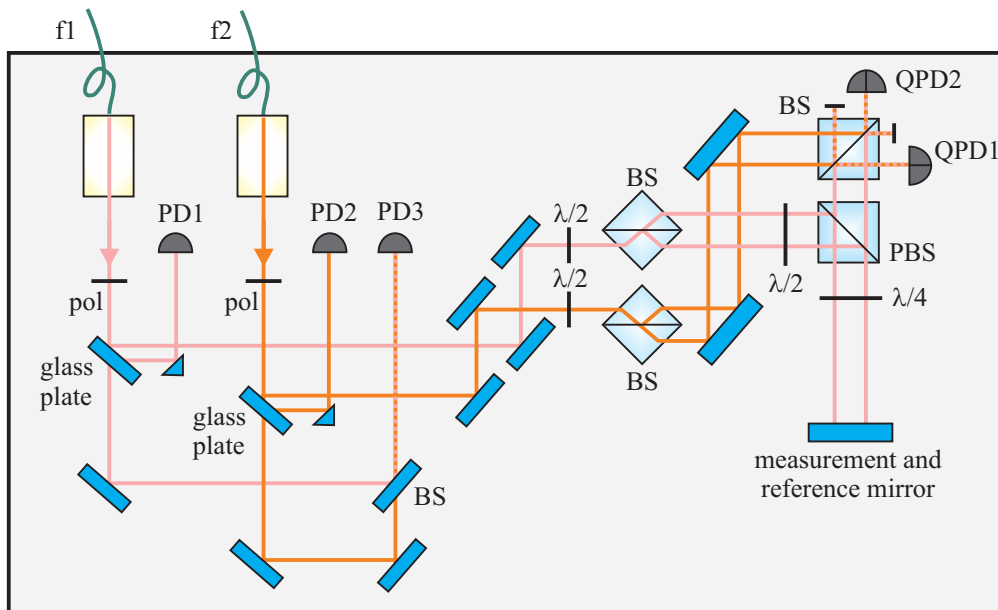


Figure 6.4.: Schematic of our setup (BS: non-polarizing beamsplitter, PBS: polarizing beamsplitter, PD: photodiode, QPD: quadrant photodiode).

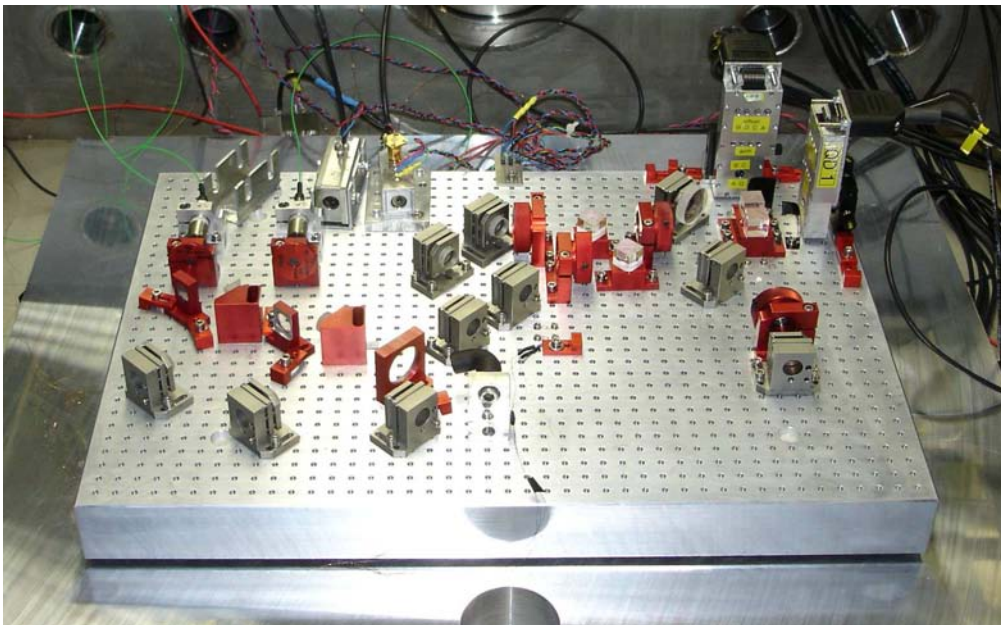


Figure 6.5.: Photograph of our interferometer setup in the vacuum chamber. The optics are placed on a 300 mm x 440 mm x 40 mm cast aluminum board.

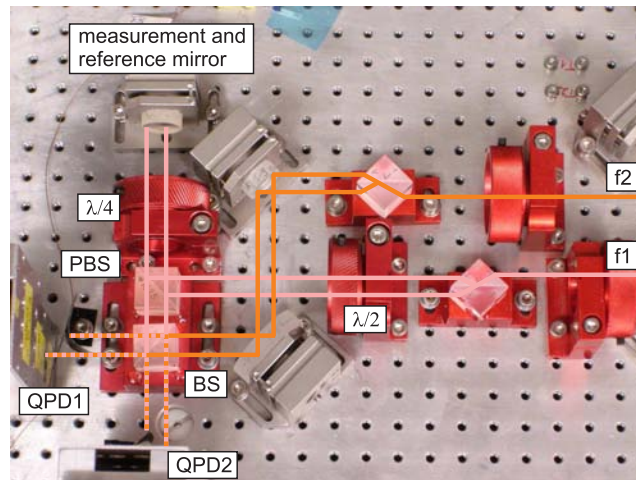


Figure 6.6.: Photograph detail of the interferometer part. The optical beam path is shown schematically.

ror reflecting both beams in order to perform noise measurements. After passing twice a quarter waveplate ($\lambda/4$), the beams are superimposed at a non-polarizing beamsplitter (BS) with the two beams with frequency f_2 . The measurement and the reference signals are both measured by a quadrant photodiode (QPD, by Silicon Sensor), where the sum signals are taken for the translation measurement. The signals of the individual quadrants of QPD1 are taken for the differential wavefront sensing measurement. A detailed photograph of the interferometer part is shown in Fig. 6.6.

6.3. Intensity Stabilization

Part of the laser light after fiber-outcoupling is monitored at two photodiodes (PD1 and PD2 in Fig. 6.1 and Fig. 6.4). Their signals are taken for an intensity stabilization controlling the amplitudes of the RF-signals driving the AOMs. A proportional integral control loop with a bandwidth of ~ 50 kHz provides the feedback signal to the intermediate frequency port of a double-balanced mixer (ZFM-3 by Mini Circuits) placed between the DDS and the AOM. The corresponding schematic is shown in Fig. 6.3.

6.4. Heterodyne Frequency Phaselock

After fiber-outcoupling on the interferometer board, the beams with frequencies f_1 and f_2 are superimposed on a photodiode (PD3 in Fig. 6.1 and Fig. 6.4). This signal

corresponds to an interferometer signal, where the splitting in measurement and reference beams takes place at the beamsplitter in front of the AOMs. Therefore, the photodiode signal contains all differential phase-effects caused by the fibers and the AOMs. These effects are limiting the interferometer performance in the sub-nm level see e.g. [63] and can be minimized by phase locking the heterodyne signal on the photodiode to an externally generated 10 kHz signal. In our experiment, the external 10 kHz signal is obtained by mixing the two signals of the DDS driving the AOMs. The actuation of the feedback loop is carried out by a mirror glued to a piezo-electric actuator in front of one of the fiber couplers. A schematic of the electronics for the phaselock is included in Fig. 6.3. Variations in intensity caused by the heterodyne frequency phaselock due to beam-walk in front of the fiber coupler are removed by the intensity stabilization.

According to [63] and [103] the limitations are caused by second-order sidebands on the light which are caused by nonlinear mixing processes of the AOM driver electronics. The (power-amplified) signal of one AOM is thereby electromagnetically picked-up by the driving electronics of the other AOM. The frequency spectra of the driving signals of the AOMs in our experiment are shown in Fig. 6.7 and Fig. 6.8. The graphs show the driving signal of one AOM, and include two measurements: one where the other AOM driver is on, one where the other AOM driver is off. In case, the other AOM driver is on, sidebands in the signal are expected. We first set the frequencies to 79.99 MHz and 80 MHz – cf. Fig. 6.7 – where large sidebands are visible in the spectra. In a setting where AOM1 is operated at 77.5913 MHz and AOM2 at 77.6013 MHz – cf. Fig. 6.8 – no sidebands are visible. Considering our measurement sensitivity, the carrier to sideband distance is in this case > 60 dB. As given in [103], this distance has to be > 120 dB in order not to have an influence on the interferometer measurement. Most probably sidebands will still be present, hence influencing our measurements. As the DDS reference signal is at 20 MHz, it is assumed, that its quadruplicated frequency has influence on the DDS output frequency spectrum, causing the peak at 80 MHz and the sidebands nearby. These sidebands are also present in the driving signal of AOM1 when AOM2 is off. The later measurements with our interferometer were made with the AOM settings near 77.6 MHz. When looking at the signals of the quadrant photodiodes using a spectrum analyzer, no 10 kHz frequency component can be seen in case only one beam is incident on the detector.

6.5. Frequency Stabilization of the Nd:YAG Laser

The new Prometheus InnoLight laser offers 1 W output power at the fundamental wavelength of 1064 nm and also 50 mW at the second harmonic (532 nm). At this wavelength, molecular Iodine offers several strong absorption lines which can be

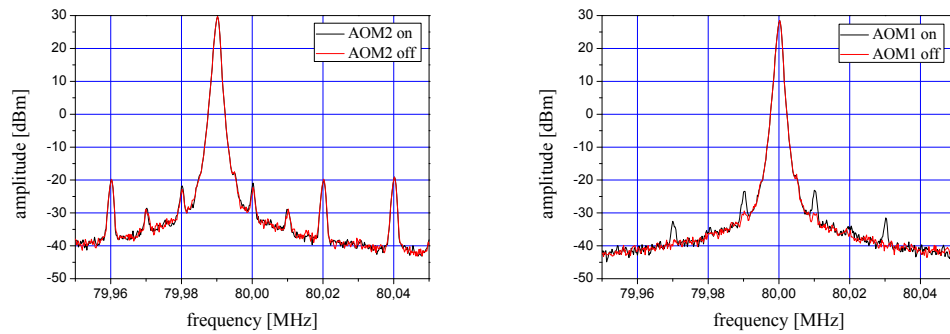


Figure 6.7.: AOM sidebands when AOM1 is operating at 79.9 MHz and AOM2 at 80.0 MHz. Left: Electronic driving signal of AOM1 with and without AOM2 operating; Right: Electronic driving signal of AOM2 with and without AOM1 operating.

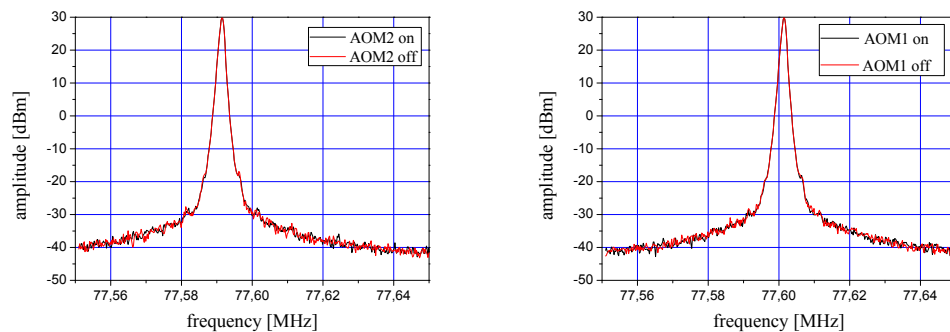


Figure 6.8.: AOM sidebands when AOM1 is operating at 77.5913 MHz and AOM2 at 77.6013 MHz. Left: Electronic driving signal of AOM1 with and without AOM2 operating; Right: Electronic driving signal of AOM2 with and without AOM1 operating.

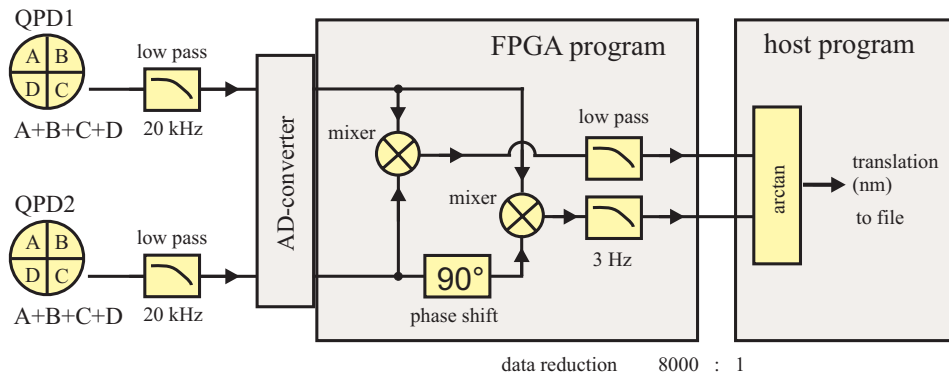


Figure 6.9.: Schematic of the digital phase measurement. The sum signals of the two quadrant photodiodes are taken as input signals for the translation measurement.

used for frequency stabilization of the laser. An existing setup – cf. [107, 108] and appendix E – was again put into operation, realizing modulation transfer spectroscopy for resolving the hyperfine splitting of the Iodine 1110 line.

6.6. Digital Phase Measurement

We implemented a digital phase measurement which is based on a National Instruments Field Programmable Gate Array (FPGA) board. The FPGA is programmed with LabVIEW and offers a simultaneous sampling of up to 8 analog input channels with sampling rates up to 200 kSamples/s. In our measurement, the 10 kHz signals from the quadrant diodes are first amplified inside the vacuum chamber and the individual quadrant signals are sent to an analog electronics outside the vacuum chamber. This electronics generates the sum signal of all four quadrants and the sum of each half of the quadrant diode. All signals are anti-aliasing filtered by use of 6th order Bessel low-pass filters with a cut-off frequency of 20 kHz. The DC components are blocked and the signals are digitized at a sampling frequency of 160 kHz by the onboard 16 bit A/D-converter. For translation measurement, the two sum signals of the quadrant diodes are multiplied and 3 Hz low-pass filtered by a 4th order IIR (infinite impulse response) butterworth filter provided by LabVIEW 8.2. The data is then reduced by a factor of 8000 and transferred to a LabVIEW host program which carries out the phase calculation by the arctan-calculation as given in equation (4.45). The program also offers a dynamic range not limited by $\lambda/2$ by monitoring π phasejumps in the arctangent. A schematic of the phase measurement is shown in Fig. 6.9. The circuit diagrams of the analog electronics can be found in appendix B, the LabVIEW program is detailed in appendix C.2.

The tilt measurement is similar to the translation measurement described above. Here, the signals from the corresponding two halves of the quadrant diode are taken as input signals to the FPGA board. The measured phase relation is converted to a tilt of the measurement mirror by use of the conversion factor $\phi_{ij} = 7500\alpha$ between opposing halves i and j of the quadrant photodiode. The factor is obtained via equation (4.47).

6.7. Vacuum System

The newly designed rectangular vacuum chamber has an internal dimension of 1050 mm x 750 mm x 280 mm giving place to a 900 mm x 600 mm breadboard. It is designed as a general test bed for optical laboratory experiments. In our experiments, the chamber is covered by a 50 mm thick plexiglass plate.

For our measurements, we first placed a 600 mm x 900 mm x 40 mm aluminum board at the bottom of the chamber. It is insulated from the vacuum chamber by POM made spacers. The interferometer board is placed on top of this aluminum board; thermoelectric coolers are situated between them.

The dry pump system consists of a membrane forepump (MVP 055-3 by Pfeiffer Vacuum) in addition with a magnetic levitated turbo pump (TMH-071 YP by Pfeiffer Vacuum). A final pressure of approximately $4 \cdot 10^{-5}$ mbar is achieved.

6.8. Measurements

6.8.1. Test of the Digital Phasemeter

We first tested our optical setup and the digital phasemeter by placing a glass plate in the measurement arm of the interferometer. The glass plate was tilted by approximately 4.2° corresponding to a change in optical pathlength of $\sim 0.95 \mu\text{m}$. Our translation measurement using the interferometer setup is shown in Fig. 6.10 where the glass plate was tilted forth and back several times. Our measurement confirms the estimated value.

6.8.2. Translation Measurement

The measured translation signal and corresponding power spectral density (PSD) of a 60 h measurement is shown in Fig. 6.11. In this measurement, the intensity stabilization and the phaselock were implemented, the temperature stabilization was turned off. The peak near 3 Hz is caused by a missing synchronization of the DDS and the FPGA board and is removed in later measurements.

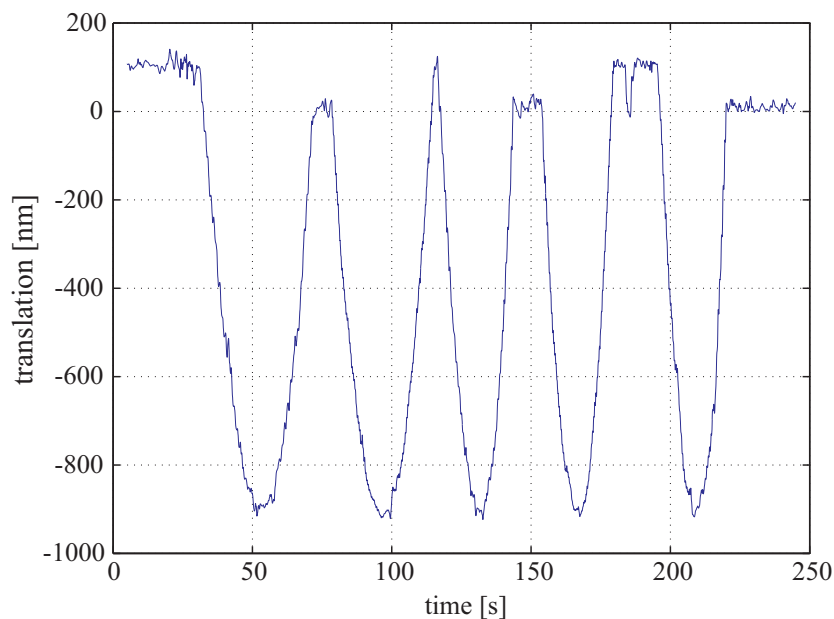


Figure 6.10.: Translation signal while tilting manually a glass plate in the measurement arm of the interferometer.

The different contributions of the several servo loops are shown in Fig. 6.12. Curve 1 was measured without intensity stabilization and phaselock. The noise level is similar to our first setup, cf. the PSD shown in Fig. 5.15, except the peak near $4 \cdot 10^{-3}$ Hz. This peak is caused by the temperature stabilization of the interferometer breadboard which is not yet optimized. The measurement shown in curve 2 includes additional intensity stabilization and a parameter optimized temperature stabilization shifting the servo peak to lower frequencies. Curve 3 corresponds to a measurement with implemented intensity stabilization and phaselock and curve 4 is obtained under similar conditions as curve 3 but with temperature stabilization turned off. It is obvious, that for the LISA low frequency band, a passive temperature stabilization seems to be more effective. The significance of the phaselock in order to reach sub-nm noise levels can clearly be seen, it is also evident in the time series shown in Fig. 6.13. We also performed measurements with an active frequency-stabilization of the Nd:YAG laser source. Frequency noise and drifts should cancel in an ideally symmetric design of the interferometer with same path-lengths in measurement and reference beam. The PSD of two measurements with and without frequency stabilization are shown in Fig. 6.14. Both measurements were carried out on two successive days without other changes in the setup. The measurements show no significant change in the measured noise levels although a slight noise decrease at lower frequencies can be interpreted in case of an active

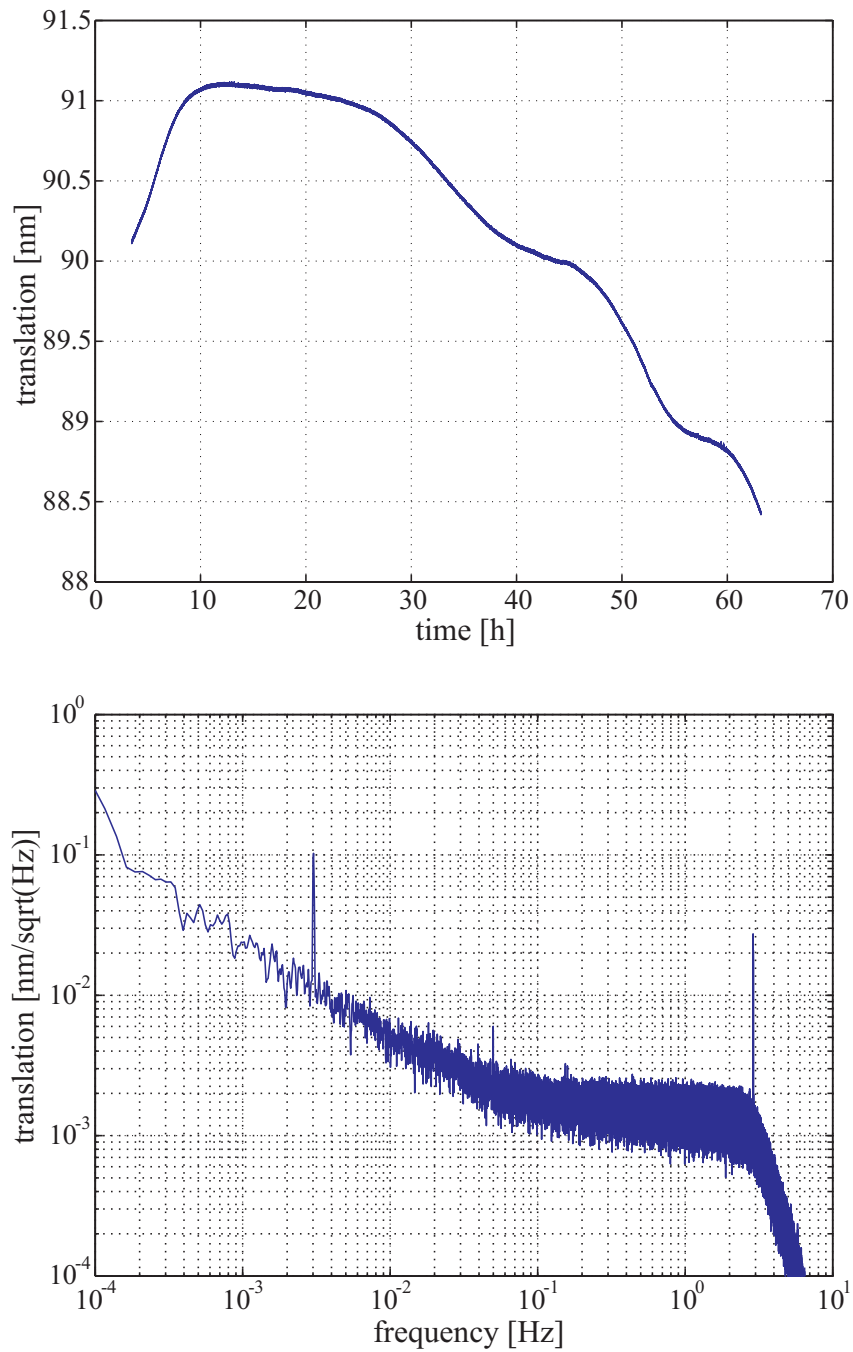


Figure 6.11.: Translation measurement of a 60h measurement. The upper curve shows the measured translation signal, the lower curve shows the calculated PSD.

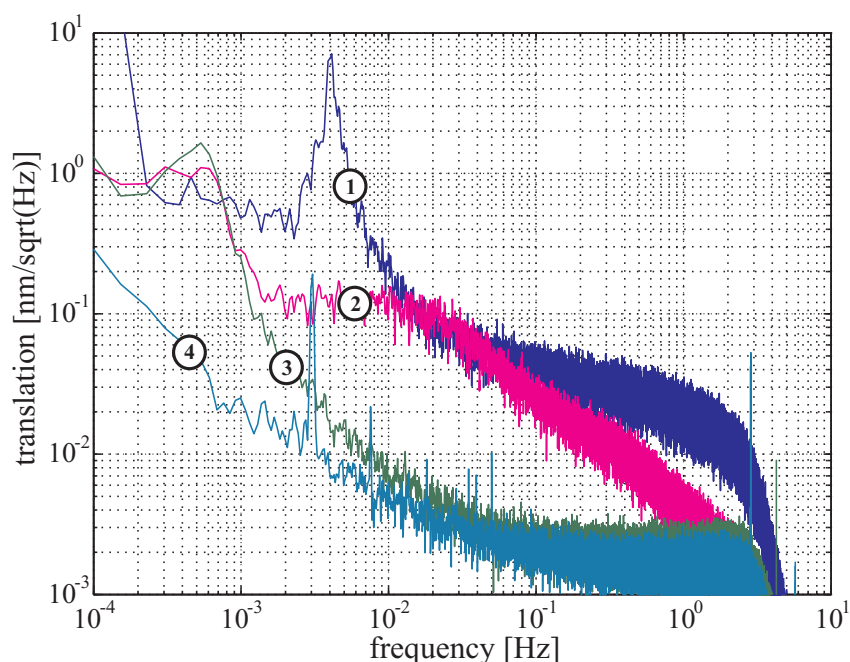


Figure 6.12.: Power spectral density of the translation measurement: 1. without intensity stabilization and phaselock, with temperature stabilization; 2. with additional intensity stabilization and improved temperature stabilization; 3. with additional phaselock; 4. with intensity stabilization and phaselock but without temperature stabilization.

stabilization.

We also performed a comparison between a digital and an analog phase measurement. The corresponding PSDs are shown in Fig. 6.15. The digital and the analog measurement were carried out at the same time. The analog measurement with double-balanced mixers as phase detectors corresponds to the in-quadrature measurement detailed in chapter 5.3. Use of analog electronics increases the (Flicker) noise level by a factor of ~ 5 over the whole LISA frequency range.

By varying the RF amplitude of one of the two AOMs, we measured an effect in the translation measurement. In this measurement, the intensity stabilization loop using the AOM whose intensity is varied is not working, the intensity stabilization loop using the other AOM is working. The measured coefficient is approximately 45 pm per 1% change in intensity. By use of the intensity stabilization, this effect states no limitation in our measurements.

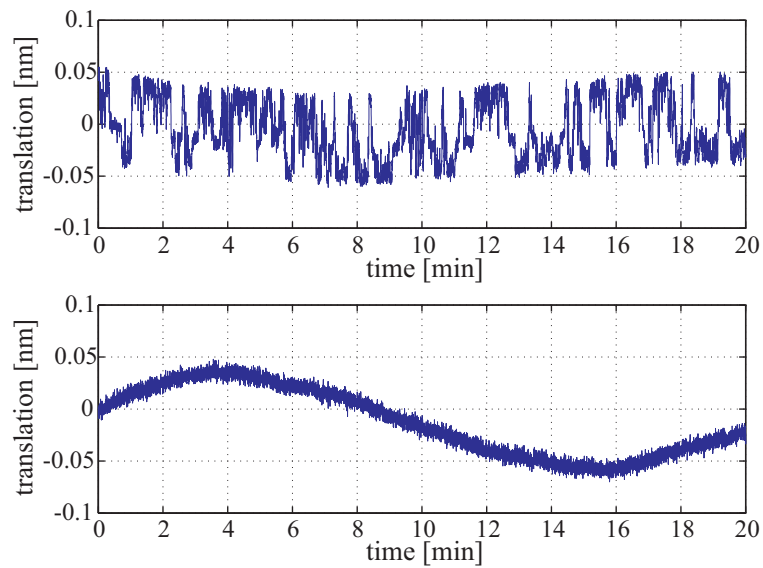


Figure 6.13.: Time series of two measurements without (upper curve) and with (lower curve) implemented phaselock. The oscillation with a wavelength of several minutes in this measurement is caused by the temperature stabilization loop.

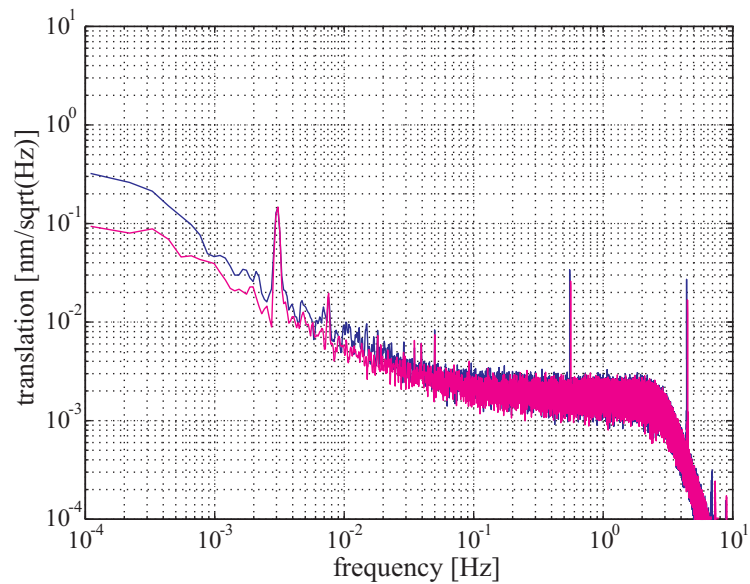


Figure 6.14.: Power spectral density of the translation measurement without (upper/blue curve) and with (lower/magenta curve) frequency stabilization of the Nd:YAG laser source.

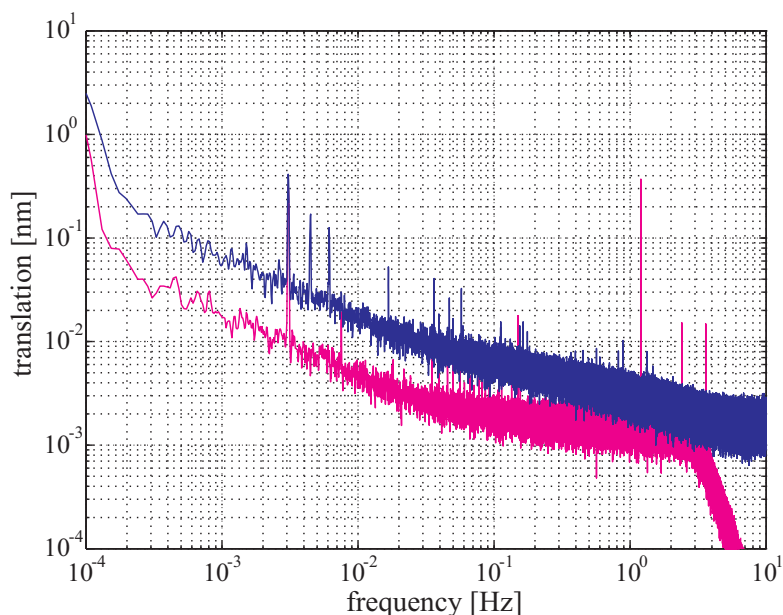


Figure 6.15.: Power spectral density of the translation measurement. The upper/blue curve is obtained by an analog phase measurement, the lower/magenta curve by a digital phase measurement.

6.8.3. Tilt Measurement

The tilt of the measurement mirror is measured in two perpendicular axis (up-down and left-right). The time series of a 60 h tilt measurement and its PSD are shown in Fig. 6.16. This tilt measurement corresponds to the 60 h translation measurement shown in Fig. 6.11; it is carried out at the same time.

6.9. Measurement of the Nonlinearities

For measuring the nonlinearities of the interferometer, the optical pathlength of the measurement arm must be varied by several fringes. This can be realized by either changing the distance l of the measurement mirror or the refractive index n in the measurement arm of the interferometer. A mechanical movement of the mirror always induces noise, we therefore designed a vacuum cell which enables a pressure scan in the measurement arm of the interferometer. Our setup and measurements will be detailed in the following.

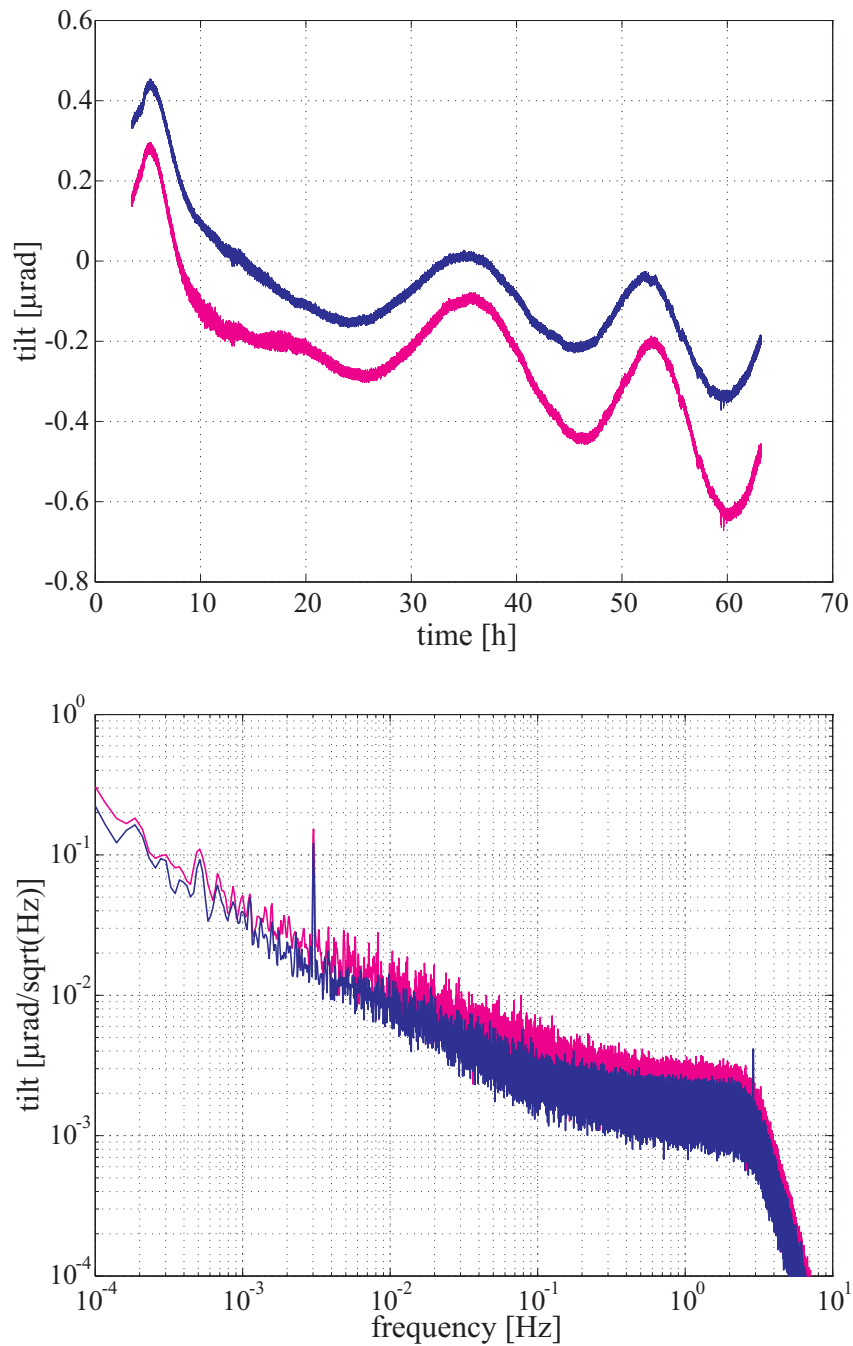


Figure 6.16.: Tilt measurement of a 60 h measurement utilizing differential wavefront sensing. The upper curve shows the measured tilt signal for two axes, the lower curve shows the corresponding calculated PSD.

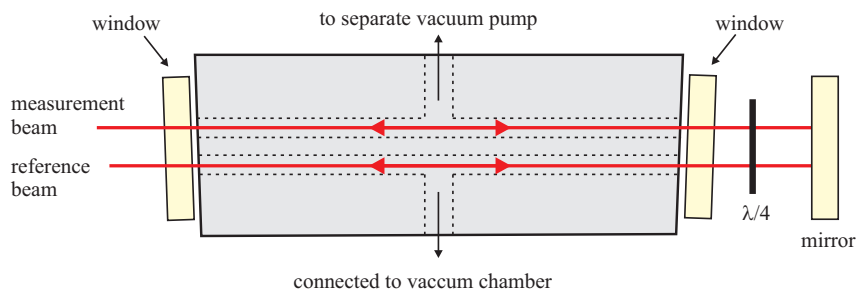


Figure 6.17.: Schematic of the gas-cell.



Figure 6.18.: Leek-tested gas-cell for measuring the interferometers nonlinearities.

6.9.1. Experimental Setup

A vacuum cell was designed, which maintains the symmetry of measurement and reference arm of the interferometer as much as possible. Its schematic is shown in Fig. 6.17, a photograph in Fig. 6.18. The length of the cell is 9 cm where reference and measurement beam are both transmitted at the same high-quality AR-coated window. The two windows are wedged with respect to each other in order to prevent Etalon effects. The cell has two identical drills for the measurement and the reference arm; the drill for the reference beam is connected to the vacuum chamber the interferometer board is placed in, the drill for the measurement beam can be evacuated via a separate vacuum pump.

As detailed in chapter 4.3.2, a pressure scan linear in time is not necessary. It is sufficient to record the interferometer's translation signal and the amplitudes of the individual QPD signals.

6.9.2. Results

In our experiments, the large vacuum chamber was operated under ambient pressure (with closed cover) and the vacuum cell's volume of the measurement beam was evacuated at the beginning of the measurement. The interferometer signal was

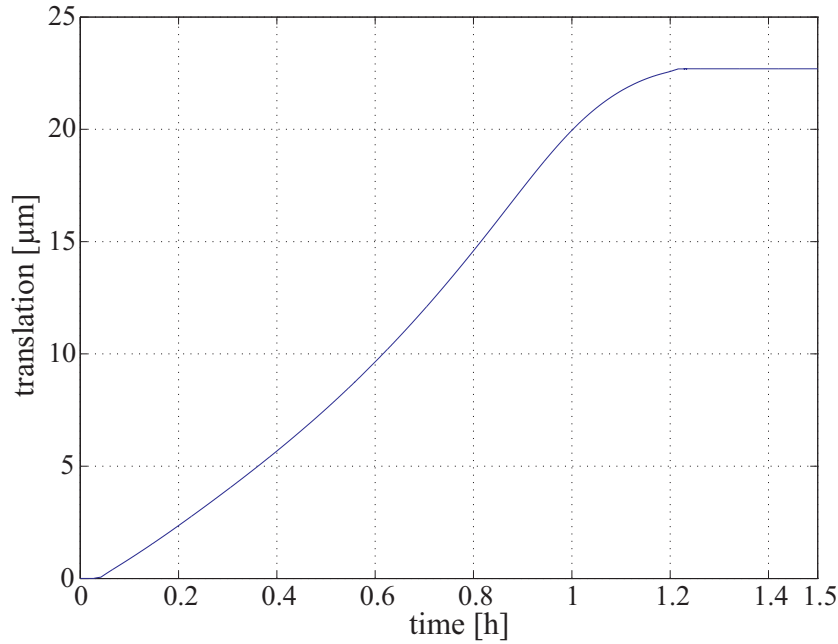


Figure 6.19.: Measured translation when venting the gas cell. The given translation corresponds to mirror displacement.

recorded during slowly venting the cell and is shown in Fig. 6.19. During ≈ 70 min, the OPD was changed by approximately $45.4 \mu\text{m}$ which corresponds to a mirror displacement of $\approx 22.7 \mu\text{m}$.

Using the dispersion equation for calculating the refractive index of air n_s in dependence of temperature, pressure and wavelength as given in [109, 110], we obtain

$$(n_s - 1) = 265 \cdot 10^{-6} \quad (6.1)$$

for $\lambda = 1064 \text{ nm}$, $T = 25^\circ\text{C}$ and $p = 101325 \text{ Pa}$. This corresponds to an OPD of $47.7 \mu\text{m}$. The slight difference to our measured value is most probably due to uncertainties in the values for ambient pressure and temperature which were not recorded but assumed.

The amplitudes of the QPD signals were recorded, the resulting nonlinearities are shown in Fig. 6.20. The value on the axis of abscissae is given by the measured translation (one fringe equals 1064 nm), and the value on the axis of ordinate is given by

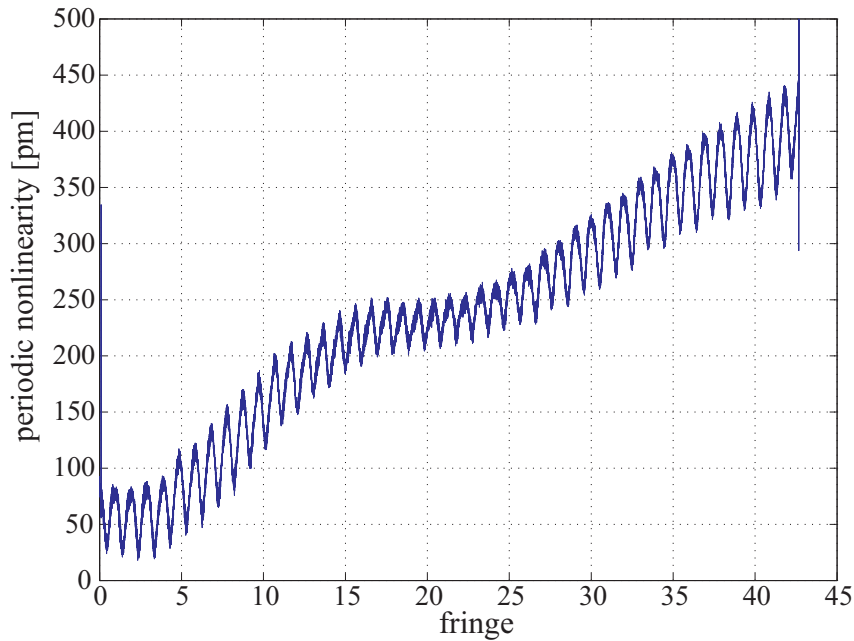


Figure 6.20.: Measured nonlinearities of the heterodyne interferometer.

$$y\text{-value} = \frac{dR}{R} = \frac{\text{amplitude sum signal QPD1}}{\text{mean value of the amplitude sum signal QPD1}} - \frac{\text{amplitude sum signal QPD2}}{\text{mean value of the amplitude sum signal QPD2}} \quad (6.2)$$

The measured nonlinearities vary between 50 and 100 pm peak-to-peak over the venting time. An FFT of the data reveals that beside a main contribution at the fringe frequency, also a smaller contribution at twice the fringe frequency is present, cf. Fig. 6.22, left.

For understanding the reason of the nonlinearities, we performed a measurement with electronically simulated signals. Therefore the two phaselocked DDS were set to 10 kHz with a slight frequency difference of 10 mHz between them. These signals are input to the FPGA computer board and replace the photodiode signals. The chosen frequency difference of 10 mHz corresponds to a translation signal which is varied by one fringe per 100 s. This measurement includes the anti-aliasing filters and the digital phasemeter; the QPD pre-amplification and the summing board are not included. The measured nonlinearities are shown in Fig. 6.21, the correspond-

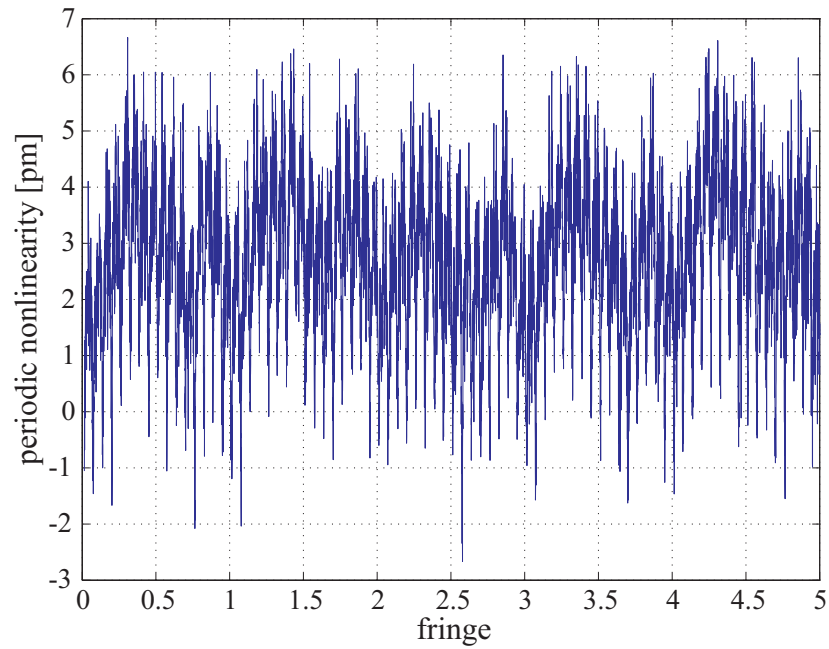


Figure 6.21.: Measured nonlinearities of the heterodyne interferometer with electronic stimuli.

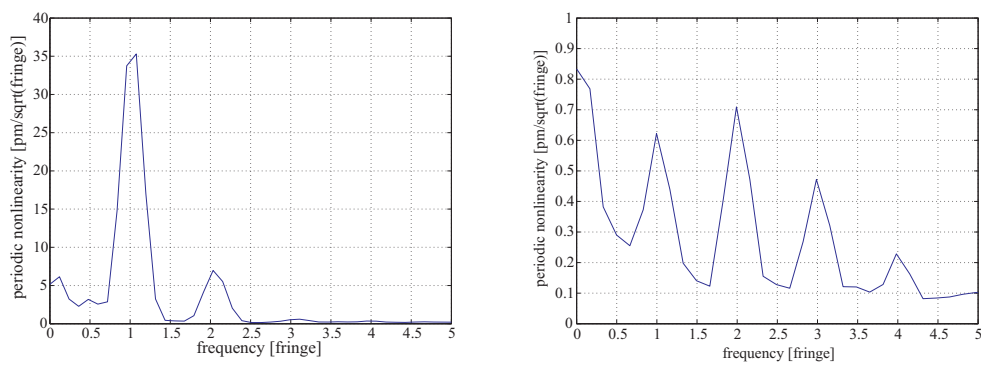


Figure 6.22.: Frequency analysis of the nonlinearity measurements. Left: signals generated by the heterodyne interferometer; Right: electronic stimuli.

ing PSD in Fig. 6.22, right. The resulting periodic nonlinearities are < 1 pm at the fringe frequency and twice the fringe frequency. The main contribution to the nonlinearities in case of electronic stimuli is at the frequency of 16 times the fringe frequency (with a PSD amplitude of $1.4 \text{ pm}/\sqrt{\text{fringe}}$, not included in Fig. 6.22, right). Therefore, the nonlinearities measured with our interferometer are either caused by the electronics (QPD pre-amplifier, summing board) and/or the optical setup (e.g. caused by straylight).

6.10. Noise Analysis

The translation noise levels achieved with the advanced setup are shown in Fig. 6.23, the tilt noise levels in Fig. 6.24. Also included are the noise levels achieved with the first setup detailed in chapter 5 and the LISA science requirements. An improvement of up to 2 orders of magnitude, both in translation and tilt noise, is achieved with the advanced setup. The achieved noise levels are close to the LISA requirements; a further decrease in noise level is still necessary.

The measured noise spectra show several characteristics which are visualized in Fig. 6.23 and Fig. 6.24:

- a white noise level at $2 \text{ pm}/\sqrt{\text{Hz}}$ (and $2 \text{ nrad}/\sqrt{\text{Hz}}$, respectively) limiting the performance of the advanced setup at frequencies between 10^{-1} to 1 Hz,
- a dominating Flicker noise ($\propto 1/f$ in power) at frequencies below 10^{-1} Hz,
- a (very sharp) peak near 3 mHz.

The noise decrease for frequencies > 3 Hz in the advanced setup is caused by the digital low-pass filter after digitization on the FPGA (4th order Butterworth with a corresponding 40 dB/decade decline). The peak near 3 Hz is caused by a missing synchronization of the FPGA clock and the DDS and is removed in later measurements.

The indicated noise levels can have a large variety of causes including photon shot noise, electronic noise (Johnson noise, electron shot noise), digitizing noise, thermal noise of the mirrors, and variations in laser intensity and frequency. Also environmental parameters as vibrations or temperature and pressure variations can be the reason. Temperature variations of the interferometer breadboard, the detectors and the electronics can be considered.

Digitizing noise: First, we checked the digital phase measurement and the correlated digitizing noise. Therefore, we split the 10 kHz quadrant photodiodes sum signals (QPD1 and QPD2) before data acquisition and digitized all four signals (resulting in QPD1₁, QPD1₂, QPD2₁, QPD2₂). We performed the phase comparison

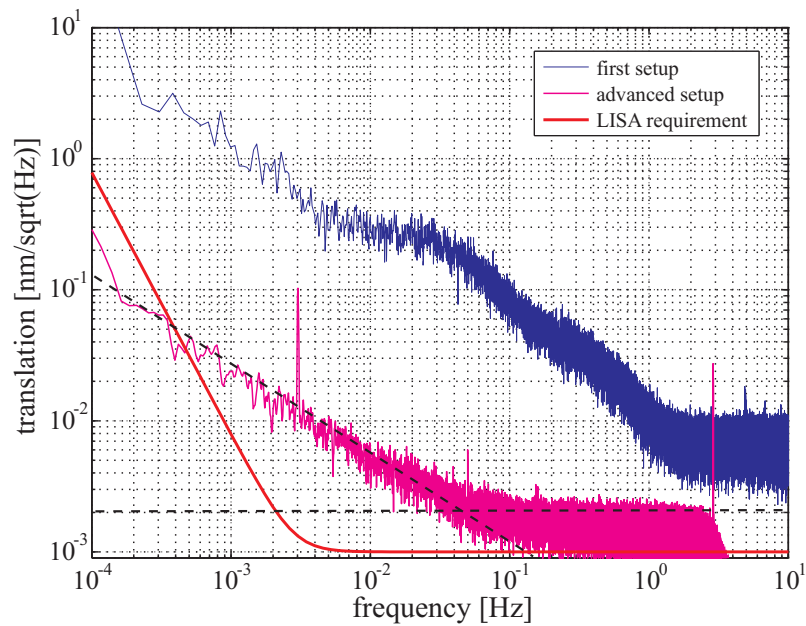


Figure 6.23.: Translation noise levels of the two realized setups. Also included are the noise levels of the advanced setup and the LISA requirements.

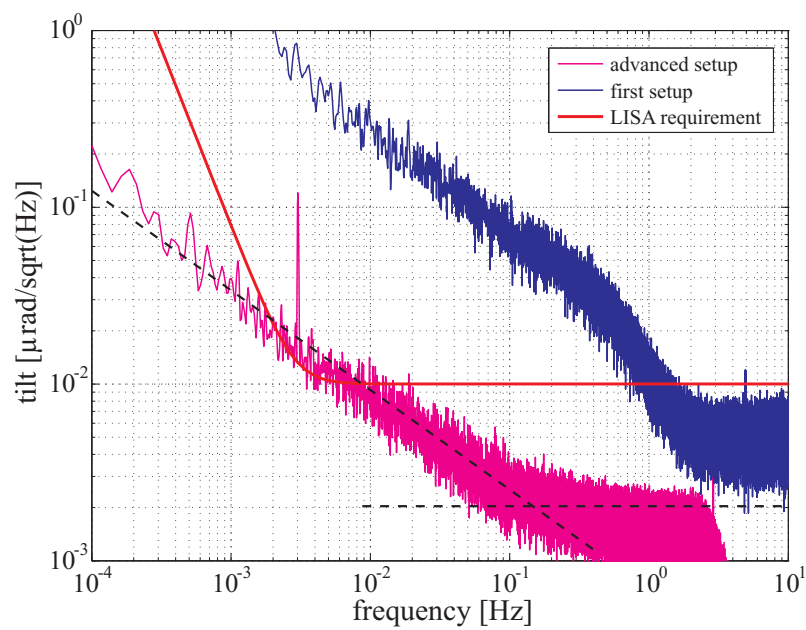


Figure 6.24.: Tilt noise levels of the two realized setups. Also included are the noise levels of the advanced setup and the LISA requirements.

on the FPGA board for both (similar) differential interferometer signals (QPD₁₁ phase compared to QPD₂₁, and QPD₁₂ phase compared to QPD₂₂) and subtracted them (cf. upper graph in Fig. 6.25). The corresponding PSD is shown in the lower graph in Fig. 6.25 and indicates that we are not limited by digitizing noise in our measurement. We also performed a phase measurement between the same signals (QPD₁₁ phase compared to QPD₁₂). The corresponding PSD is also included in Fig. 6.25. The noise level at $200 \text{ fm}/\sqrt{\text{Hz}}$ corresponds to the digitizing noise.

A measurement where the 10 kHz interferometer signals are simulated by two phase-locked function generators as input to the FPGA board reveals a similar digitizing noise level.

Noise introduced by the phase measurement: As detailed in appendix C.2, the signal phase shifted by 90° for in-quadrature readout is generated by implementing a delay in the data stream. In order to analyze its influence, we performed a translation noise measurement with delays of 90° , 450° and 810° . All delays correspond to the same phase shift equal to $\pi/2$. The PSD of the measurements are shown in Fig. 6.26. It can clearly be seen, that the delay has no influence on the high-frequency noise level of $2 \text{ pm}/\sqrt{\text{Hz}}$ but with increasing delay time, the noise at lower frequencies increases. The peak near 3 mHz has the same amplitude in all measurements.

Electronic noise: Electronic noise can be subdivided in electron shot noise (due to a quantized current leading to a statistically described current), Johnson noise caused by equilibrium fluctuations of the electric current and Flicker noise ($1/f$ -noise). Shot noise and Johnson noise have no frequency dependency (white noise) and are caused by physical principles and can therefore not be minimized.

Shot noise: The shot noise limit is the same as given in chapter 5.6 and corresponds to approximately $1.4 \cdot 10^{-14} \text{ m}$.

Influence of laser frequency noise: To investigate an influence of a change in laser frequency, a slow sine function was applied to the PZT mounted to the laser crystal ('fast modulation input') while recording the translation signal. The measurement with a sine wave with a frequency of 0.3 Hz and an amplitude of 20 Vpp (corresponding to a change in frequency of about 20 MHz peak-to-peak) results in a frequency dependency coefficient of approximately 1.5 pm/MHz .

Conclusion

In conclusion, it can be stated that we are not limited by digitizing noise, photon shot noise, and laser frequency noise. Electronic noise was not further investigated in this thesis but is assumed to be a limiting factor. A future investigation with respect to electronic noise in the detector preamplifier and the summing board should be carried out. Also, thermal effects can limit our performance in the low-frequency range. With a new interferometer setup, based on thermally highly stable glass ceramics such as Zerodur or ULE, this limitation can be analyzed in more detail.

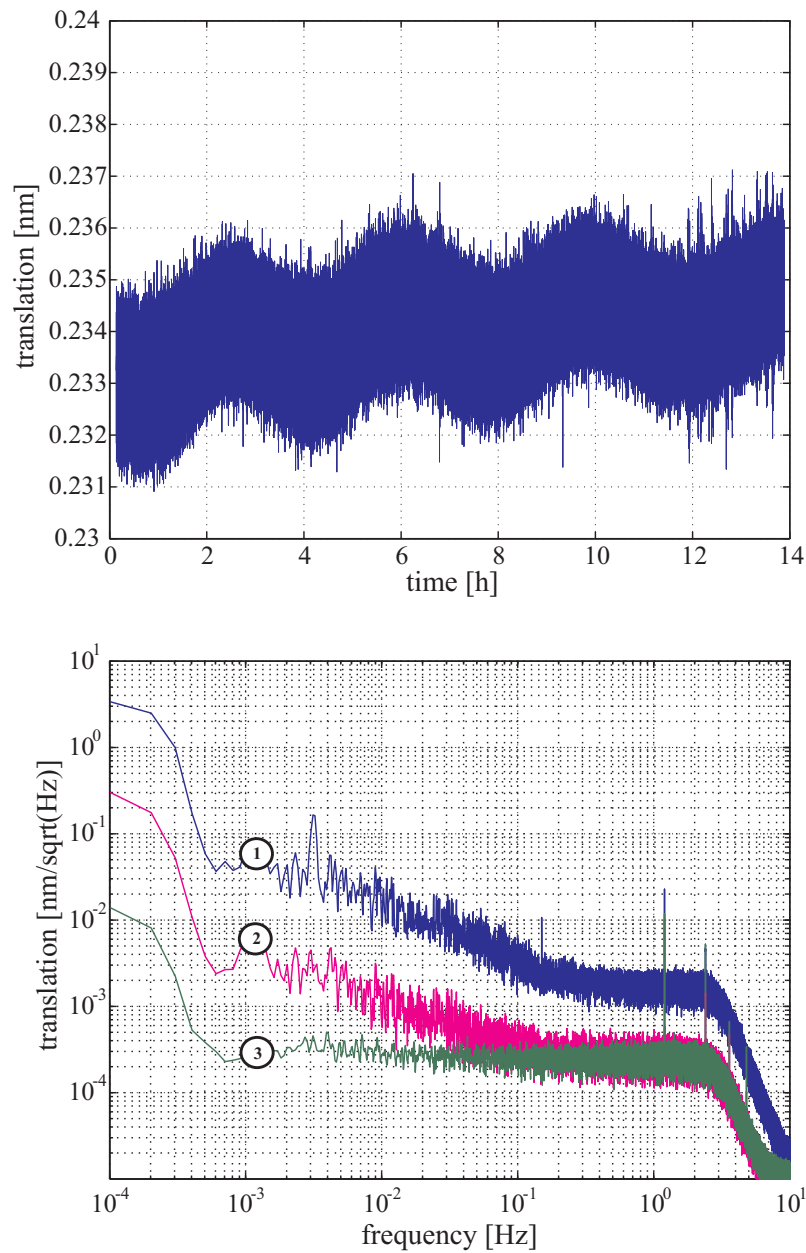


Figure 6.25.: Upper graph: difference of the two time series of two similar digitized differential interferometer signals. Lower graph: Noise measurement. 1. PSD of the differential interferometer with intensity stabilization and phaselock (blue curve); 2. PSD of the mixing of two identical signals (sum signal of QPD1, magenta curve); 3. PSD of the difference of two separately mixed differential interferometer signals (calculated of the upper graph, green curve).

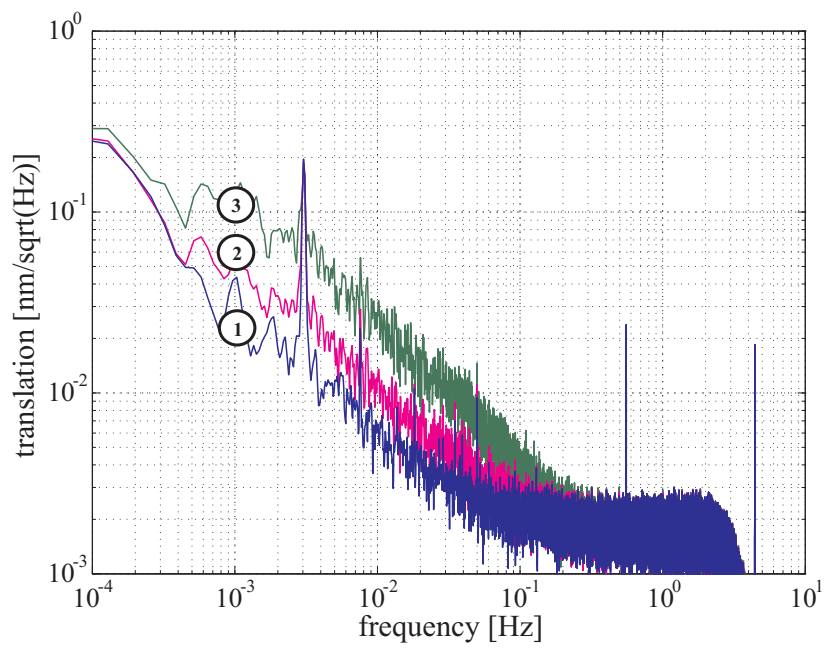


Figure 6.26.: PSD of the translation measurement where the phase shift for in-quadrature measurement was varied. 1: 90° ; 2: 450° ; 3: 810° .

7. Applications

Our interferometer is developed with respect to the requirements of the optical read-out of the LISA gravitational reference sensor but it represents much more generally a high-sensitivity test facility for measuring translation and tilt of a reflective surface at one single spot. This sensor – as it is – can for example be used for nano-positioning control (e. g. for controlling a translation stage of an atomic-force microscope (AFM) in the picometer range), calibration of capacitive sensors and as high-precision displacement sensor in seismometers¹. Our interferometer can also be used for characterizing high-precision actuators on the picometer and nanoradian level. This is of importance with respect to LISA, as its optical bench includes actuators which are part of the scientific measurement and therefore have to fulfill the stringent requirements given in Table 2.1. In the following, the interferometer’s adaptation for use in high-precision dilatometry and optical profilometry is presented.

7.1. Dilatometry

The interferometer as described in this thesis is currently used for measuring the linear coefficient of thermal expansion of thermally and mechanically highly stable materials, such as carbon-fiber reinforced plastic (CFRP) or Zerodur [113, 114, 115, 116, 117]. CFRP is the standard material for spacecraft structures due to its mechanical and thermal properties, in combination with low mass. It is also foreseen as spacer material for the LISA telescope mirrors where a CTE below 10^{-7} K^{-1} is required.

The linear coefficient of thermal expansion (CTE) is given by

$$CTE = \frac{1}{L} \cdot \frac{\Delta L}{\Delta T} \quad (7.1)$$

where ΔL is the change in length of a sample with length L when a change in temperature ΔT is applied.

¹An interferometric seismic sensor can e.g. be found in [111, 112] where the measurement frequency band is 10^{-4} Hz to 30 Hz .

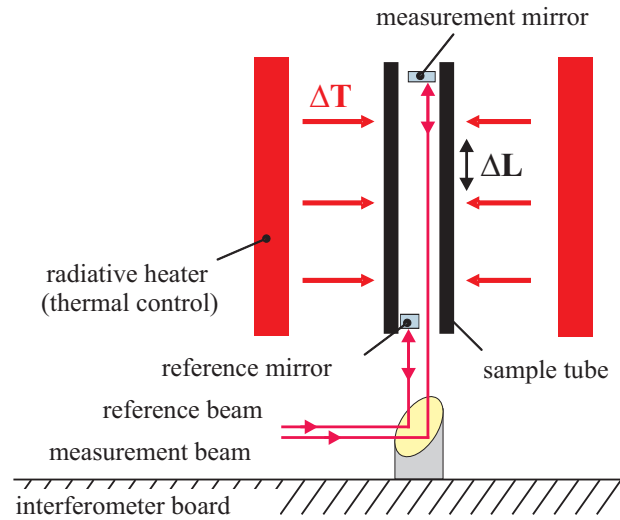


Figure 7.1.: Measurement concept of our dilatometer. The interferometer measures a change in length, ΔL , of a sample tube when a change in temperature, ΔT , is applied.

7.1.1. Measurement Concept

The principle of our CTE measurement is shown in Fig. 7.1. Reference and measurement mirror of the interferometric measurement are fixed inside a tube made of the material under investigation. The tube is placed inside a heating where a change in temperature, ΔT , of the tube causes an expansion (or contraction), ΔL , of the tube. The change in distance between the two mirrors is measured with sub-nanometer sensitivity by use of the heterodyne interferometer.

7.1.2. Experimental Setup

For the CTE measurements, a 12 cm long sample tube is vertically mounted, compensating for the gravitational caused contraction of the upper half of the tube and expansion of the lower half of the tube. The measurement mirror is clamped inside the tube's upper end and the reference mirror inside the tube's lower end. The interferometer measures the changes in distance between measurement and reference mirror, i.e. the expansion (or contraction, respectively) of the tube. The tube is surrounded by a radiation heating (copper cylinder with thermo-electric coolers). Temperature changes are supplied by controlling the peltier elements with a PID temperature controller whose DC modulation input is driven by a function generator. Several Pt100 temperature sensors are glued to the copper cylinder and the sample tube by use of high thermal conductivity epoxy. They provide the actual temperature and their gradients. One sensor at the middle inside of the tube pro-

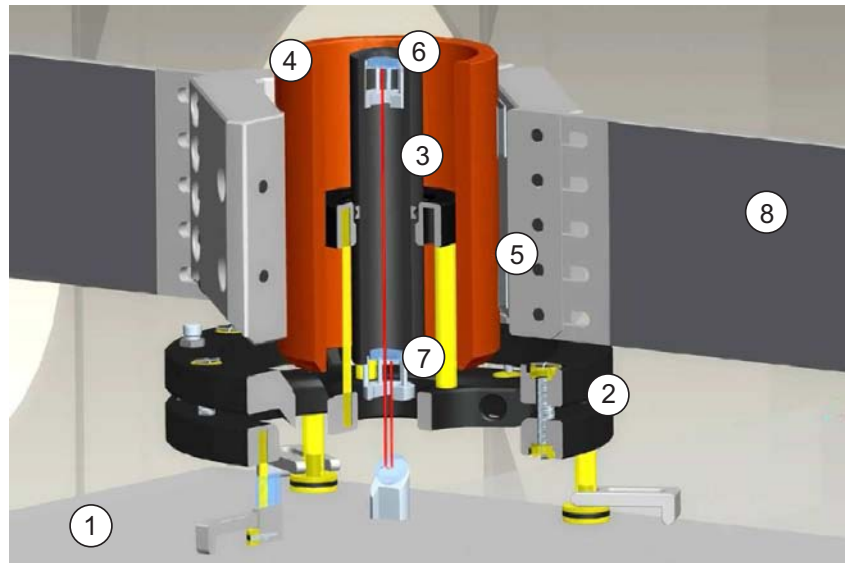


Figure 7.2.: Engineering CAD drawing of the existing facility for measuring the thermal stability of a sample tube. 1: interferometer board, 2: tube support, 3: sample tube, 4: copper cylinder, 5: Peltier elements, 6: measurement mirror, 7: reference mirror, 8: heating support. [113]

vides the control variable for the PID controller. The temperature of the tube can be varied in a temperature range between 20°C and 60°C. A CAD drawing of the setup is shown in Fig. 7.2 and a photograph in Fig. 7.3.

The mirror clamps that fix the mirrors inside the sample tube are specifically designed in order not to influence the CTE measurement. Invar36, an iron-nickel alloy with a very low coefficient of thermal expansion $< 10^{-6} \text{ K}^{-1}$ was chosen as material. Each clamp is made up of six legs of the same length. Three of them fix the clamp to the inner surface of the tube, the other three legs fix the mirror inside the clamp, as seen in Fig. 7.4. The reflective mirror surface together with the six clamping points of the clamp legs define a thermally neutral plane, which in case of a thermal expansion of the clamp due to a temperature variation keeps the reflective mirror surface unmoved.

7.1.3. Experimental Results

We first performed a measurement with a CFRP tube whose CTE value was already specified in previous measurements²:

²The tube was manufactured with respect to the MSG-Seviri mission requirements and characterized by use of a vertical Netzsch dilatometer TMA 402.

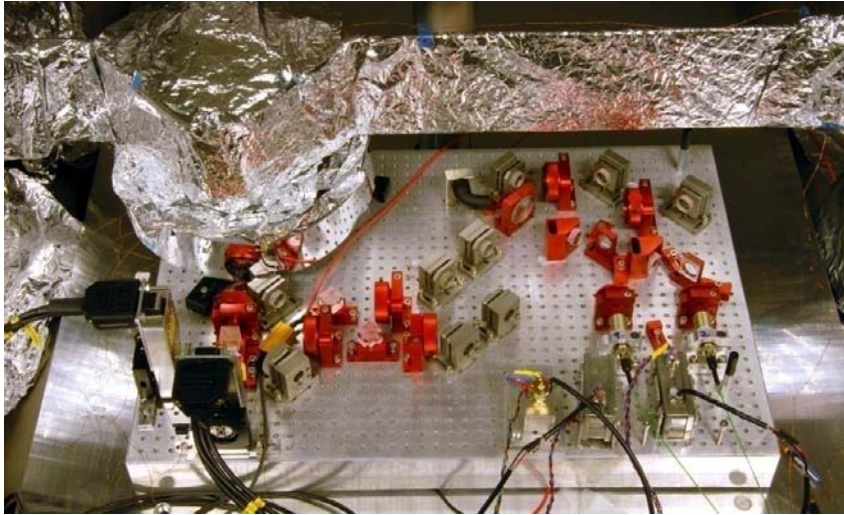


Figure 7.3.: Photograph of the CTE measurement facility. Shown is the interferometer board with mounted sample tube support and heating. The heating is covered by multilayer insulation (MLI) foil.

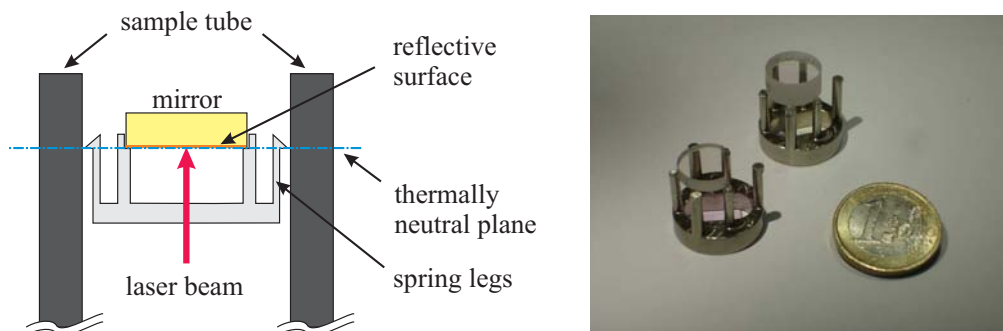


Figure 7.4.: Left: schematic of the mirror mount. The reflective surface of the mirror and the clamping points of the mount inside the tube define a thermally neutral plane. Right: photograph of the mirror mounts.

$$CTE_{meas,Netzsch} = (-1.1 \pm 0.03) \cdot 10^{-6} \text{ K}^{-1} \quad (7.2)$$

$$CTE_{theo} = -0.647 \cdot 10^{-6} \text{ K}^{-1} \quad (7.3)$$

The theoretical value is calculated out of the matrix-fiber ratio and the fiber plies angle. The sample tube used in our experiments has a length of 120 mm, an outer diameter of 27.2 mm and an inner diameter of 20.0 mm. Different temperature variations – such as sine and square wave functions – were applied to the temperature controller. Measurements with different offset temperatures, amplitudes and frequencies were carried out.

The CTE value is calculated via equation (7.1) where ΔL is obtained by the interferometer measurement, ΔT by use of high-sensitivity Pt-100 temperature sensors and L using a mechanical gauge. Different evaluation methods were applied to the measurement data (ΔL and ΔT); the CTE values given in the following are derived from our measurement data.

- *hysteresis evaluation*: A periodical sine thermal cycling is applied to the sample tube and the length variation ΔL is plotted over the temperature variation ΔT . A hysteresis curve is obtained where the CTE can be calculated by applying a linear fit to it.

$$CTE = -0.55 \cdot 10^{-6} \text{ K}^{-1}$$

- *frequency analysis*: A sine thermal cycling is applied and the power spectral densities of the measured time series ΔL and ΔT are calculated, revealing a peak at the thermal cycling frequency. The ratio of the corresponding peak values yields to the CTE value. This method is only suitable for long measurements with a large number of applied sine cycling periods.

$$CTE = -0.54 \cdot 10^{-6} \text{ K}^{-1}$$

- *sine fit*: A sine thermal cycling is applied and the measured ΔL and ΔT values are segmented into single periods. To each period, a sine is fitted whose amplitudes yield to a single period CTE value. The mean value of the single period CTE values gives the resulting CTE.

$$CTE = -0.56 \cdot 10^{-6} \text{ K}^{-1}$$

As result, all evaluation methods yield to a comparable CTE value close to the theoretical value. The difference to the theoretical CTE value can either be a property of the tube itself or a systematic error of our measurement facility. A future measurement with a tube with a defined CTE (e.g. a tube made of zero-class Zerodur) will provide more information.

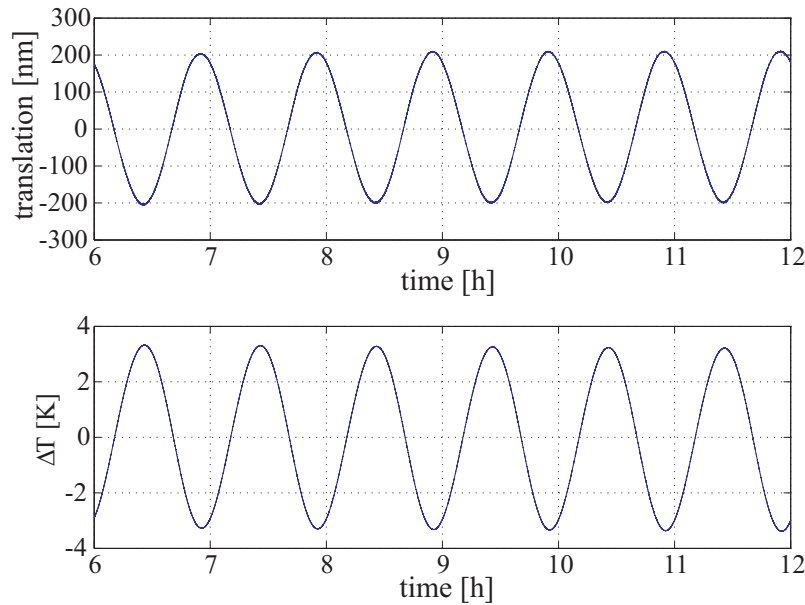


Figure 7.5.: CTE measurement. The upper curve shows the change in length of the tube, the lower curve the temperature measured at the tube.

A typical measurement with sine thermal cycling and a period of 1 h is shown in Fig. 7.5. Shown is the temperature measured at the tube and the expansion/contraction of the tube. The temperature was varied by about ± 3.1 K at an offset temperature of 30°C .

7.1.4. Limitations and Next Steps

The measurements shown above demonstrate the capability of measuring the material CTE with values below 10^{-6} K^{-1} . They confirm the theoretical value of the sample. In a current activity, we improve the design of the mirror clamps as it was seen that the current clamps scratch the inner surface of the tube. This might have an influence on the obtained CTE value. Also, due to rather high spring forces, these clamps are not suitable for a tube made of Zerodur which is rather brittle. The Zerodur tube with a predicted CTE value of $-1 \cdot 10^{-8} \text{ K}^{-1}$ will be taken as reference for our facility in order to analyze our measurement sensitivity and systematic effects. We will also manufacture a CFRP tube with a predicted (theoretical) CTE value below 10^{-9} K^{-1} and verify its thermo-mechanical properties with our setup. Since a relative tilt of the two mirrors induce a translation error, the DWS signals can provide a correction for the translation data.

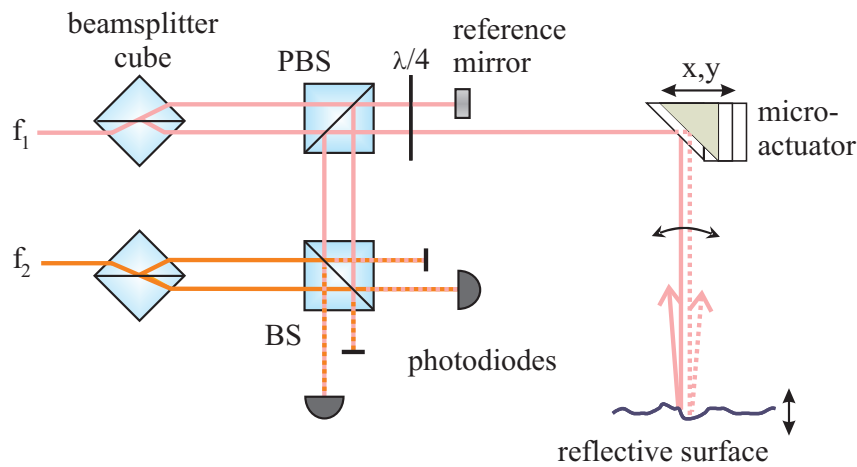


Figure 7.6.: Schematic of the extension of our interferometer for use as profilometer. The micro-actuator enables a scan of the measurement beam of the interferometer over the surface under investigation.

7.2. Profilometry

The interferometer developed with respect to LISA requirements measures translation and tilt at one single laser beam spot. For surface property measurements, as e.g. roughness, evenness and roundness, a scan of the interferometer's measurement beam over the surface under investigation is necessary. Either the device under test (DUT) or the measurement beam of the interferometer is actuated with respect to each other. A schematic of a profilometer with actuation of the measurement beam is shown in Fig. 7.6.

Special care has to be taken on the beam reflected by the surface under investigation as problems might occur due to limited reflectivity and non-normal angle. As the translation information is integrated over the beam diameter, a lens in the measurement beam will be needed placing the focus on the test surface. A resulting lateral resolution in the μm -range should then be possible. In order to overcome the limited dynamic range of the actuator, the optical sensor can be used together with a three axes coordinate measuring machine, the latter offering a dynamic range up to several meters and positional resolutions below $0.1 \mu\text{m}$. The high sensitivity of the optical sensor is then combined with the large dynamic range of the coordinate measuring machine.

One specific issue in the context of surface property measurement is the characterization of mirror surfaces in the pm-range for the LISA space mission. This information is important in case of actuated mirrors, where the beam is reflected at different locations of the mirror with time.

7.2.1. Experimental Setup

In a first profilometer setup, we use our interferometer as described in chapter 5, where the measurement mirror is mounted on an x-y piezo-electric actuator.³ As laser source, we utilize the DBR laser module (cf. appendix F) in combination with two AOMs. The corresponding AOM RF signals are generated by use of two phaselocked function generators (SRS DS345) in combination with appropriate amplifiers and filters. The heterodyne frequency is set to 1 kHz; the two frequencies are fiber coupled to the interferometer board, cf. the photographs shown in Fig. 7.7 and Fig. 7.8. The interferometer board is operated at normal pressure in a laboratory without air conditioning. During the measurements the setup is covered by a cardboard box in order to minimize influences by air turbulence.

The signals from the reference and measurement quadrant photodiodes are pre-amplified, anti-aliasing filtered, and the heterodyne signals are directly digitized by use of a National Instruments data acquisition board (model M6229). As its maximum sample rate is 250 kS/s, a low heterodyne frequency (in our case 1 kHz) is necessary in order to keep digitizing and synchronizing effects small. A 1 kHz reference signal is generated by mixing the two RF signals driving the AOMs; this signal is also input to the NI data acquisition board (together with its corresponding 90° phase shifted signal for IQ, using an analog phaseshifter) and taken for mixing the heterodyne input signals. A LabVIEW program carries out the in-quadrature translation measurement and also controls the position of the PZT by supplying a control voltage to the control input of the PZT driver. In order to minimize vibrations of the PZT setup, a step function with smoothed steps is used for PZT actuation. A data matrix containing the information on the x-y position of the actuator and the measured z-component is generated as output of the program. The setup for profilometry and the corresponding LabVIEW programs are described in detail in [118, 119, 120].

7.2.2. First Measurements

We first performed a noise measurement with implemented x-y PZT actuator. The PZT was not actuated and the translation noise was measured for several hours. The corresponding PSD is shown as upper curve in Fig. 7.9. A noise level of approximately $1 \text{ nm}/\sqrt{\text{Hz}}$ was achieved for frequencies near 1 Hz. The lower curve corresponds to the initial interferometer setup as detailed in chapter 5. The noise performance of the profilometer setup is degraded by one to two orders of magnitude. Reasons are the operation of the interferometer under ambient pressure and

³Provided by PI, model P-625.20L. The stroke is $600 \mu\text{m}$ per axis with 0.5 nm resolution. A PI PZT driver, model E505, with a control input (-2 V to +10 V) is used for supply of the PZT voltage.

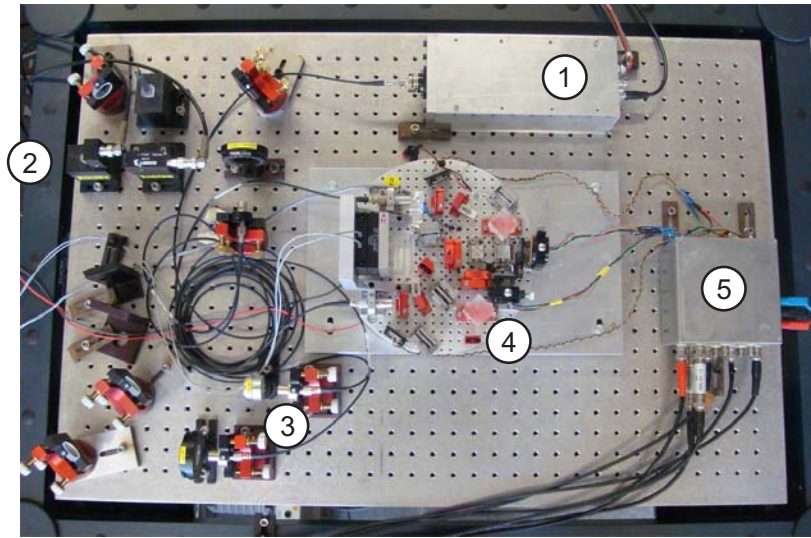


Figure 7.7.: Photograph of our interferometer setup adapted for optical profilometry. Shown are the DBR laser module (1), the optics for heterodyne frequency generation including AOMs (2) and fiber coupling (3), the interferometer board (4) and the analog electronics for the quadrant photodiodes (5).

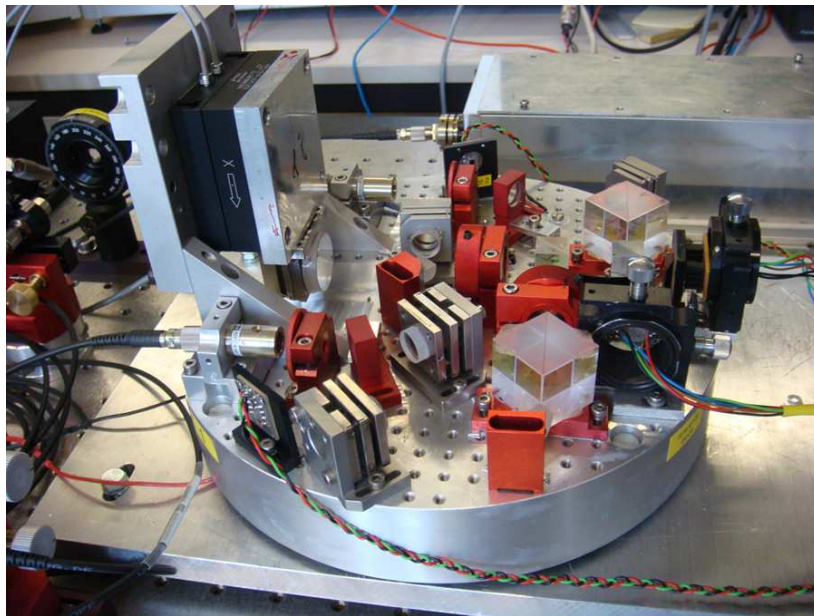


Figure 7.8.: Photograph of the interferometer board. The measurement mirror is placed on an x-y PZT translation stage.

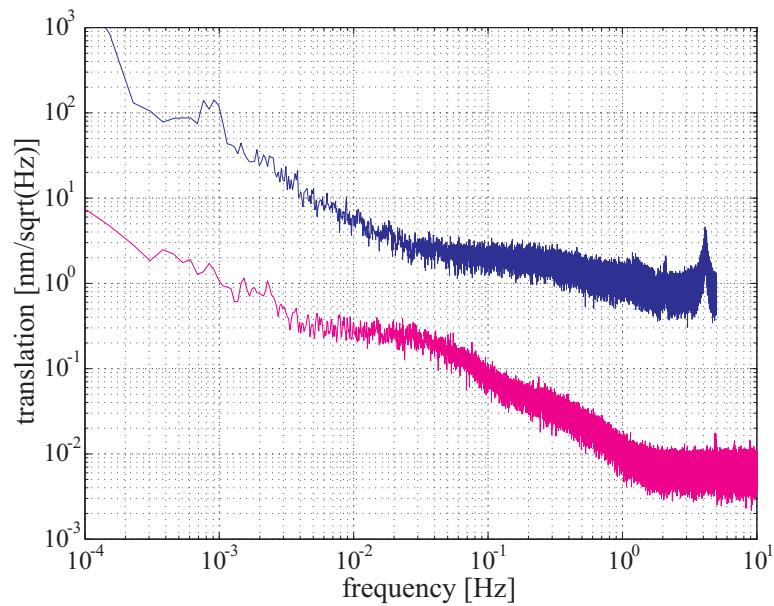


Figure 7.9.: Power spectral density of the interferometer setup for profilometry (upper curve). The noise performance of the original interferometer setup is shown for comparison (lower curve).

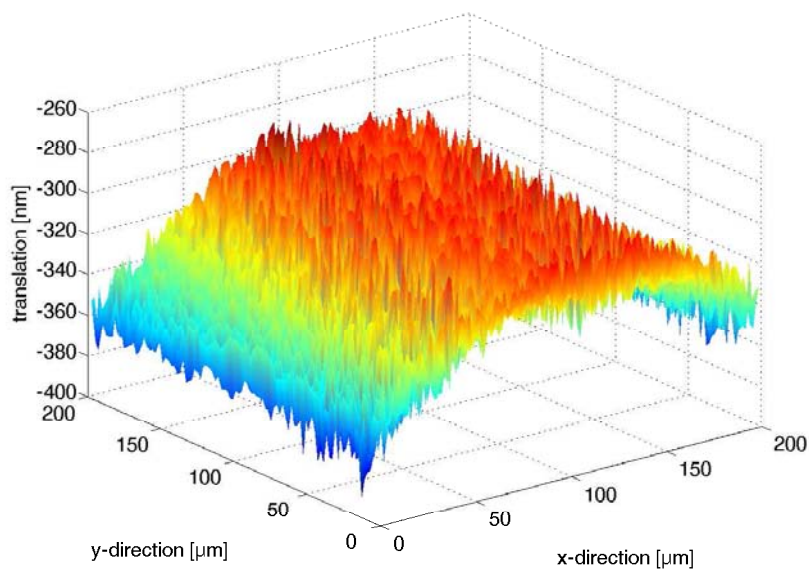


Figure 7.10.: Preliminary profilometer measurement of a $200 \mu\text{m} \times 200 \mu\text{m}$ area of a high-reflective mirror surface.

temperature in a laboratory without air-conditioning, a mechanically not optimized mounting of the PZT, the low heterodyne frequency of 1 kHz, and the direct, non-synchronous, digitization of the 1 kHz heterodyne signals. The profilometer setup shows a temperature coefficient of about 700 nm/K.

A preliminary surface measurement is shown in Fig. 7.10. For each direction, x and y, the PZT is moved by 100 steps scanning a $200\ \mu\text{m} \times 200\ \mu\text{m}$ area of a high-reflective mirror surface. In the measurement, a linear drift in both directions is subtracted. The measured profile is most probably caused by a lateral movement of the PZT and not a property of the surface. For further investigation, we will in a next step implement a PZT with a larger stroke (several millimeters) and add a lens in the optical path, focussing the beam onto the surface under investigation.

8. Conclusion and Next Steps

In this thesis, a heterodyne interferometer using polarizing optics was developed and two interferometer setups were realized. With the advanced setup, we demonstrated noise levels below $2 \text{ pm}/\sqrt{\text{Hz}}$ in translation and below $3 \text{ nrad}/\sqrt{\text{Hz}}$ in tilt measurement, both for frequencies above 10^{-1} Hz . Towards lower frequencies, both noise curves show a near $1/f$ Flicker behavior. Intensity stabilization and phaselock of the fiber output beams were implemented in the advanced setup. They reduce the noise level up to one order of magnitude at frequencies around 10^{-2} Hz and are essential for obtaining a few pm noise level. Using an FPGA for phase comparison clearly improves the noise performance as shown in our second setup where the noise level was reduced by a factor of about 3 over the whole LISA frequency range.

The noise levels achieved with our second setup are included in Table 8.1. They are compared to the measured noise levels achieved in other optical readout implementations (cf. chapter 3.3). With our setup we demonstrated very low translation and tilt noise levels; lower noise levels are only demonstrated with the LTP interferometer. The LTP interferometer is realized on engineering model (EM) level, using a complex assembly-integration technology where the baseplate is made of Zerodur and the optical components are integrated using hydroxide-catalysis bonding. Our interferometer is realized using a cast aluminum breadboard; the optical components are mounted in aluminum and stainless steel mounts and fixed to the breadboard using standard M3 screws.

The achieved noise levels of our interferometer are close to the LISA requirements but it is necessary to further reduce the white noise floor at higher frequencies, and to shift the $1/f$ -increase in noise towards lower frequencies. We investigated digitizing noise, photon shot noise, and laser frequency noise – which currently all do not present a limitation. In a next step, a total noise breakdown should be carried out, including the Flicker and random-walk noise at lower frequencies, the white noise level of 2 pm at higher frequencies and the origin of the peak near 3 mHz . The most probable noise source is electronic noise, at lower frequencies also thermal effects might be a limiting factor.

For a more comprehensive understanding of the setup, following items can be investigated in more detail:

- The phaselock is currently realized using an additional photodiode after fiber outcoupling. It should also be possible, to use the sum signal of the reference

	translation noise [pm/ $\sqrt{\text{Hz}}$] @ 1 mHz @ 0.1 Hz	tilt noise [nrad/ $\sqrt{\text{Hz}}$] @ 1 mHz @ 0.1 Hz	remarks
ORO			
University of Napoli (lever sensor)	6000 80	50 5	+ very compact setup + already integrated in existing LISA GRS design – limited sensitivity, only applicable for DFACS
Stanford University (Littrow grating)	5000 40	—	+ very compact – no tilt measurement – based on a LISA GRS design with spherical PM
University of Birmingham (homodyne, polarizing)	200 10	—	+ very compact setup – no tilt measurement
LTP interferometer (heterodyne, non-polarizing)	50 0.5	20 1	+ very stable setup, thermal and vibration tested – very complex integration technology – non normal beam incidence on the proof mass
this thesis (heterodyne, polarizing)	25 2	30 3	+ easy to handle integration technology + can be realized very compact

Table 8.1.: Comparison of the noise levels achieved with different LISA optical readout implementations.

quadrant photodiode making the optical setup less complex by maintained performance.

- The electronics used for generating the sum signal of the quadrant photodiodes and the signals for DWS is currently realized using analog electronics. In an improved FPGA program all single quadrants of both quadrant photodiodes are input signal to the FPGA computer board. Therefore, the summing can be implemented on the FPGA. This enables a tilt measurement of both mirrors at the same time and reduces the amount of analog electronics which is assumed to be a limiting factor. It is recommended to realize as much as possible of the electronics directly on the FPGA.
- By use of two phase-locked lasers for generating the heterodyne frequencies, the sidebands of the AOMs are obsolete. Their influence on the measured noise levels can then be investigated in more detail.
- Our interferometer setup utilizes polarizing optics, but it can easily be adapted to a non-polarizing setup. The PBS is then replaced by a BS and the waveplates are omitted. With this setup, a possible limitation caused by temperature dependent polarization effects can be investigated. While increasing the complexity, a non-polarizing setup has a potential lower noise level, especially at lower frequencies.

Beside its application aboard the LISA satellites, the interferometer is adapted for dimensional characterization of ultra-stable materials such as carbon-fiber reinforced plastic (CFRP). This is of special interest also for space applications, as the main spacecraft structure material is based on CFRP. Our facility enables the measurement of the linear coefficient of thermal expansion (CTE) in a temperature range between 20°C and 60°C. Our interferometer, in principle, offers a $\sim 50 \text{ pm}/\sqrt{\text{Hz}}$ sensitivity in tube expansion/contraction measurement at an integration time $\tau = 1 \text{ h}$. Due to the implementation of the tube support and the heating subsystem, this sensitivity is reduced to nanometers. Therefore the characterization of materials with a CTE as low as 10^{-9} K^{-1} should be possible. In first experiments we measured the CTE of a tube made of CFRP and demonstrated a resolution of 10^{-7} K^{-1} in CTE measurement. In a next step, we will measure the CTE of a tube made of Zerodur for (macroscopic) calibration of our test facility. The results will be taken for further evaluation of our measurement resolution and systematic errors.

The first interferometer setup is also adapted for use in industrial metrology, especially in optical profilometry. A first setup was realized using a DBR laser diode at 1064 nm as light source. Nanometer-interferometry and the feasibility of a 3D surface scan were demonstrated.

Future Miniaturized Setup

As a next step, we develop a very compact and quasi-monolithic setup where the baseplate is made out of a thermally stable ultra-low expansion glass material, e.g. Zerodur with a thermal expansion coefficient of $2 \cdot 10^{-8} \text{ K}^{-1}$ at room temperature. The optical components are made out of fused silica and either glued to the baseplate using a two-component epoxy or connected to it via hydroxide-catalysis bonding [38]. With this setup, the temperature coefficient of the interferometer should be small enough to verify its performance down to $5 \cdot 10^{-5} \text{ Hz}$ and to reduce the noise levels at lower frequencies.

A possible implementation of such a small fiber-coupled module is shown in Fig. 8.1 and Fig. 8.2. In this design, the two frequencies are on opposing sides of the Zerodur baseplate reducing straylight influences. Also, the heat dissipating quadrant photodiodes (eventually with adjacent pre-amplifiers) are shielded to the proof mass by the Zerodur mounting angle. Monitor photodiodes after fiber outcoupling are not included in the schematic, the phaselock is foreseen by using the signal on the reference photodiode.

This miniaturized interferometer can also be the basis for a sensor head used in industrial environment. Here, also the mounting of the optical components to a baseplate made of Invar, an iron-nickel alloy with a CTE $< 2 \cdot 10^{-6} \text{ K}^{-1}$, might be sufficient. The optical components can then be glued to the baseplate making the assembly-integration process less difficult.

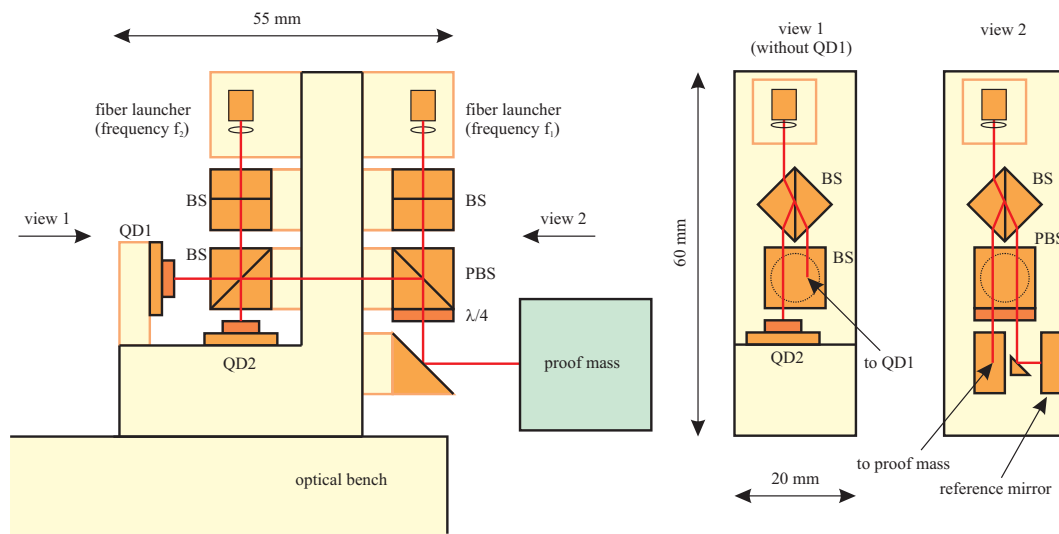


Figure 8.1.: Sketch of a possible quasi-monolithic interferometer implementation utilizing thermally stable glass materials and hydroxide-catalysis bonding technology.

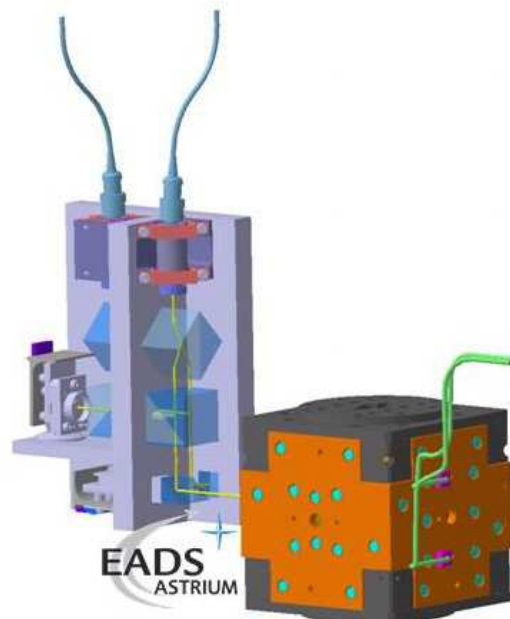


Figure 8.2.: Engineering CATIA drawing of the quasi-monolithic interferometer design. Shown to the right is the proof mass with its surrounding electrode housing.

A. Compact Frequency Stabilized Laser System

As part of a project realizing a Bose-Einstein condensate (BEC) under micro-gravity at the ZARM drop tower in Bremen (Germany), a compact fiber-coupled laser module for laser cooling and trapping was developed [121]. The laser source is a DBR (Distributed Bragg Reflector, also cf. appendix F) laser diode with a wavelength of 780 nm, frequency stabilized to an atomic transition in Rubidium. The whole setup for BEC generation must fit in a cylindric 2 m long drop capsule with a diameter of 80 cm and must be capable to be operated remote controlled. The deceleration at the end of the fall is up to 50 g. Therefore, essential design drivers for all parts of the setup (including the laser system), are compactness, robustness, low mass, low power consumption and the capability to control the setup via computer interfaces.

Our laser module is shown in Fig. A.1. For mechanical stability and compactness a beam height of 2 cm was chosen. All mounts for optical components, including rotation mounts for waveplates and polarizers, mounts for beamsplitter cubes, lens mounts and mirror mounts (in adjustable and non-adjustable versions) were purpose-built items.

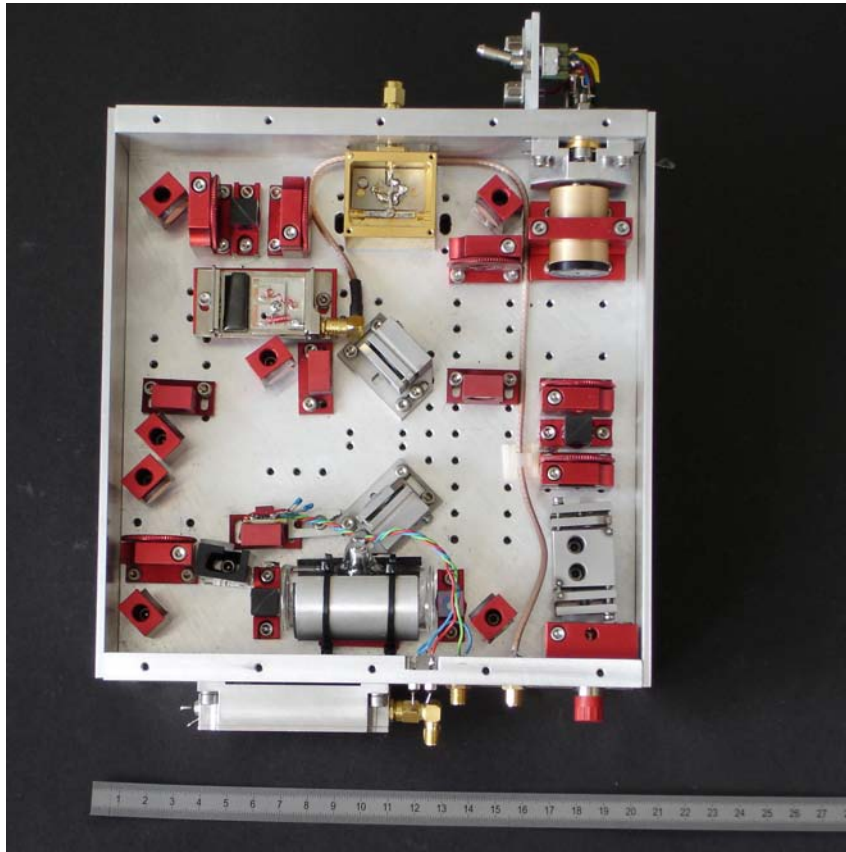


Figure A.1.: Photograph of the DBR laser module including frequency stabilization to an atomic transition in Rubidium. Shown is the stabilization by use of Frequency Modulation Spectroscopy (FMS), but the setup can easily be changed to Modulation Transfer Spectroscopy (MTS).

B. Electronics

B.1. Quadrant Photodiode Electronics

The schematic of the quadrant photodiode preamplifier is shown in Fig. B.2. It is based on a design provided by the Albert-Einstein-Institute Hannover. For our second experimental setup, we realized an SMD version with an additional LT1127 offset adjustment potentiometer (not shown in the schematic). The SMD version is housed in a shielded aluminum box placed in the vacuum chamber (cf. the photograph in Fig. B.4). The signals are differentially fed through to the summing board placed outside the vacuum chamber. Its schematic is shown in Fig. B.3. The input signals are the (differential) signals from the quadrant diode; the board generates the following signals:

1. $A+B+C+D$
2. $A+B$
3. $C+D$
4. $A+D$
5. $B+C$
6. $(A+B)-(C+D)$
7. $(A+D)-(B+C)$

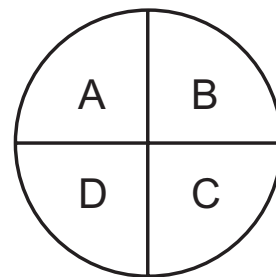
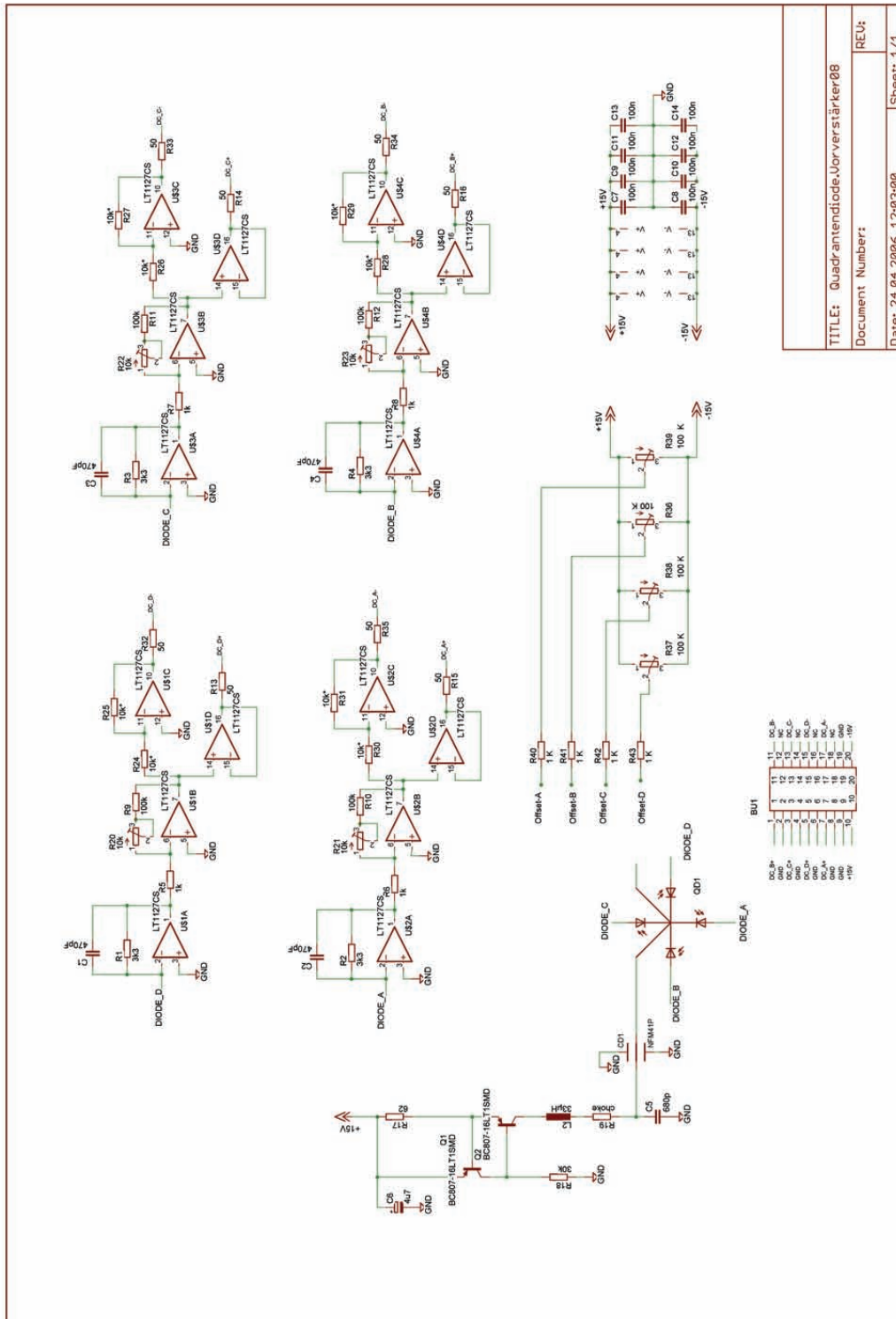


Figure B.1.: Labeling of the individual quadrants (view from front).

The first signal is taken for the translation measurement, signals 2 to 5 for differential wavefront sensing and signals 6 and 7 for adjustment of the photodiode (the signals are zero in case of a beam centered on the quadrant photodiode).

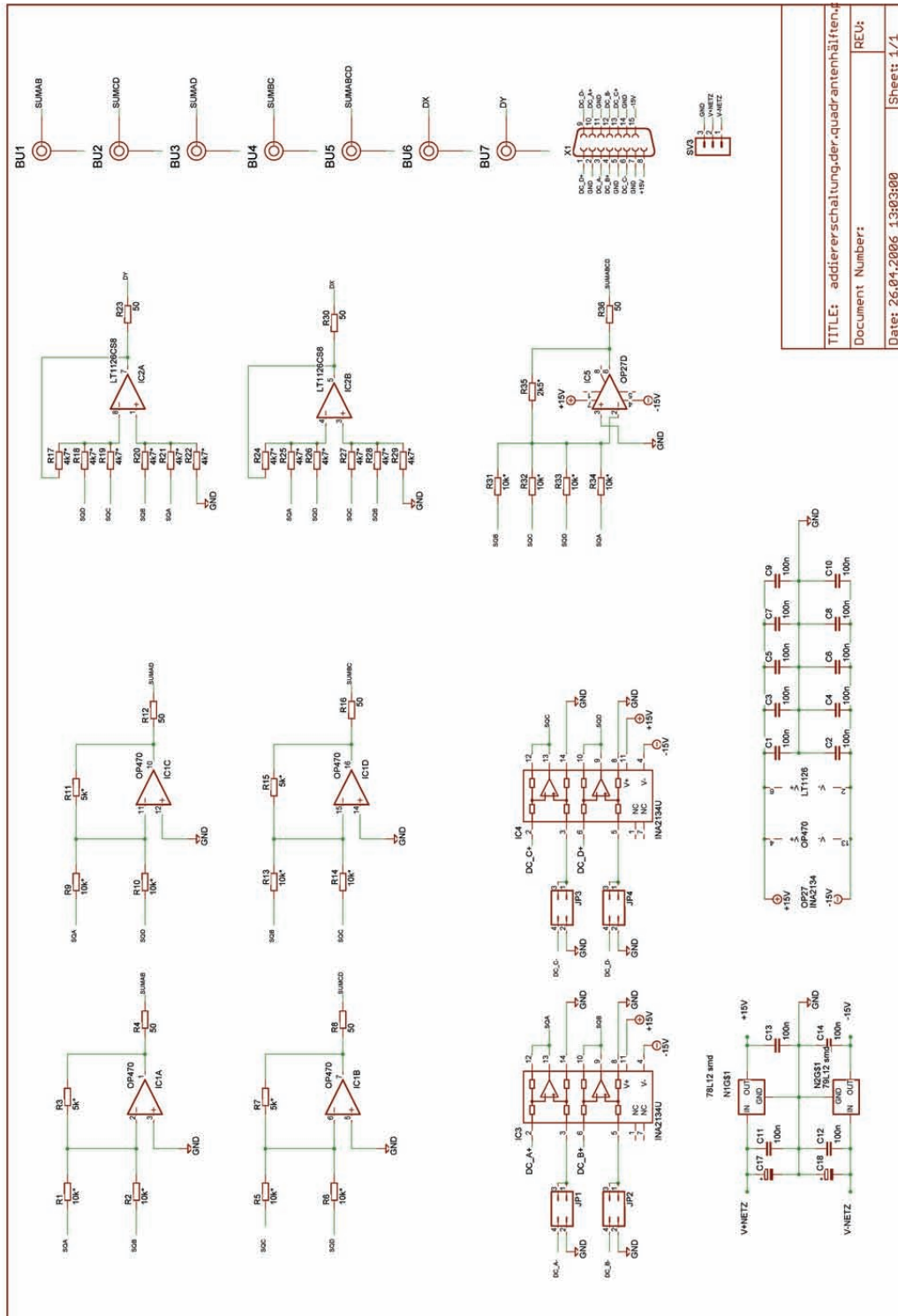
B.2. PID-Servo Loop

The schematic of the multi-purpose PID-servo loop as it is used for the phaselock as detailed in chapter 6.4 and for intensity stabilization (cf. chapter 6.3) is shown in Fig. B.6. For our applications, both control loops are realized as PI servo loops.



TITLE: Quadrantdiode-Vorverstärker08	REV:
Document Number:	Sheet: 1/1
Datet: 24.04.2006 12:03:00	

Figure B.2.: Schematic of the quadrant diode preamplifier.



TITLE: addierschaltung-der-quadrantenhäufung	REV:
Document Number:	
Date: 26.04.2006 13:03:00	Sheet: 1/1

Figure B.3.: Schematic of the quadrant diode summing board.



Figure B.4.: Photograph of the SMD quadrant photodiode electronics developed for the second experimental setup. The windows of the quadrant photodiodes were removed for the measurements.

B.3. 6th Order Lowpass

For anti-aliasing, we designed a 6th order Bessel low pass filter. The schematic is shown in Fig. B.7 and represents a multi-purpose board for filters up to the 6th order. The filter has a differential input by use of the unity gain differential amplifier INA105. The specific values for a 2 Hz low pass used in our first experiment is given in Fig. B.5.

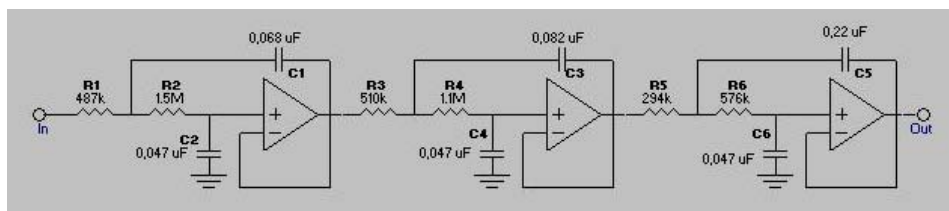


Figure B.5.: Schematic of the 2 Hz anti-aliasing filter (Bessel, 6th order) used in our first experimental setup. The filter design was performed using the freeware FilterLab software provided by Microchip.

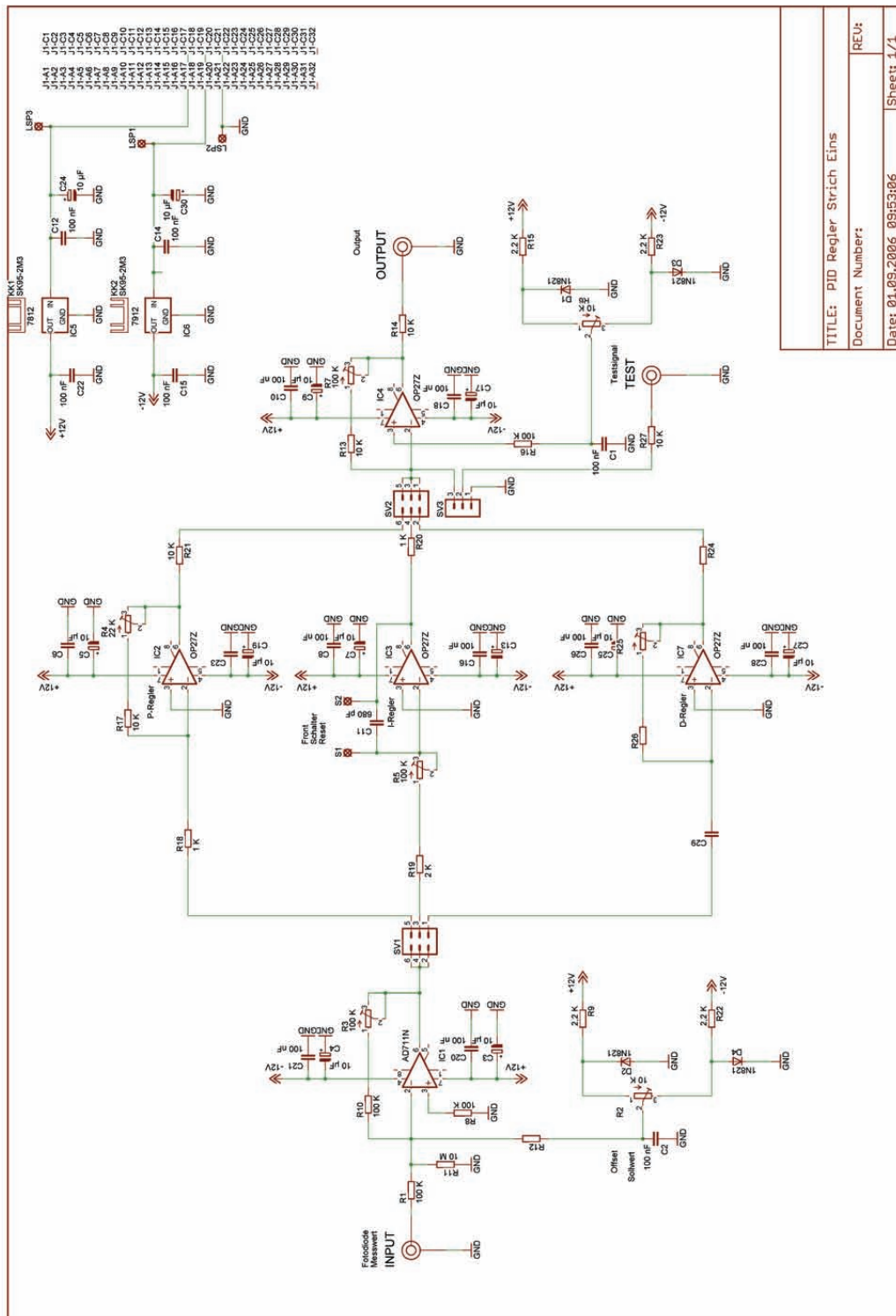


Figure B.6.: Schematic of the PID servo loop.

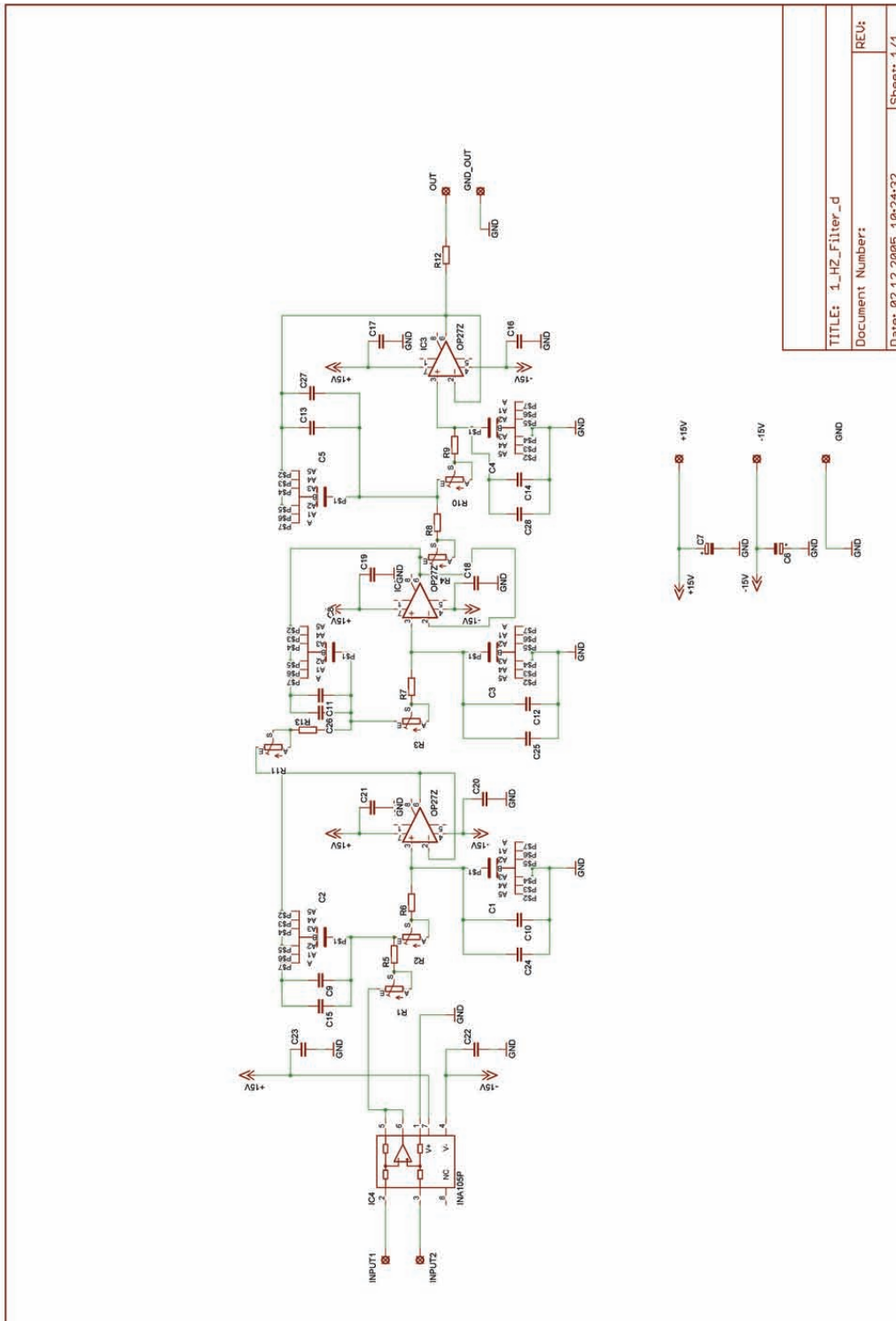


Figure B.7.: Schematic of the anti-aliasing filter.

TITLE: 1_HZ_Filter_d	REU:
Document Number:	
Date: 02.12.2005 10:24:32	Sheet: 1/1

C. LabVIEW Programs

The data acquisition (DAQ) and post-processing was carried out by the graphical programming software LabVIEW by National Instruments in combination with data acquisition computer boards. The specifications of the two DAQ boards used in our experiments are given in Table C.1 where the sampling rate of the NI-PCI-6229 board is in our case limited by the speed of the host computer. For quasi real-time programs only sampling rates up to a few hundred Hertz are possible.

C.1. First Interferometer Setup

In our first setup we used the NI-PCI-6229 data acquisition board. The generation of the in-quadrature measurement is carried out utilizing analog electronics. The output signals of the (analog) mixers were anti-aliasing filtered (with a 2 Hz cut-off frequency) and digitized with a sample rate of 20 Hz. Also other parameters as room temperature, temperature of the interferometer board and voltages at the monitor photodiodes after fiber-outcoupling in the vacuum chamber were recorded. The LabVIEW program for data post-processing is shown in Fig. C.1.

Six signals from the quadrant diodes are input signals to the DAQ board: the sum signal of QPD1 (measurement photodiode) and the sum signal of QPD2 (reference photodiode) for translation measurement; the individual quadrants of QPD1 for tilt measurement. For clarity reasons, the input signals for the tilt measurement and its calculation are not included in the program shown in Fig. C.1. The post-processing

	NI-PCI-6229	NI-PCI-7833R
number of channels	32SE / 16DI	16SE / 8DI
max. sampling rate	250kS/s	200kS/s
AD resolution	16 bit	16 bit
simultaneous sampling	no	yes
input voltage	± 10 V	± 10 V

Table C.1.: Specifications of the two DAQ computer boards used in the experiments (SE: single ended; DI: differential).

procedure is the same for all three signal pairs. The monitoring of π -phasejumps in the arctan-calculation is carried out by two ‘for’ loops, cf. Fig. C.2. The calculated translation and tilt (converted to nm and nrad, respectively) is written to a data file.

C.2. Second Interferometer Setup

In our second setup we implemented a digital phase measurement and utilized an additional FPGA (Field Programmable Gate Array) data acquisition board for simultaneously digitizing signals with a rate up to 200 kS/s. The FPGA board can be programmed by the LabVIEW FPGA module which afterwards compiles the program to VHDL code. Therefore, it is necessary to create a LabVIEW project which includes the LabVIEW program running on the FPGA and the so-called host program which runs on the computer CPU. In our case, also a FIFO (first in first out) memory block for data exchange between FPGA and the host computer is included in the project’s structure.

The FPGA program is shown in Fig. C.3. The sequence inside the while loop is repeated with the given sampling rate. In our case, the input signals AI0 to AI5 (at the heterodyne frequency of 10 kHz) are digitized with a sampling rate of 160 kHz. The signals AI0 and AI1 are the sum signals of QPD1 and QPD2 used for the translation measurement, the signals AI2 to AI5 are the summed halves A+B, C+D, A+C, B+D of QPD1 used for the tilt measurements. For in-quadrature measurement, each signal is split. Before multiplication, one signal is phase shifted by 90° by adding a delay of 4 iterations of the while loop to one signal. After multiplication, the signals are filtered by use of a Butterworth 4th order low pass filter with a corner frequency of 4 Hz. The signals are merged to an array and transferred to the FIFO. For data reduction, only every n-th value is transferred (given by the value of ‘Faktor fuer Datenreduktion’, in our measurements mostly 8000). The single-cycle timed loop in the lower part of Fig. C.3 generates a 20 MHz square wave signal which is used for synchronizing the DDS and the FPGA on-board clock. The data of the FIFO is read out in the LabVIEW host program as shown in Fig. C.4. Similar to the calculation in our first experimental setup (cf. Fig. C.1), the program calculates the translation and tilts and monitors π -phasejumps in the arc tangent. Also room temperature, the monitor photodiode signals and other parameters for diagnostics are recorded by use of the M-Series DAQ board (lower part in Fig. C.4). The data is written to a file.

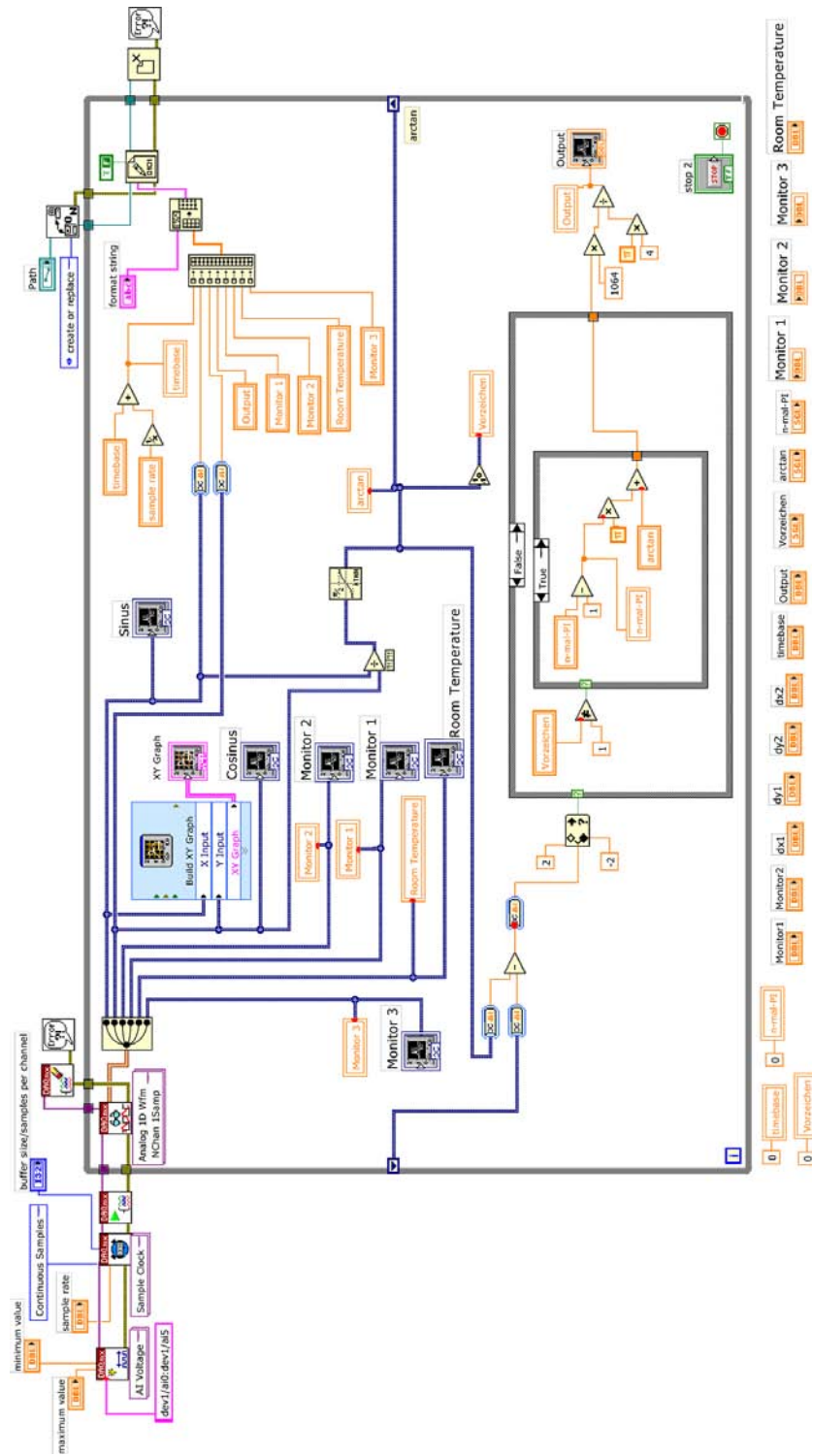


Figure C.1.: LabView program for calculating the translation.

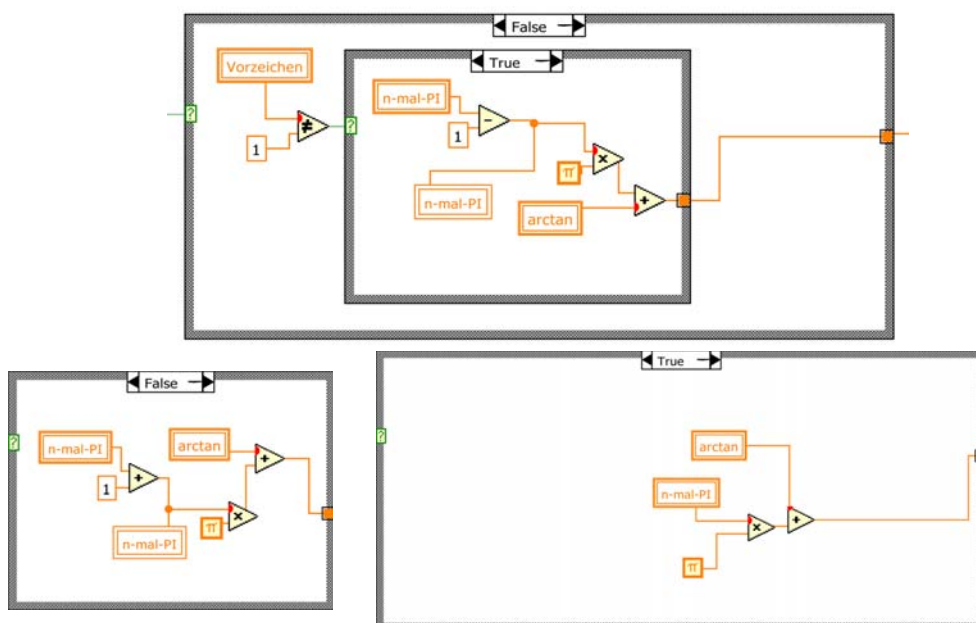


Figure C.2.: The other ‘for’-cases in the LabVIEW program shown in Fig.C.1. They are monitoring π -phasejumps in the arctan calculation of the translation.

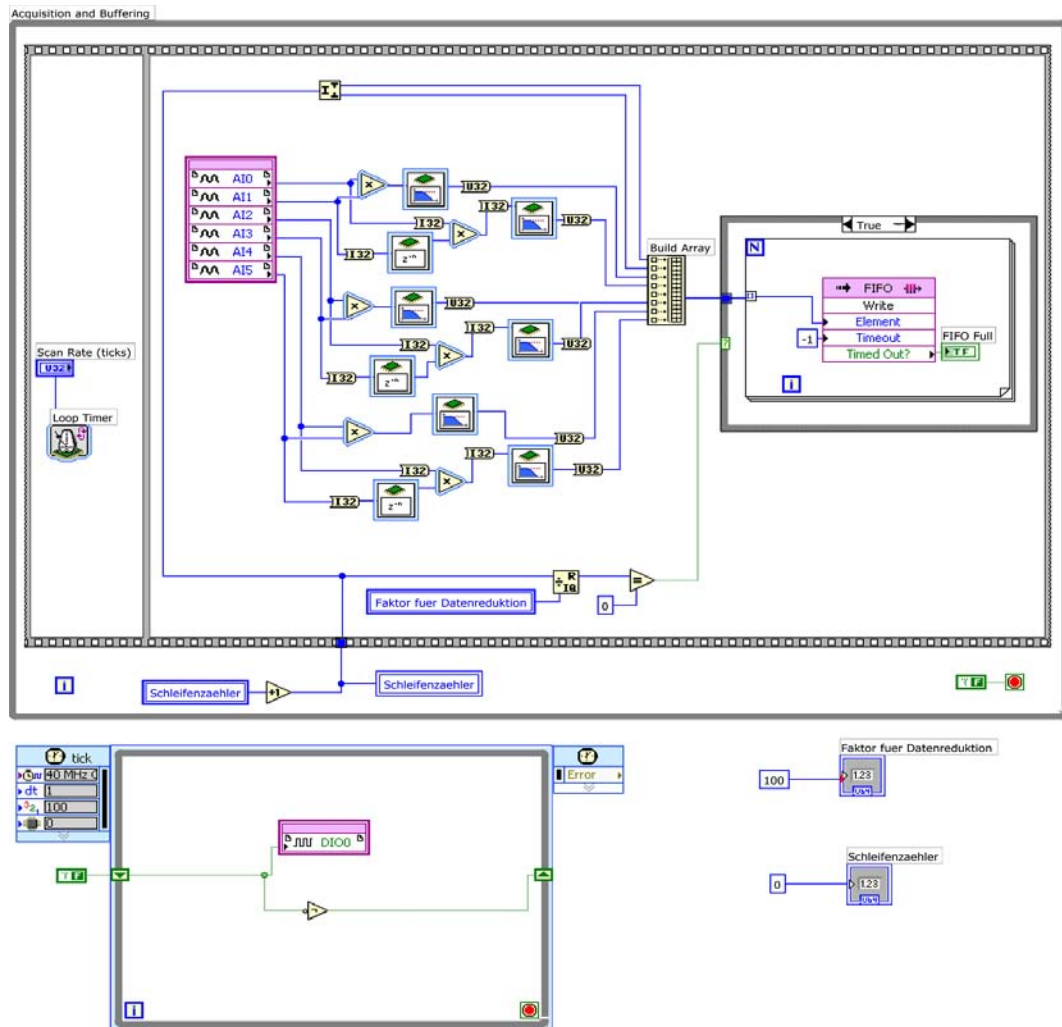


Figure C.3.: LabView program running on the FPGA. The 'false' loop is just empty.

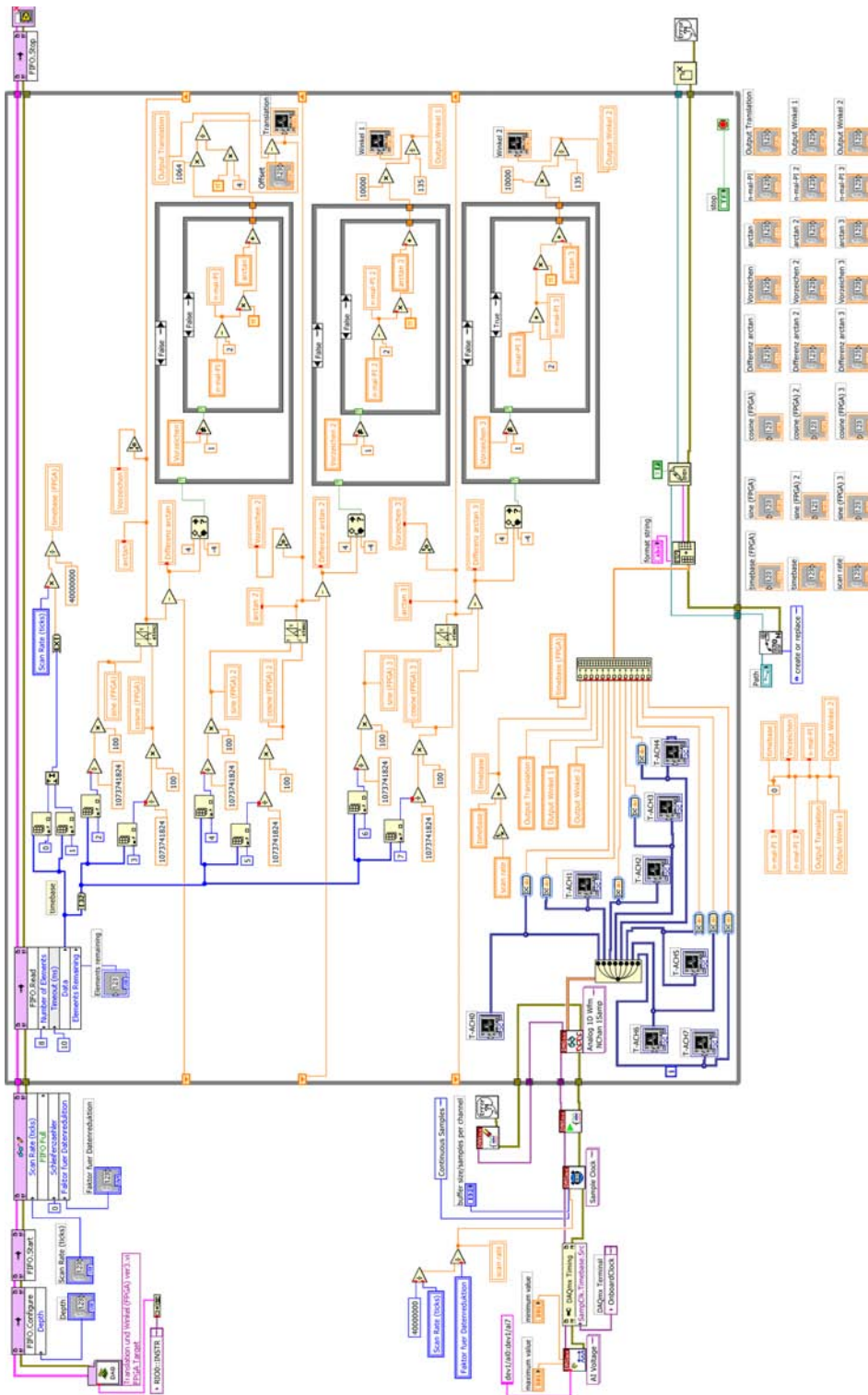


Figure C.4.: LabVIEW host program running on the main CPU.

D. Calculation of the Power Spectrum Density

The calculation of the power spectral density throughout this thesis is based on a recommendation by the LISA and LISA Pathfinder teams [122] and a corresponding Matlab m-file [123].

The power spectral density (PSD) is defined as

$$S_{x,x}(f) = 2 \int_{-\infty}^{\infty} \langle x(t)x(t+\tau) \rangle e^{-i2\pi f\tau} d\tau \quad (\text{D.1})$$

where $x(t)$ is the measured signal and the square brackets represent the average value. Hence, the PSD represents the Fourier transform of the autocorrelation of $x(t)$.

The square root of Equation D.1 is called linear spectral density $s_{x,x}$ with the unit $1/\sqrt{\text{Hz}}$:

$$s_{x,x} = \sqrt{S_{x,x}}. \quad (\text{D.2})$$

The rms-value¹ Δs_{rms} is obtained by integration of $s_{x,x}$ over a frequency interval Δf :

$$\begin{aligned} \Delta s_{rms} &= \left[\int_f^{f+\Delta f} df \cdot S_{x,x}(f) \right]^{1/2} \\ &\approx [S_{x,x}(f) \cdot \Delta f]^{1/2} \\ &\approx s_{x,x}(f) \cdot \sqrt{\Delta f}. \end{aligned} \quad (\text{D.3})$$

For a discrete time series $x(n) = x(t = n \cdot \Delta t)$, where n is an integer and Δt is the

¹A spectrum analyzer measures this rms-value in a frequency band Δf (called ‘resolution bandwidth’, RBW). The linear spectral density is obtained by dividing the rms-value by the square root of the measurement bandwidth RBW.

sampling time, the Discrete Fourier Transform (DFT) is defined as

$$x(k) = \frac{1}{\sqrt{N_d}} \sum_{n=1}^{N_d} x(n) e^{-i \frac{2\pi}{N_d} k(n-1)}, \quad (\text{D.4})$$

where N_d is the number of points of $x(n)$. The calculation of the PSD as given in Ref. [122] is based on the Welch PSD estimate:

$$P_{x,x}[k] = \frac{2\Delta t}{N_w} \sum_{l=1}^{N_w} \left| \frac{1}{\sqrt{N_d}} \sum_{n=1}^{N_d} w(n) x^l(n) e^{-i \frac{2\pi}{N_d} k(n-1)} \right|^2. \quad (\text{D.5})$$

Here, the time series $x(n)$ is divided in N_w segments with N_d data and a certain overlap. Δt is the sampling time and $w(n)$ is the spectral window which is normalized as

$$\frac{1}{N_d} \sum_{n=1}^{N_d} |w(n)|^2 = 1. \quad (\text{D.6})$$

$P_{x,x}[k]$ is an estimator for the PSD of the measured signal $x(n)$ at the frequency $f = k/(N_d\Delta t)$.

For our calculation, the data is divided into 9 segments with 50% overlap and a blackmanharris window is applied.

For removing long term drifts from the data, de-trending of the data is carried out. Therefore, a polynomial of time $c_1 \cdot t + c_0$ is fitted to the data and subtracted before PSD calculation. The de-trending is applied to each single segment of the time series individually.

E. Frequency Stabilized Nd:YAG Laser

The laser used as light source for our interferometer could be optionally frequency stabilized to a transition in molecular Iodine. The Nd:YAG laser at 1064 nm is therefore doubled in frequency and a setup for doppler-free spectroscopy of Iodine is realized [107, 108, 124, 125, 126]. The method of Modulation Transfer Spectroscopy (MTS) is utilized due to enhanced long-term stability compared to Frequency Modulation Spectroscopy (FMS). A photograph of the setup is shown in Fig. E.1. With a similar but compact setup using a 10 cm long Iodine cell, a frequency stability (Root-Allen-Variance) below $3 \cdot 10^{-13}$ for integration times $\tau > 100$ s was achieved [107].

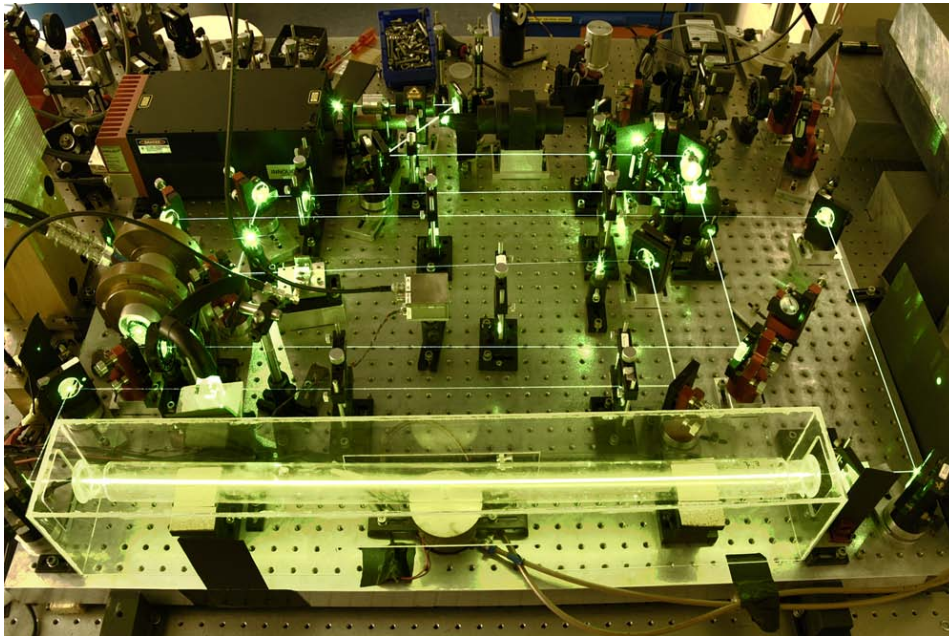


Figure E.1.: Photograph of the Iodine stabilized Nd:YAG laser. At the front, one can see the fluorescent 80 cm long Iodine cell.

F. Alternative Laser Source

DBR (distributed Bragg reflector) laser diodes are a promising alternative to the Nd:YAG solid-state lasers used in our experiments. These laser diodes offer relatively narrow linewidths and a high frequency and intensity stability. Compared to the NPRO type Nd:YAG laser, they have lower mass, lower power consumption and a less complex optical setup which all are relevant parameters for its application, both in space science and industrial environment.

For their future application, the characterization of the laser diodes with respect to linewidth, frequency and intensity stability, and also modulation bandwidth is essential. The determination of the laser linewidth also determines the feasibility of phase-locking of two DBR diode lasers. In the following, we give a short introduction to DBR lasers, detail the developed fiber-coupled laser module and show first preliminary measurements.

F.1. DBR Laser Diodes

Fig. F.1 shows the schematic of a three-section DBR laser diode. It is a semiconductor laser based on a Gallium Arsenide (GaAs) hetero-structure and consists of an active gain section, a passive phase section and a DBR section (Bragg section). The diodes used in our experiments are provided by the ‘Ferdinand Braun Institut für Höchstfrequenztechnik (FBH)’ in Berlin and have a total length of $2000 \mu\text{m}$, where the gain section has a length of $1000 \mu\text{m}$, the phase section a length of $300 \mu\text{m}$ and the Bragg section a length of $700 \mu\text{m}$. In the Bragg section the refractive index in propagation direction is periodically varied resulting in a frequency selective reflector causing only one longitudinal laser mode to be amplified (single-mode laser).

The Bragg and phase sections of the laser diode have a heating resistance on the top layer ($R= 5.9 \Omega$). By applying currents, the frequency of the laser radiation can be varied (and also modulated). The length of the laser resonator, and in case of the Bragg section also the frequency selective period length of the grating, is depending on the temperature of the DBR laser [127, 128]:

$$l_P = l_{P0} \cdot (1 + \varepsilon_l \cdot [T_P - T_0])$$
$$\Lambda_B = \Lambda_{B0} \cdot (1 + \varepsilon_l \cdot [T_B - T_0])$$

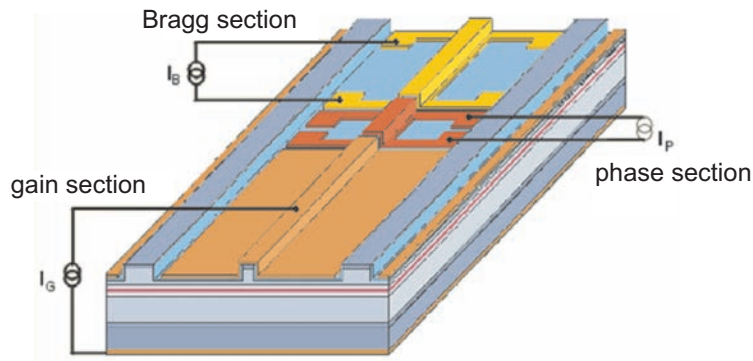


Figure F.1.: Three section DBR laser diode (source: Ferdinand Braun Institut Berlin).

with:

l_P = phase section length

l_{P0} = initial phase section length

ϵ_l = linear thermal expansion coefficient

T_P = phase section temperature

T_0 = initial temperature

Λ_B = period length of the Bragg reflector in the Bragg section

Λ_{B0} = initial period length in the Bragg section

T_B = Bragg section temperature

The initial temperature is the same for all sections. The refractive indexes of the phase section n_P and the Bragg section n_B are also changed:

$$n_P = n_{GaAs} \cdot (1 + \epsilon_n \cdot [T_P - T_0])$$

$$n_B = n_{GaAs} \cdot (1 + \epsilon_n \cdot [T_B - T_0])$$

with ϵ_n the temperature coefficient of the refractive index change and n_{GaAs} the refractive index of GaAs. A comparison of the coefficients ($\epsilon_n \approx 100 \cdot 10^{-6} \text{ K}^{-1}$ and $\epsilon_l \approx 6 \cdot 10^{-6} \text{ K}^{-1}$, cf. [127]) reveals, that the change in refractive index is the dominating effect.

A small tuning range of the laser frequency is realized by only heating the Bragg section of the DBR diode. For larger (mod-hop free) operation, it is necessary

to control both, Bragg and phase section of the laser diode, simultaneously in an appropriate way.

F.2. Laser Module

For a first characterization of the DBR laser diodes, a fiber-coupled laser module made of aluminum was developed. It includes the laser diode, a collimating lens (focal length: 1.2 mm), a two-stage optical isolator (Linos, model FI-1040-TI, with an isolation > 60 dB) and a fiber coupler (Schäfter und Kirchhoff, model 60SMS). The laser diode is mounted on a temperature stabilized copper plate for stable operation where a Pt-100 temperature sensor is used for temperature measurement (≈ 10 mK stability). Peltier elements are used for heat supply; they are mounted between the copper plate and the aluminum support. A low-noise current controller based on the design given in [129] is used. A photograph of the laser module with corresponding schematic is shown in Fig. F.2.

F.3. First Characterization

For a beat measurement, we set up two identical laser modules. The laser chips are placed in a TO3 package where only the gain sections are connected. The DBR laser diodes have a wavelength of 1063.29 nm and 1063.30 nm, respectively. The threshold current is 25 mA and the maximum current is 230 mA.

In a first test, the laser diode temperature was varied between 15°C and 40°C, showing a mod-hop free linear correlation with a coefficient of about 23 GHz/K. The frequency was measured using a commercial wavelength meter (Toptica, model WS-6). In a second test, the laser diode temperature was stabilized at 35°C and the laser current was varied. Using a beat configuration of the DBR laser and an iodine stabilized Nd:YAG laser as reference (cf. the schematic shown in Fig. F.3 and appendix E), a linear frequency response with a coefficient of approximately 476 MHz/mA was measured.

Using the beat setup in combination with a spectrum analyzer (Agilent, model N9320A), an upper limit for the laser linewidth was obtained: < 1 MHz (average over 10 measurement with a total time of 204 ms).

The presented measurements are a first step in characterizing the DBR laser diodes. In future work, the linewidth measurement method will be improved, the current measurement of 1 MHz states an upper limit. Also, it is necessary to have individual control of every single section of the diode. Using a separate current controller for each section, the whole tuning capability of the laser diodes can be analyzed. The DBR laser as detailed above is integrated in the interferometer setup for optical profilometry described in chapter 7.2.

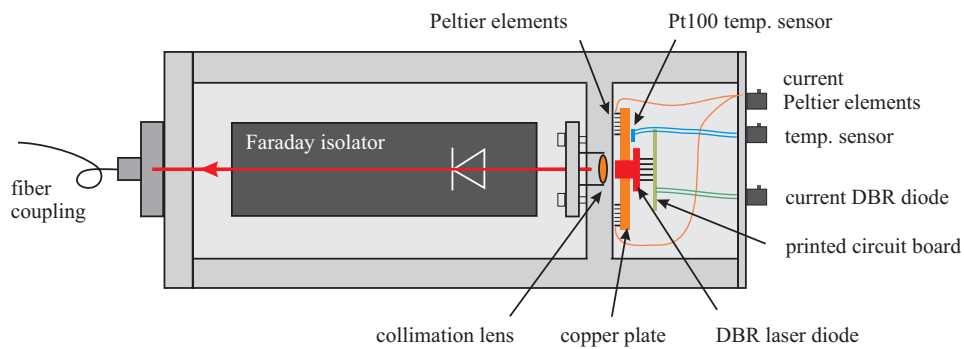
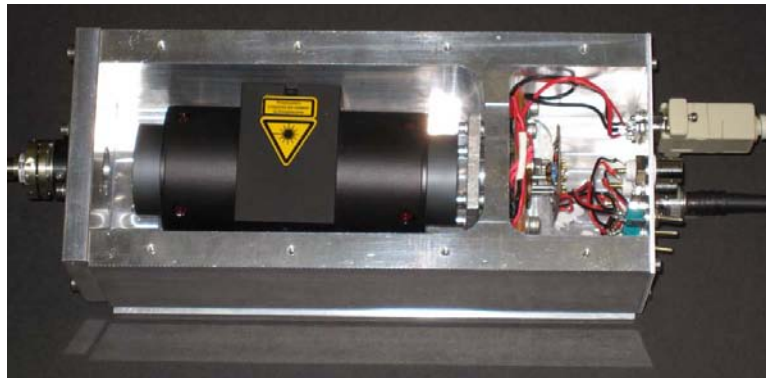


Figure F.2.: Top: Photograph of the DBR laser modul with integrated laser diode, collimation lens, optical isolator and fiber coupling. It has a total length of 23 cm. Bottom: Schematic of the DBR laser module.

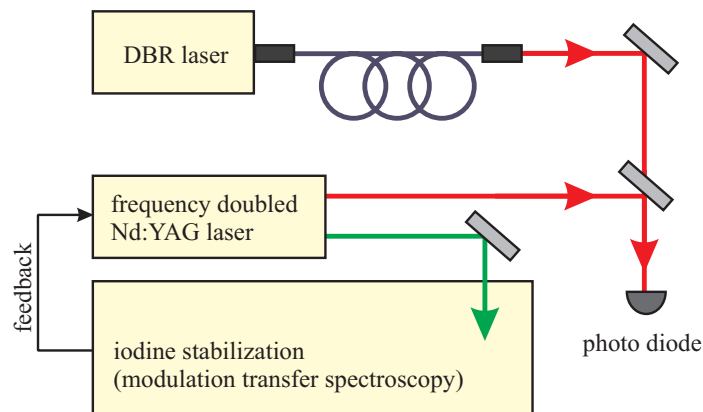


Figure F.3.: Schematic of the beat measurement. The light of the DBR laser diode is superimposed with the light from a frequency stabilized Nd:YAG laser on a fast photo diode.

Bibliography

- [1] C. Misner, K. Thorne, and J. Wheeler. *Gravitation*. Freeman, 2000.
- [2] S. Brozek. *Frequenzstabilisierung eines Nd:YAG-Hochleistungs-Laser-Systems für den Gravitationswellendetektor GEO 600*. PhD thesis, Universität Hannover, 1999.
- [3] LISA study team. LISA – Laser Interferometer Space Antenna; Pre-Phase A Report, 1998.
- [4] C. Ungarelli, P. Corasaniti, R. A. Merder, and A. Vecchio. Gravitational waves, inflation and the cosmic microwave background: towards testing the slow-roll paradigm. *Class. Quantum Grav.*, 22:S955–S963, 2005.
- [5] A. Abramovici, P. Bender, R. Drever, L. S. Finn, R. Flaminio, L. Grishchuk, W. Johnson, K. Kawabe, P. Michelson, N. Robertson, A. Rüdiger, R. J. Sandeman, P. Saulson, D. Shoemaker, Thorne K., M. Tinto, M. Tobar, R. Weiss, and S. Whitcomb. Gravitational wave astrophysics. In E. W. Kolb and R. Peccei, editors, *Particle and Nuclear Astrophysics and Cosmology in the Next Millenium: Proceedings of the 1994 Snowmass Summer Study*, pages 398–425, Singapore, 1995. World Scientific Publishing Co.
- [6] F. Ricci and A. Brilliet. A review of gravitational wave detectors. *Annu. Rev. Nucl. Part. Sci.*, 47:111–156, 1997.
- [7] G. A. Prodi and et al. The Ultracryogenic Gravitational Wave Detector AU-RIGA. In E. Coccia, G. Veneziano, and G. Pizzella, editors, *Second Edoardo Amaldi Conference on Gravitational Wave Experiments*, pages 166–+, 1998.
- [8] LISA-LIST team. LISA: Probing the universe with gravitational waves. Technical report, LISA Mission Science Office, 2007.
- [9] R. A. Hulse and J. H. Taylor. Discovery of a pulsar in a binary system. *Astrophys. J.*, 195:L51–L53, 1975.
- [10] J. H. Taylor and J. M. Weisberg. A new Test of General Relativity: Gravitational Radiation and the Binary Pulsar PSR 1913+16. *Astrophys. J.*, 253: 908–920, 1982.

- [11] Russell A. Hulse. The discovery of the binary pulsar. *Rev. Mod. Phys.*, 66(3):699–710, 1994.
- [12] J. Taylor. Binary pulsars and relativistic gravity. *Rev. Mod. Phys.*, 66(3):711–719, 1994.
- [13] J. Weber. Detection and generation of gravitational waves. *Phys. Rev.*, 117(1):306–313, Jan 1960.
- [14] Z. K. Geng, W. O. Hamilton, W. W. Johnson, E. Mauceli, S. M. Merkowitz, A. Morse, and N. Solomonson. Operation of the ALLEGRO detector at LSU. In E. Coccia, G. Pizzella, and F. Ronga, editors, *First Edoardo Amaldi Conference on Gravitational Wave Experiments*, Singapore, 1995. World Scientific Publishing Co.
- [15] P. Bonifazi and M. Visco. The ALTAIR cryogenic gravitational-wave experiment. *Il Nuovo Cimento C*, 15(6):943–954, 1992.
- [16] P. Astone, M. Bassan, P. Bonifazi, P. Carelli, M. G. Castellano, G. Cavallari, E. Coccia, C. Cosmelli, V. Fafone, S. Frasca, E. Majorana, I. Modena, G. V. Pallottino, G. Pizzella, P. Rapagnani, F. Ricci, and M. Visco. Long-term operation of the rome "explorer" cryogenic gravitational wave detector. *Phys. Rev. D*, 47(2):362–375, Jan 1993.
- [17] P. Astone, D. Babusci, M. Bassan, P. Bonifazi, E. Coccia, S. D'Antonio, V. Fafone, G. Giordano, A. Marini, Y. Minenkov, I. Modena, G. Modestino, A. Moleti, G. V. Pallottino, G. Pizzella, L. Quintieri, A. Rocchi, F. Ronga, R. Terenzi, and M. Visco. The next science run of the gravitational wave detector NAUTILUS. *Class. Quant. Grav.*, 19:1911–1917, 2002.
- [18] D. G. Blair, E. N. Ivanov, M. E. Tobar, P. J. Turner, F. van Kann, and I. S. Heng. High sensitivity gravitational wave antenna with parametric transducer readout. *Phys. Rev. Lett.*, 74(11):1908–1911, 1995.
- [19] Scott A. Hughes and Kip S. Thorne. Seismic gravity-gradient noise in interferometric gravitational-wave detectors. *Phys. Rev. D*, 58(12):122002, 1998.
- [20] Kip S. Thorne and Carolee J. Winstein. Human gravity-gradient noise in interferometric gravitational-wave detectors. *Phys. Rev. D*, 60(8):082001, 1999.
- [21] <http://www.esa.int/science/lisa>, (last access: september 2010).
- [22] <http://lisa.nasa.gov>, (last access: september 2010).

- [23] S. Rowan and J. Hough. Gravitational wave detection by interferometry (ground and space). *Living Rev. Relativity*, 3, 2000.
- [24] N. A. Robertson. Laser interferometric gravitational wave detectors. *Class. Quant. Grav.*, 197:R19–R40, 2000.
- [25] W. M. Folkner, P. L. Bender, and R. T. Stebbins. LISA mission concept study. *Jet Propulsion Laboratory*, 1998.
- [26] Astrium. LISA – study of the Laser Interferometer Space Antenna; final technical report, 2000.
- [27] A. Hammersfahr. LISA mission study overview. *Class. Quant. Grav.*, 18: 4045–4051, 2001.
- [28] LISA Sensitivity Curve Generator available at <http://www.srl.caltech.edu/~shane/sensitivity/MakeCurve.html>, (last access: september 2010).
- [29] P. W. McNamara. Weak-light phase locking for LISA. *Class. Quantum Grav.*, 22:S243–S247, 2005.
- [30] B. S. Sheard, M. B. Gray, D. E. McClelland, and D. A. Shaddock. Laser frequency stabilization by locking to a LISA arm. *Phys. Lett. A*, 320(1): 9–21, 2003.
- [31] B. S. Sheard, M. B. Gray, D. A. Shaddock, and D. E. McClelland. Laser frequency noise suppression by arm-locking in LISA: progress towards a bench-top demonstration. *Class. Quantum Grav.*, 22:S221–S226, 2005.
- [32] M. Tinto, F. B. Estabrook, and J. W. Armstrong. Time-delay interferometry for LISA. *Phys. Rev. D*, 65:082003–1–12, 2002.
- [33] M. Tinto and S. V. Dhurandhar. Time-delay interferometry. *Living Rev. Relativity*, 8, 2005.
- [34] D. Weise, C. Braxmaier, M. Kersten, W. Holota, and U. Johann. Optical Design of the LISA Interferometric Metrology System. In *Proceedings of the 6th International LISA Symposium*, volume 873, pages 389–394, AIP conference proceedings, 2006.
- [35] M. Sallusti, P. Gath, D. Weise, M. Berger, and H. R. Schulte. LISA system design highlights. *Class. Quantum Grav.*, 26:094015, 2009.
- [36] S. Anza *et al.* The LTP experiment on the LISA pathfinder mission. *Class. Quantum Grav.*, 22:S125–S138, 2005.

- [37] <http://www.esa.int/science/lisapathfinder>, (last access: september 2010).
- [38] E. J. Ellife, J. Bogenstahl, A. Deshpande, J. Hough, C. Killow, S. Reid, D. Robertson, S. Rowan, H. Ward, and G. Cagnoli. Hydroxide-catalysis bonding for stable optical systems for space. *Class. Quantum Grav.*, 22: S257–S267, 2005.
- [39] T. Kane and R. Byer. Monolithic, unidirectional single-mode Nd:YAG ring laser. *Opt. Lett.*, 10:65–67, 1985.
- [40] D. B. DeBra. Drag-free spacecraft as platforms for space missions and fundamental physics. *Class. Quantum Grav.*, 14:1549–1555, 1997.
- [41] B. Lange. Drag-free performance in a LISA mission with spherical proof masses. *Class. Quantum Grav.*, 19:1739–1743, 2002.
- [42] U. Johann, P. Gath, W. Holota, H. R. Schulte, and D. Weise. Novel payload architectures for LISA. In *Proceedings of the 6th International LISA Symposium*, volume 873, pages 304–311, AIP conference proceedings, 2006.
- [43] W. J. Weber, A. Cavalleri, R. Dolesi, G. Fontana, M. Hueller, and S. Vitale. Position sensors for LISA drag-free control. *Class. Quantum Grav.*, 19: 1751–1756, 2002.
- [44] L. Carbone, A. Cavalleri, G. Ciani, R. Dolesi, M. Hueller, D. Tombolato, S. Vitale, and W.J. Weber. Upper limits to surface force disturbances on LISA proof-masses and the possibility of observing galactic binaries. *Phys. Rev. D*, 75:042001, 2007.
- [45] A. Cavalleri, R. Dolesi, G. Fontana, M. Hueller, J. Turneaure, S. Vitale, and W. Weber. Progress in the development of a position sensor for LISA drag-free control. *Class. Quant. Grav.*, 18:4133–4144, 2001.
- [46] LISA: System and technology study report, 2000.
- [47] H. J. Paik. Superconducting tunable diaphragm transducer for sensitive acceleration measurements. *J. Appl. Phys.*, 47:1168–1178, 1976.
- [48] S. Zarembinski. On superconductive gravity gradiometry in space. *Space Science Reviews*, 00:1–10, 2003.
- [49] H. A. Chan and H. J. Paik. Superconducting gravity gradiometer for sensitive gravity measurements. I. Theory. *Phys. Rev. D*, 35(12):3551–3571, 1987.

- [50] M. V. Moody, H. J. Paik, and E. R. Canavan. Three-axis superconducting gravity gradiometer for sensitive gravity experiments. *Rev. Sci. Instr.*, 73(11):3957–3974, 2002.
- [51] E. Morrison, B. J. Meers, D. I. Robertson, and H. Ward. Automatic alignment of optical interferometers. *Appl. Opt.*, 33(22):5041–5049, 1994.
- [52] E. Morrison, B. J. Meers, D. I. Robertson, and H. Ward. Experimental demonstration of an automatic alignment system for optical interferometers. *Appl. Opt.*, 33(22):5037–5040, 1994.
- [53] F. Acernese, E. Calloni, R. De Rosa, L. Di Fiore, and L. Milano. An optical readout system for the drag-free control of LISA. *Class. Quantum Grav.*, 22:S279–S285, 2005.
- [54] A. La Rana. *An Optical ReadOut for the Gravitational Reference Sensor of LISA*. phd-thesis, University of Napoli Federico II, 2007.
- [55] C.C. Speake and S.M. Aston. An interferometric sensor for satellite drag-free control. *Class. Quantum Grav.*, 22:S269–S277, 2005.
- [56] S. M. Aston and C. C. Speake. An interferometric based optical read-out scheme for the LISA proof-mass. In *Proceedings of the 6th International LISA Symposium*, volume 873, pages 326–333, AIP conference proceedings, 2006.
- [57] K.-X. Sun, G. Allen, S. Buchman, D. DeBra, and R. Byer. Advanced gravitational reference sensor for high precision space interferometers. *Class. Quantum Grav.*, 22:S287–S296, 2005.
- [58] K.-X. Sun, U. Johann, D. B. DeBra, S. Buchman, and R. L. Byer. LISA gravitational reference sensors. In *Proceedings of the TeV Particle Astrophysics II Workshop*, volume 60, pages 272–275, Journal of Physics: Conference Series, 2007.
- [59] K.-X. Sun, S. Buchman, R. Byer, D. DeBra, J. Goebel, G. Allen, J. W. Conklin, D. Gerardi, S. Higuchi, N. Leindecker, P. Lu, A. Swank, E. Torres, and M. Trittler. Modular Gravitational Reference Sensor Development. In *Proceedings of the 7th International LISA Symposium*, volume 154, page 012026, Journal of Physics: Conference Series, 2009.
- [60] G. Heinzl, C. Braxmaier, R. Schilling, A. Rüdiger, D. Robertson, M. te Plate, V. Wand, K. Arai, U. Johann, and K. Danzmann. Interferometry for the LISA technology package (LTP) aboard SMART-2. *Class. Quantum Grav.*, 20:S153–S161, 2003.

- [61] G. Heinzel, V. Wand, A. Garcia, O. Jennrich, C. Braxmaier, D. Robertson, K. Middleton, D. Hoyland, A. Rüdiger, R. Schilling, U. Johann, and K. Danzmann. The LTP interferometer and phasemeter. *Class. Quantum Grav.*, 21:S581–S587, 2004.
- [62] G. Heinzel, C. Braxmaier, M. Caldwell, K. Danzmann, F. Draaisma, A. Garcia, J. Hough, O. Jennrich, U. Johann, C. Killow, K. Middleton, M. te Plate, D. Robertson, A. Rüdiger, R. Schilling, F. Steier, V. Wand, and H. Ward. Successful testing of the LISA technology package (LTP) interferometer engineering model. *Class. Quantum Grav.*, 22:1–6, 2005.
- [63] V. Wand, J. Bogenstahl, C. Braxmaier, K. Danzmann, A. Garcia, F. Guzman, G. Heinzel, J. Hough, O. Jennrich, C. Killow, D. Robertson, Z. Sodnik, F. Steier, and H. Ward. Noise sources in the LTP heterodyne interferometer. *Class. Quantum Grav.*, 23:S159–S167, 2006.
- [64] R. C. Quenelle. Nonlinearity in interferometer measurements. *Hewlett-Packard Journal*, 34(4):10, 1983.
- [65] C. M. Sutton. Non-linearity in length measurement using heterodyne laser Michelson interferometry. *J. Phys. E: Sci. Instrum.*, 20(10):1290–1292, 1987.
- [66] N. Bobroff. Residual errors in laser interferometry from air turbulence and nonlinearity. *Appl. Opt.*, 26(13):2676–2682, 1987.
- [67] W. Augustyn and P. Davis. An analysis of polarization mixing errors in distance measuring interferometers. *J. Vac. Sci. Technol.*, 8(6):2032–2036, 1990.
- [68] A.E. Rosenbluth and N. Bobroff. Optical sources of nonlinearity in heterodyne interferometers. *Precision Eng.*, 12(1):7–11, 1990.
- [69] J.M. De Freitas and M.A. Player. Polarization effects in heterodyne interferometry. *J. Mod. Opt.*, 42(9):1875–1899, 1995.
- [70] B.C. Park, T.B. Eom, and M.S. Chung. Polarization properties of cube-corner retroreflectors and their effects on signal strength and nonlinearity in heterodyne interferometers. *Appl. Opt.*, 35(22):4372–4380, 1996.
- [71] C.M. Wu and C.S. Su. Nonlinearity in measurements of length by optical interferometry. *Meas. Sci. Technol.*, 7(1):62–68, 1996.

- [72] J.M. De Freitas. Analysis of laser source birefringence and dichroism on nonlinearity in heterodyne interferometry. *Meas. Sci. Technol.*, 8(11):1356–1359, 1997.
- [73] C.M. Wu and R.D. Deslattes. Analytical modeling of the periodic nonlinearity in heterodyne interferometry. *Appl. Opt.*, 37(28):6696–6700, 1998.
- [74] F. Petru and O. Cip. Problems regarding linearity of data of a laser interferometer with a single-frequency laser. *Precision Eng.*, 23(1):39–50, 1999.
- [75] S.J.A.G. Cosijns, H. Haitjema, and P.H.J. Schellekens. Modeling and verifying non-linearities in heterodyne displacement interferometry. *Precision Eng.*, 26(4):448–455, 2002.
- [76] H. Zhao and G. Zhang. Nonlinear error by orientation and elliptic polarization in a two-beam interferometer. *Opt. Eng.*, 41(12):3204–3208, 2002.
- [77] P. L. M. Heydemann. Determination and correction of quadrature fringe measurement errors in interferometers. *Appl. Opt.*, 20(19):3382–3384, 1981.
- [78] W. Hou and X. Zhao. Drift of nonlinearity in the heterodyne interferometer. *Precision Eng.*, 16(1):25–35, 1994.
- [79] J.A. Stone and L.P. Howard. A simple technique for observing periodic nonlinearities in Michelson interferometers. *Precision Eng.*, 22(4):220–232, 1998.
- [80] C. Yin, G. Dai, Z. Chao, Y. Xu, and J. Xu. Determining the residual nonlinearity of a high-precision heterodyne interferometer. *Opt. Eng.*, 38(8):1361–1365, 1999.
- [81] V.G. Badami and S.R. Patterson. A frequency domain method for the measurement of nonlinearity in heterodyne interferometry. *Precision Eng.*, 24(1):41–49, 2000.
- [82] T.L. Schmitz and J.F. Beckwith. An investigation of two unexplored periodic error sources in differential-path interferometry. *Precision Eng.*, 27(3):311–322, 2003.
- [83] S. Cosijns. *Displacement laser interferometry with sub-nanometer uncertainty*. PhD thesis, Technische Universiteit Eindhoven, 2004.
- [84] W. Hou and G. Wilkening. Investigation and compensation of the nonlinearity of heterodyne interferometers. *Precision Eng.*, 14(2):91–98, 1992.

- [85] J.H. Guo, Y. Zhang, and S. Shen. Compensation of nonlinearity in a new optical heterodyne interferometer with doubled measurement resolution. *Opt. Commun.*, 184(14):49–55, 2000.
- [86] O. P. Lay and S. Dubovitsky. Polarization compensation: a passive approach to a reducing heterodyne interferometer nonlinearity. *Opt. Lett.*, 27(10):797–799, 2002.
- [87] S. Dubovitsky. Heterodyne interferometer with phase-modulated carrier. *NASA Tech. Briefs*, 25(2), 2001.
- [88] S. Dubovitsky, O.P. Lay, and D.J. Seidel. Elimination of heterodyne interferometer nonlinearity by carrier phase modulation. *Opt. Lett.*, 27(8):619–621, 2002.
- [89] C.M. Wu, C.S. Su, and G.S. Peng. Correction of nonlinearity in one-frequency optical interferometry. *Meas. Sci. Technol.*, 7(4):520–524, 1996.
- [90] T. Eom, J. Y. Kim, and K. Jeong. The dynamic compensation of nonlinearity in a homodyne laser interferometer. *Meas. Sci. Technol.*, 12(10):1734–1738, 2001.
- [91] T. Eom, T. Choi, K. Lee, H. Choi, and S. Lee. A simple method for the compensation of the nonlinearity in the heterodyne interferometer. *Meas. Sci. Technol.*, 13(2):222–225, 2002.
- [92] T. Eom, J. Kim, C.-S. Kang, B. Park, and J. Kim. A simple phase-encoding electronics for reducing the nonlinearity error of a heterodyne interferometer. *Meas. Sci. Technol.*, 19:075302, 2008.
- [93] C.M. Wu, J. Lawall, and R.D. Deslattes. Heterodyne interferometer with subatomic periodic nonlinearity. *Appl. Opt.*, 38(19):4089–4094, 1999.
- [94] H. Takasaki, N. Umeda, and M. Tsukiji. Stabilized transverse zeeman laser as a new light source for optical measurement. *Appl. Opt.*, 19:435–441, 1980.
- [95] M. Tanaka and K. Nakayama. A new optical interferometer for absolute measurement of linear displacement in the subnanometer range. *Jpn. J. Appl. Phys.*, 22(4):L233–L235, 1983.
- [96] M.-S. Kim and S.-W. Kim. Two-longitudinal-mode He-Ne laser for heterodyne interferometers to measure displacements. *Appl. Opt.*, 41(28):5938–5942, 2002.

- [97] D.C. Su, M.H. Chiu, and C.D. Chen. A heterodyne interferometer using an electro-optic modulator for measuring small displacements. *J. Opt.*, 27(1): 19–23, 1996.
- [98] M. Tanaka, T. Yamagami, and K. Nakayama. Linear interpolation of periodic error in a heterodyne laser interferometer at subnanometer levels. *IEEE Trans. Instrum. Meas.*, 38(2):552–554, 1989.
- [99] C.M. Wu, S.T. Lin, and J. Fu. Heterodyne interferometer with two spatial-separated polarization beams for nanometrology. *Opt. Quantum Electron.*, 34(12):1267–1276, 2002.
- [100] C.M. Wu. Periodic nonlinearity resulting from ghost reflections in heterodyne interferometry. *Opt. Commun.*, 215(13):17–23, 2003.
- [101] H. Müller, S.-W. Chiow, Q. Long, C. Vo, and S. Chu. Active sub-Rayleigh alignment of parallel or antiparallel laser beams. *Opt. Lett.*, 30:3323–3325, 2005.
- [102] H. J. Kraus. Kompaktaufbau eines Interferometers als Demonstrator für einen optisch ausgelesenen Inertialsensor für LISA. Diplomarbeit, Fachhochschule NTA Isny, 2005.
- [103] G. Heinzel, V. Wand, A. Garcia, F. Guzman, F. Steier, C. Killow, D. Robertson, H. Ward, and C. Braxmaier. Investigation of noise sources in the LTP interferometer. Technical Note S2-AEI-TN-3028, Albert-Einstein Institute, Hannover, 2005.
- [104] G. Heinzel, J. Bogenstahl, C. Braxmaier, K. Danzmann, A. Garcia, F. Guzman, J. Hough, D. Hoyland, O. Jennrich, C. Killow, D. Robertson, Z. Sodnik, F. Steier, H. Ward, and V. Wand. Interferometry for the LISA technology package LTP: an update. *Class. Quantum Grav.*, 32:132–136, 2006.
- [105] M. Gohlke. Ein hochsymmetrisches Heterodyninterferometer zur Demonstration einer optischen Auslesung der Inertialsensoren des weltraumbasierten Gravitationswellendetektors LISA. Diplomarbeit, Humboldt-Universität zu Berlin, 2007.
- [106] T. Schuldt, M. Gohlke, D. Weise, U. Johann, A. Peters, and C. Braxmaier. Picometer and nanoradian optical heterodyne interferometry for translation and tilt metrology of the LISA gravitational reference sensor. *Class. Quantum Grav.*, 26:085008, 2009.
- [107] T. Schuldt. Frequenzstabilisierter Nd:YAG-Laser für Weltraumanwendungen. Diplomarbeit, Universität Hamburg, 2003.

- [108] T. Schuldt, C. Braxmaier, H. Müller, G. Huber, A. Peters, and U. Johann. Frequency stabilized Nd:YAG laser for space applications. In *Proceedings of the 5th International Conference on Space Optics (ICSO 2004)*, pages 611–617, ESA Publications, 2004.
- [109] K.P. Birch and M.J. Downs. An updated Edlen equation for the refractive index of air. *Metrologia*, 30(3):155–162, 1993.
- [110] K.P. Birch and M.J. Downs. Correction to the updated Edlen equation for the refractive index of air. *Metrologia*, 31(4):315–316, 1994.
- [111] F. Acernese. *An interferometric seismic sensor: theoretical model and experimental performances*. PhD thesis, Università di Napoli, 2005.
- [112] F. Acernese, R. De Rosa, F. Garufi, R. Romano, and F. Barone. A Michelson interferometer for seismic wave measurement: theoretical analysis and system performances. In *Proceedings of SPIE, Vol 6366, Remote Sensing for Environmental Monitoring, GIS Applications, and Geology VI*, page 63660I, 2006.
- [113] T. Heinrich. Interferometrische Messung des Thermischen Ausdehnungskoeffizienten von Kohlenstoff-Verbundwerkstoff für Weltraum-Anwendungen mit Pikometer-Stabilität. Masterarbeit, Hochschule Konstanz, 2007.
- [114] J. Cordero Machado, T. Heinrich, T. Schuldt, M. Gohlke, S. Lucarelli, D. Weise, U. Johann, A. Peters, and C. Braxmaier. Picometer resolution interferometric characterization of the dimensional stability of zero CTE CFRP. In *Proceedings of SPIE, Vol 7018, Advanced Optical and Mechanical Technologies in Telescopes and Instrumentation*, page 70183D, 2008.
- [115] J. Cordero Machado. Measurements of the linear coefficient of thermal expansion (CTE) of a theoretical zero CTE carbon-fiber reinforced plastic (CFRP) tube by means of a nanometer resolution optical dilatometer prototype. Diploma thesis, Escuela Superior de Ingenieros, Universidad de Sevilla, 2008.
- [116] J. Cordero Machado, T. Heinrich, T. Schuldt, M. Gohlke, S. Lucarelli, D. Weise, U. Johann, and C. Braxmaier. Interferometry based high-precision dilatometry for dimensional characterization of highly stable materials. *Meas. Sci. Technol.*, 20:095301, 2009.
- [117] T. Schuldt, M. Gohlke, D. Weise, U. Johann, and C. Braxmaier. A high-precision dilatometer based on sub-nm heterodyne interferometry. In *IEEE Conference Proceedings of ISOT*, 2009.

- [118] S. Gauss. Phasenauslesung und Signalverarbeitung eines Laser-Interferometers für die hochauflösende nicht-taktile Profilometrie. Bachelorarbeit, Hochschule Konstanz, 2009.
- [119] M. Schwierz. Modularer Aufbau und Charakterisierung des hochauflösenden und optischen, Sub-Nanometer-Profilometer genannten, Messsystems mit linearer Aktorik. Diplomarbeit, Hochschule Konstanz, 2009.
- [120] R. Spannagel. Integration und Test der Aktorik für ein Laserinterferometer zur hochauflösenden optischen Profilometrie. Bachelorarbeit, Hochschule Konstanz, 2009.
- [121] A. Vogel, M. Schmidt, K. Sengstock, K. Bongs, W. Lewoczko, T. Schuldt, A. Peters, T. Van Zoest, W. Ertmer, E. Rasel, T. Steinmetz, J. Reichel, T. Konemann, W. Brinkmann, E. Goklu, C. Lammerzähl, H.J. Dittus, G. Nandi, W.P. Schleich, and R. Walser. Bose-Einstein condensates in microgravity. *Applied Physics B*, 84:663–671(9), 2006.
- [122] S. Vitale, G. Heinzel, K. Danzmann, W. Weber, M. Hueller, and M. Hewitson. Recommendation for an algorithm for Power Spectral Density estimation for LISA Pathfinder. Technical Note S2-UTN-TN-3040, University degli studi di Trento, 2006.
- [123] N. Brandt and P. Gath. PlotPSD.m – a Matlab m-file for calculating the power spectral density. Technical report, Astrium GmbH, 2006.
- [124] H. Müller, S. Herrmann, M. Scholz, T. Schuldt, E. Kovalchuk, and A. Peters. Offset compensation by use of amplitude-modulated sidebands in optical frequency standards. *Opt. Lett.*, 28:2186–2188, 2003.
- [125] E. Kovalchuk, T. Schuldt, and A. Peters. A combination of cw-OPO and femtosecond frequency comb for optical frequency metrology. *Opt. Lett.*, 30:3141–3143, 2005.
- [126] C. Braxmaier. Frequenzstabilisierung eines Nd:YAG Lasers auf Hyperfeinübergänge von molekularem Jod. Diplomarbeit, Universität Konstanz, 1997.
- [127] T. Müller. Modellierung und Untersuchung der Frequenzdurchstimmung von DBR-Laserdioden. Diplomarbeit, Ernst-Moritz-Arndt-Universität Greifswald, 2002.
- [128] K.-D. Salewski, T. Kinder, and T. Müller. Lineare Frequenzdurchstimmung von DBR-Laserdioden. *Photonik*, 2:62–65, 2004.

- [129] K. G. Libbrecht and J. L. Hall. A low-noise high-speed diode laser current controller. *Rev. Sci. Instrum.*, 64(8):2133–2135, 1993.

Acknowledgments

It is a pleasure to thank all those people who supported me during my work over the last years. Without their help and contributions – and also friendship – this project would not have been possible.

First of all I would like to thank Prof. Dr. Claus Braxmaier and Prof. Achim Peters, PhD. They gave me the opportunity to work on a highly motivating subject related to the exciting LISA space mission. Claus always lives and shares his fascination about physics. His many ideas were invaluable for my work and they most probably will be the basis for a multitude of future student projects. Achim supported the project from the very beginning. With his ideas and his substantial knowledge of physics he made crucial contributions to this work. His knowledge of physics (including all technical details) still keeps fascinating me.

I am grateful to thank Dr. Ulrich Johann from Astrium GmbH, Friedrichshafen, who supported the ORO-project from the very beginning. I thank Dr. Dennis Weise who supported the establishment of the ‘laboratory for enabling technologies’ with firm conviction. He gave a multitude of wise advices which helped us to succeed with our experiment.

Two diploma theses were carried out as part of the ORO-activities. Hans-Jürgen Kraus from the University of Applied Sciences Isny helped building up and characterizing the first experimental setup which still exists. His initial fear as an engineer not to survive in a group of physicists fortunately did not come true. Martin Gohlke joined our ORO-group as a diploma student from the HU Berlin, moved to the lake of Constance and now continues his work on the ORO. He was involved in the second setup, his work and patience were invaluable. Thanks a lot!

When working at the Humboldt-University, many colleagues contributed to my work. Many thanks to Sven Herrmann whose modesty and physics knowledge already impressed me during my diploma thesis. I am indebted to Evgeny Kovalchuk, Holger Müller, Wojtek Lewoczko-Adamczyk and Katharina Möhle. They took part in many discussions and gave lots of useful inputs and suggestions. Together, they all created an inspiring atmosphere in our Berlin group. Without Sven, Evgeny and Holger, the project would have a much lower technical realization. Evgeny, thank you for sharing the office – and your physics knowledge and Ukrainian life – with me. Thanks to Holger, the integral for the arctan-calculation could be solved. Many thanks to all other members of the QOM, NANO and AMO groups.

Special thanks to Dipl.-Ing. Klaus Palis whose expertise in electronic and me-

chanical design was of great value for my work. I also thank him for his friendship and the way he was creating a highly motivating and friendly atmosphere on our physics floor. Many thanks to Mr. Rausche and his team at the HU mechanics shop. Their effort is highly appreciated.

The DBR laser diodes were provided by the Ferdinand Braun Institut für Höchstfrequenztechnik, Berlin. Special thanks to Dr. Andreas Klehr for his support.

Many thanks to my colleagues at Astrium in Friedrichshafen: Peter Gath, Hans-Reiner Schulte, Andreas Keller, Francesca Cirillo and all the others involved in LISA, LISA pathfinder and our laboratory for enabling technologies. Many thanks to Thomas Heinrich and Jorge Cordero who performed their graduation works in the dilatometer project. Their efforts and endurance were the basis for its success. Martin Maurer was involved in the DBR laser module setup and crucially contributed to its progress. Many thanks to all other students in the LET.

At HTWG, I would like to thank Hermann Richter who was the technician most involved in our optics lab and Jürgen Romer, Wendelin Biller and their colleagues from the mechanical shop. I would like to thank all members of the Institute of Optical Systems (IOS) which was founded in 2008 at HTWG. A special thanks to Ruven Spannagel who put lots of time in setting the profilometer setup into operation and is still involved in it.

I am indebted to the LISA group at the Albert-Einstein Institute, Hannover, especially to Prof. Dr. Karsten Danzmann and Dr. Gerhard Heinzel. My work was always coordinated with their activities and they supported it at any time. Also appreciated are the discussions with Felipe Guzman Cervantes, Frank Steier, Sascha Skorupka, Antonio Garcia Marin, and Michael Tröbs. Thanks to Johanna Bogenstahl who shared her experience in hydroxide-catalysis bonding with us.

Half a year I was working on the drop-BEC project. Many thanks to all the collaboration members, it was a great time – resulting in the first BEC under microgravity. For the laser system, coordinating the project with Anika Vogel from the Hamburg university was always a pleasure.

A special thanks to Martin Gohlke, Sven Herrmann and Evgeny Kovalchuk for proof-reading of my thesis.

I am very much indebted to my parents. Without their permanent support, my academic studies and the work on this thesis would not have been possible. Thank you so much! Last but not least, I thank Maren, who enriched my life for the last year. Now, we can plan our future together :-)

List of Publications

Journals

1. *Bose-Einstein Condensation in Microgravity*
T. van Zoest, N. Gaaloul, Y. Singh, H. Ahlers, W. Herr, S. T. Seidel, W. Ertmer, E. Rasel, M. Eckart, E. Kajari, S. Arnold, G. Nandi, W. P. Schleich, R. Walser, A. Vogel, K. Sengstock, K. Bongs, W. Lewoczko-Adamczyk, M. Schiemangk, T. Schuldt, A. Peters, T. Könemann, H. Müntinga, C. Lämmerzahl, H. Dittus, T. Steinmetz, T. W. Hänsch, J. Reichel
Science 328, no. 5985 (2010) 1540-543
2. *Ultra-stable assembly and integration technology for ground- and space-based optical systems*
S. Ressel, M. Gohlke, D. Rauen, T. Schuldt, W. Kronast, U. Mescheder, U. Johann, D. Weise, and C. Braxmaier
Appl. Opt. 49 (2010) 4296-4303
3. *Sub-nanometer heterodyne interferometry and its application in dilatometry and industrial metrology*
T. Schuldt, M. Gohlke, R. Spannagel, S. Ressel, D. Weise, U. Johann, and C. Braxmaier
Int. J. Optomechatronics 3 (2009) 187-200
4. *Interferometry based high-precision dilatometry for dimensional characterization of highly-stable materials*
J. Cordero, T. Heinrich, T. Schuldt, M. Gohlke, S. Lucarelli, D. Weise, U. Johann, and C. Braxmaier
Meas. Sci. and Technol. 20 (2009) 095301
5. *Picometer and nanoradian optical heterodyne interferometry for translation and tilt metrology of the LISA gravitational reference sensor*
T. Schuldt, M. Gohlke, D. Weise, U. Johann, A. Peters, and C. Braxmaier
Class. Quantum Grav. 26 (2009) 085008
6. *Compact Laser Interferometer for Translation and Tilt Metrology*
T. Schuldt, M. Gohlke, D. Weise, U. Johann, A. Peters, and C. Braxmaier
Int. J. Optomechatronics 1 (2007) 168-179

7. *Bose-Einstein condensates in microgravity*
A. Vogel, M. Schmidt, K. Sengstock, K. Bongs, W. Lewoczko, T. Schuldt, A. Peters, T. v. Zoest, W. Ertmer, E. Rasel, T. Steinmetz, J. Reichel, T. Köne-
mann, W. Brinkmann, E. Göklü, C. Lämmerzahl, H. J. Dittus, G. Nandi, W.
P. Schleichner, and R. Walser
Appl. Phys. B: Lasers and optics, Vol. 84, 663-671 (2006)
8. *A combination of cw-OPO and femtosecond frequency comb for optical fre-
quency metrology*
E. Kovalchuk, T. Schuldt, and A. Peters
Optics Letters, Vol 30, Issue 23, 3141-3143 (2005)
9. *Offset compensation by use of amplitude-modulated sidebands in optical fre-
quency standards*
H. Müller, S. Herrmann, T. Schuldt, M. Scholz, E. Kovalchuk, and A. Peters
Optics Letters, Vol 28, Issue 22, 2186-2188 (2003)
10. *Hochstabile Nd:YAG-Miniatur-Ringlaser im sichtbaren Spektralbereich mit
aktiver Frequenzstabilisierung auf molekulares Jod*
M. Bode, J. Meyer, M. Tröbs, T. Schuldt, A. Peters, and C. Braxmaier
Photonik, 2-4 (January 2003)

Conference proceedings

1. *The Space-Time Asymmetry Research (STAR) Program*
C. Braxmaier, T. Schuldt, M. Allab, T. van Zoest, S. Theil, I. Pelivan, S.
Herrmann, C. Lämmerzahl, A. Peters, K. Möhle, A. Wicht, M. Nagel, E.
Kovalchuk, K. Döringshoff, and H. Dittus
ESA Proceedings of the 24th European Time and Frequency Forum 2010,
Noordwijk (The Netherlands)
2. *Dual absolute and relative high precision laser metrology*
K. Ergenzinger, T. Schuldt, P. Berlioz, C. Braxmaier, and U. Johann
Proc. of the 8th International Conference on Space Optics (ICSO 2010)
3. *Development of a tilt actuated micromirror for applications in laser interfer-
ometry*
W. Kronast, U. Mescheder, B. Müller, A. Nimo, C. Braxmaier, and T. Schuldt
Proc. of SPIE, Vol 7594, MOEMS and Miniaturized Systems IX (2010)

4. *High-resolution dimensional metrology for industrial applications*
T. Schuldt, M. Gohlke, D. Weise, A. Peters, U. Johann, and C. Braxmaier
Key Engineering Materials, Vol. 437 (2010); Conference Proceedings of the 9th International Symposium on Measurement Technology and Intelligent Instruments (ISMTEI 2009)
5. *A high-precision dilatometer based on sub-nm heterodyne interferometry*
T. Schuldt, M. Gohlke, D. Weise, U. Johann, and C. Braxmaier
IEEE Conference Proc.: International Symposium on Optomechatronic Technologies (2009), 146-151
6. *A high precision heterodyne interferometer for relative and absolute displacement measurement*
M. Gohlke, T. Schuldt, D. Weise, A. Peters, U. Johann, and C. Braxmaier
IEEE Conference Proc.: International Symposium on Optomechatronic Technologies (2009), 289-293
7. *Development of an ultrasensitive interferometry system as a key to precision metrology applications*
M. Gohlke, T. Schuldt, D. Weise, U. Johann, A. Peters, and C. Braxmaier
Proc. of SPIE, Vol 7389, 3D interferometry, 73890V (2009)
8. *A high-sensitivity heterodyne interferometer as a possible optical readout for the LISA gravitational reference sensor and its application to technology verification*
M. Gohlke, T. Schuldt, D. Weise, U. Johann, A. Peters, and C. Braxmaier
Journal of Physics: Conference Series 154 – Proceedings of the 7th International LISA Symposium, 012030 (2009)
9. *A heterodyne interferometer for high-performance industrial metrology*
T. Schuldt, M. Gohlke, D. Weise, U. Johann, A. Peters, and C. Braxmaier
Proc. of SPIE, Vol 7266, Optomechatronic sensor design, 72660M (2008)
10. *A high sensitivity heterodyne interferometer as a possible optical readout for the LISA gravitational reference sensor and its application to technology verification*
M. Gohlke, T. Schuldt, D. Weise, J. Cordero, A. Peters, U. Johann, and C. Braxmaier
Proc. of the 7th International Conference on Space Optics (ICSO 2008)
11. *A high-sensitivity heterodyne interferometer for industrial metrology*
T. Schuldt, M. Gohlke, D. Weise, A. Peters, U. Johann, and C. Braxmaier
Proc. of the IMEKO TC 2 Symposium on Photonics in Measurements (2008)

12. *Picometer resolution interferometric characterization of the dimensional stability of zero CTE CFRP*
J. Cordero Machado, T. Heinrich, T. Schuldt, M. Gohlke, S. Lucarelli, D. Weise, U. Johann, A. Peters, and C. Braxmaier
Proc. of SPIE, Vol 7018, Advanced optical and mechanical technologies in telescopes and instrumentation, 70183D (2008)
13. *A compact high-sensitivity heterodyne interferometer for industrial metrology*
T. Schuldt, M. Gohlke, D. Weise, A. Peters, U. Johann, and C. Braxmaier
Proc. of SPIE, Vol 7003, Optical Sensors, 70030Y (2008)
14. *Compact laser interferometer for translation and tilt measurement as optical readout for the LISA inertial sensor*
T. Schuldt, M. Gohlke, D. Weise, U. Johann, A. Peters, and C. Braxmaier
Proc. of SPIE, Vol 6716, Optomechatronic Sensors and Instrumentation III, 67160F (2007)
15. *Adopting our heterodyne interferometer with sub-nm sensitivity for industrial position metrology*
T. Schuldt, M. Gohlke, D. Weise, A. Peters, U. Johann, and C. Braxmaier
Proc. of SPIE, Vol 6616, Optical Measurement Systems for Industrial Inspection V, 661649 (2007)
16. *A high sensitivity heterodyne interferometer as optical readout for the LISA inertial sensor*
T. Schuldt, H.-J. Kraus, D. Weise, C. Braxmaier, A. Peters, and U. Johann
Proc. of SPIE, Vol 6293, Interferometry XIII, 62930Z (2006)
17. *A heterodyne interferometer for high resolution translation and tilt measurement as optical readout for the LISA inertial sensor*
T. Schuldt, H.-J. Kraus, D. Weise, C. Braxmaier, A. Peters, and U. Johann
Proc. of the 6th International Conference on Space Optics (ICSO 2006), ESA SP-621 June 2006
18. *A high sensitivity heterodyne interferometer as optical readout for the LISA inertial sensor*
T. Schuldt, H.-J. Kraus, D. Weise, A. Peters, U. Johann, and C. Braxmaier
AIP Conference Proceedings, Vol. 873, 374-378 (6th Int. LISA Symposium, 2006)

-
19. *TNO TPD contributions to high-precision optical metrology: a Darwin metrology breadboard for ESA*
A. L. Verlaan, T. C. van den Dool, B. C. Braam, B. Calvel, R. Sesselmann, W. Poeschel, D. Dontsov, I. Cabeza Vega, E. Manske, T. Schuldt, and Z. Sodnik
Proc. of SPIE, Vol. 5528, Space Systems Optomechanics and Dynamics, 32-43 (2004)
 20. *Frequency stabilized Nd:YAG laser for space applications*
T. Schuldt, C. Braxmaier, H. Müller, G. Huber, A. Peters, and U. Johann
Proc. of the 5th International Conference on Space Optics (ICSO 2004), pp. 611-617, ESA SP-554 June 2004

List of Figures

1.	Artist's view of the LISA space mission	3
2.	Comparison of different ORO sensitivities	4
1.1.	Polarizations of gravitational waves	7
1.2.	Spectrum of gravitational waves	8
1.3.	Indirect proof of gravitational waves	10
1.4.	Gravitational waves acting on a ring of free masses	11
2.1.	LISA sensitivity curve	14
2.2.	LISA orbit	15
2.3.	Schematic of the LISA spacecraft	16
2.4.	Schematic of the strap-down architecture	17
2.5.	Schematic of the LISA payload module	19
2.6.	Schematic of the LISA Optical Bench	20
2.7.	Photograph of the LTP GRS prototype	21
3.1.	Schematic of a capacitive PM position readout	24
3.2.	Schematic of a SQUID based accelerometer	25
3.3.	Possible optical readout methods	27
3.4.	Multiple-path interferometry	28
3.5.	Optical readout developed at the University of Napoli	30
3.6.	Optical readout at the University of Birmingham	31
3.7.	Optical readout at Stanford University	32
3.8.	LTP optical readout aboard LISA pathfinder	33
4.1.	Schematic of a Michelson interferometer	36
4.2.	Homodyne Michelson interferometer	39
4.3.	Homodyne Michelson interferometer with IQ readout	40
4.4.	Schematic of a heterodyne interferometer	41
4.5.	Generation of the heterodyne frequencies by use of 2 AOMs	45
4.6.	Schematic of a Mach-Zehnder interferometer	46
4.7.	Heterodyne interferometer with spatially separated frequencies	47
4.8.	Heterodyne interferometer design as basis for our optical readout	49
4.9.	Implementation of a symmetric beamsplitter	50
4.10.	Schematic of Differential Wavefront Sensing	51

4.11. Quadrant photodiode used for DWS	52
5.1. Generation of the heterodyne frequencies	54
5.2. Schematics of the AOM driving electronics	55
5.3. Schematic of the first interferometer setup	56
5.4. Photograph of the first setup.	56
5.5. Schematic of the analog IQ phase measurement	57
5.6. First check of the interferometer	58
5.7. Time series and PSD with PZT in the measurement arm	60
5.8. Measured translation and corresponding temperature	61
5.9. Individual interferometer signals	61
5.10. Translation time series	62
5.11. Time series and PSD with beams reflected by the PZT	63
5.12. Influence of intensity variations (AOM1)	64
5.13. Influence of intensity variations (AOM2)	64
5.14. PSD under vacuum condition	65
5.15. Time series and PSD with one fixed mirror	67
5.16. PSD of the tilt measurement	68
6.1. Schematic of the heterodyne frequency generation	72
6.2. Photograph of the frequency generation setup	73
6.3. Schematic of the electronics for heterodyne frequency generation	73
6.4. Schematic of the second interferometer setup	74
6.5. Photograph of the second interferometer setup	74
6.6. Photograph detail of the interferometer	75
6.7. AOM sidebands near 80 MHz	77
6.8. AOM sidebands near 77 MHz	77
6.9. Schematic of the digital phase measurement	78
6.10. Translation signal while tilting a glass plate	80
6.11. Time series and PSD of a 60 h measurement	81
6.12. PSD of the translation measurement	82
6.13. Time series with and without phaselock	83
6.14. PSD with and without frequency stabilization	83
6.15. PSD with analog and digital phase measurement	84
6.16. Time series and PSD of the tilt measurement	85
6.17. Schematic of the gas-cell	86
6.18. Photograph of the gas-cell	86
6.19. Translation during flooding the gas cell	87
6.20. Nonlinearities of the interferometer	88
6.21. Nonlinearities of the interferometer (electronic stimuli)	89
6.22. PSD of the nonlinearity measurements	89
6.23. Translation noise comparison	91

6.24. Tilt noise comparison	91
6.25. Time series and PSD for noise analysis	93
6.26. PSD of the translation measurement for different phase shifts	94
7.1. Measurement concept of the dilatometer	96
7.2. CAD drawing of the CTE test facility	97
7.3. Photograph of the CTE test facility	98
7.4. Mirror mounts	98
7.5. CTE measurement	100
7.6. Schematic of an optical profiler	101
7.7. Photograph of the interferometer adapted for optical profilometry	103
7.8. Photograph of the interferometer board	103
7.9. PSD of the translation measurement (profilometer setup)	104
7.10. Profilometer measurement	104
8.1. Sketch of a miniaturized interferometer	111
8.2. CAD drawing of the miniaturized interferometer	111
A.1. Photograph of the DBR laser module	114
B.1. Labeling of the individual quadrants	115
B.2. Schematic of the quadrant diode preamplifier	116
B.3. Schematic of the quadrant diode summing board	117
B.4. Photograph of the integrated quadrant photodiode electronics	118
B.5. Schematic of the 2 Hz anti-aliasing filter	118
B.6. Schematic of the PID servo loop	119
B.7. Schematic of the anti-aliasing filter	120
C.1. LabView program for calculating the translation (1)	123
C.2. LabView program for calculating the translation (2)	124
C.3. FPGA LabView Program	125
C.4. Host LabView program	126
E.1. Photograph of the Iodine stabilized Nd:YAG laser	130
F.1. Three section DBR laser diode	132
F.2. DBR laser module	134
F.3. Schematic of the beat measurement	134

List of Tables

1.1. Currently operating resonant bar detectors	11
1.2. Currently operating interferometric GW detectors	12
2.1. LISA requirements (interferometric measurement)	18
2.2. DFACS requirements for LISA	22
3.1. Requirements for the LISA inertial sensor readout	24
8.1. Comparison of different LISA optical readout implementations . . .	108
C.1. Specifications of the DAQ computer boards	121

Selbständigkeitserklärung

Hiermit erkläre ich, die vorliegende Arbeit selbständig ohne fremde Hilfe verfasst und nur die angegebene Literatur und Hilfsmittel verwendet zu haben.

Ich habe mich anderwärts nicht um einen Doktorgrad beworben und besitze einen entsprechenden Doktorgrad nicht.

Ich erkläre die Kenntnisnahme der dem Verfahren zugrunde liegenden Promotionsordnung der Mathematisch-Naturwissenschaftlichen Fakultät I der Humboldt-Universität zu Berlin.

Berlin, den 12. Oktober 2009

Thilo Schuldt